

Microscopy and digital light shaping through optical fibers

THÈSE N° 7799 (2017)

PRÉSENTÉE LE 23 JUIN 2017

À LA FACULTÉ DES SCIENCES ET TECHNIQUES DE L'INGÉNIEUR
LABORATOIRE DE DISPOSITIFS PHOTONIQUES APPLIQUÉS
PROGRAMME DOCTORAL EN PHOTONIQUE

ÉCOLE POLYTECHNIQUE FÉDÉRALE DE LAUSANNE

POUR L'OBTENTION DU GRADE DE DOCTEUR ÈS SCIENCES

PAR

Damien Claude-Marie LOTERIE

acceptée sur proposition du jury:

Prof. H. Altug, présidente du jury
Prof. C. Moser, directeur de thèse
Prof. S. Gigan, rapporteur
Dr T. Cizmar, rapporteur
Prof. D. Psaltis, rapporteur



ÉCOLE POLYTECHNIQUE
FÉDÉRALE DE LAUSANNE

Suisse
2017

Acknowledgements

After completing this thesis, I'm glad to have the opportunity to thank all the colleagues, friends and family who contributed in one way or another to the realization of my research project at the Laboratory of Applied Photonics Devices in École polytechnique fédérale de Lausanne.

First, thanks to Professor Christophe Moser, my thesis director. I am very grateful for having had the opportunity to do this PhD and I had an amazing time in his lab. I really appreciated all his encouragements and his advice. Thanks also to Dr. Salma Farahi, for helping me get started in this project and for her contributions during the writing of my first multimode fiber imaging paper.

I want to thank my office mates, Dino, Manon, Paul, Salma and Claudia, for having been such a great company, and for all the interesting and funny discussions we've had over the years. Thanks as well to all the other colleagues in the lab, for the help they gave me, for their friendship, and for their enthusiasm: Emilio, Sébastien, Volker, Zahra, Miguel, Enrico, Gaël, Timothé, Frédéric, Laurent, Mathieu, Andreas, David, Eric, Mickaël, Philippe, Ronald, Arnaud, Jan, Maya and Sunan. And special thanks to Sabrina for all the administrative support and for being a great organizer. I'm grateful to all of the members of Professor Christophe Moser's lab, and I feel very fortunate to have been part of this group for these four years.

Thanks also to Prof. Psaltis for his helpful feedback, and to the members of the Laboratory of Optics, particularly those whom I collaborated with more closely during certain phases of the project: Yiannis, Nico, Donald, Grégoire, Carole, Jacob, Marilisa, Eirini, Thomas and Alexandre. It has always been a pleasure to interact with them, both during work and outside.

Many thanks to the members of my thesis committee, Prof. Altug, Prof. Psaltis, Prof. Gigan and Dr. Čižmár, for setting aside time to review my work. Thanks also to Chris, Paul, Claude and Sezin for their attention in proofreading the thesis text.

Finally, thanks to my parents for their continuous support, and to my dear wife for bringing so much happiness to my life.

Lausanne, 21st of April 2017

Damien

Résumé

La microscopie est un outil essentiel dans l'exercice de la médecine et la recherche biomédicale. Les microscopes traditionnels sont généralement dotés de composants optiques volumineux, ce qui complique leur usage lors de l'étude de tissus d'animaux vivants. De plus, à cause du phénomène de diffusion, la lumière ne peut pas s'infiltrer très profondément dans la plupart des tissus biologiques. Seuls les tissus superficiels sont donc accessibles de façon non-invasive à l'imagerie optique.

Dans cette thèse, l'imagerie microscopique a été réalisée à travers une simple fibre optique. Les fibres optiques sont extrêmement fines (moins de $300\ \mu\text{m}$) et guident la lumière efficacement. Leur emploi fournit donc une solution minimalement invasive permettant une observation microscopique à n'importe quelle profondeur dans des tissus.

Pour recueillir des images à travers une fibre optique, il faut compenser le brouillage modal, cet effet qui brouille les images lors de leur propagation à travers une fibre multimode. L'outil utilisé dans cette thèse pour contrôler la lumière et annuler le brouillage modal est la matrice de transmission. Cet outil permet de décrire précisément la relation entrée-sortie de n'importe quel système optique. Une procédure a été développée pour mesurer de grandes matrices de transmission avec exactitude, en utilisant l'holographie digitale et l'adaptation de front d'onde avec un modulateur spatial. Des images de haute résolution ont ainsi pu être transmises à travers des fibres dans diverses configurations. Sur base des résultats obtenus, la microscopie confocale a été implémentée pour augmenter le contraste. Pour finir, la résistance des fibres à la déformation a été étudiée, et une série de conditions ont été identifiées qui permettent de déformer une fibre sans perdre trop de qualité d'image.

L'imagerie à travers les fibres optiques est une solution prometteuse pour la microscopie endoscopique. En compensant le brouillage modal, il est possible de transformer une fibre optique en un microscope extrêmement fin avec une résolution à la limite de la diffraction. Cet outil pourrait être utilisé pour optimiser le résultat des biopsies ou dans d'autres applications requérant une imagerie minimalement invasive.

Mots clés : imagerie via des fibres optiques, microscopie, matrice de transmission, holographie digitale, adaptation de front d'onde, modulateur spatial de lumière.

Abstract

Microscopy is an essential tool in medicine and biomedical research. Traditional microscopes rely on bulky optics, complicating their usage when studying live animal tissues. In addition, light cannot penetrate very far in most biological tissues due to scattering, so typically only superficial tissues can be accessed non-invasively.

In this thesis, microscopic imaging was achieved through a single multimode optical fiber. Fibers are extremely thin (less than $300\mu\text{m}$) and guide light efficiently, so they provide a minimally invasive solution for microscopic imaging at any depth inside tissues.

Imaging via single fibers requires compensation of modal scrambling, an effect that distorts images in multimode fibers. The tool used in this thesis to control light and undo modal scrambling is the transmission matrix, a general framework that can describe the input-output relationship of any optical system very precisely. A procedure was developed to measure large transmission matrices accurately, based on digital holography and wavefront shaping with spatial light modulators. High-resolution image transmission through single fibers was subsequently demonstrated in a variety of configurations. Building on these results, confocal imaging was implemented in order to increase image contrast. Finally, the bending tolerance was investigated, and a set of conditions was identified under which fibers can be deformed without losing significant imaging performance.

Multimode fiber imaging is a promising solution for endoscopic microscopy. By compensating modal scrambling, it is possible to turn fibers into extremely thin microscopes with diffraction-limited resolution. This could be applied for example to assist in biopsies or for other minimally invasive imaging applications.

Keywords: fiber optics imaging, microscopy, transmission matrix, digital holography, wavefront shaping, spatial light modulators.

Contents

Acknowledgements	i
Résumé	iii
Abstract	v
Table of contents	vii
List of Figures	xi
1 Introduction	1
1.1 Basic concepts	1
1.1.1 Optical fibers	1
1.1.2 Modal scrambling	2
1.2 Motivation	3
1.2.1 Microscopy of deep tissues	3
1.2.2 Fiber bundles	4
1.2.3 Multimode fiber microscopy	5
1.3 Literature review	6
1.3.1 Scattering media	6
1.3.2 Multimode fiber imaging	7
2 Digital light control	11
2.1 Digital off-axis holography	11
2.1.1 Choice of the method	11
2.1.2 Theory	12
2.1.3 Reconstruction procedure	14
2.1.4 Practical aspects	14
2.2 Liquid crystal phase modulators	18
2.2.1 Choice of the modulator	18
2.2.2 Temporal response	19
2.2.3 Other non-idealities	21
2.2.4 Amplitude coding	23
2.3 Resolution	25
	vii

Contents

3	Transmission matrix	29
3.1	Theory	29
3.1.1	Introduction	29
3.1.2	General properties	31
3.2	Experimental aspects	33
3.2.1	Fourier basis	33
3.2.2	Phase drift tracking	35
3.2.3	Memory requirements	38
3.3	Measurement	40
3.4	Conclusion	42
4	Image transmission	45
4.1	Pattern projection	45
4.1.1	Inversion of the matrix	45
4.1.2	Results	46
4.2	Scanning microscopy	51
4.3	Reverse image transmission	53
4.3.1	Setup	53
4.3.2	Alignment of camera and SLM	54
4.3.3	Results	54
4.4	Conclusion	56
5	Digital confocal imaging	57
5.1	Introduction	57
5.1.1	Fiber-based confocal endoscopes	57
5.1.2	Multimode fiber confocal microscopy	58
5.2	Methods	59
5.2.1	Experimental setup	59
5.2.2	Digital processing algorithms	60
5.3	Results	61
5.4	Discussion	63
5.4.1	Contrast, sectioning and image quality	63
5.4.2	Speed	63
5.4.3	Digital pinhole versus correlation method	64
5.4.4	Bending and stability	65
5.5	Conclusion	65
6	Correlation-based confocal imaging	67
6.1	Introduction	67
6.2	Methods	68
6.2.1	Setup and fiber characterization	68
6.2.2	Optical correlation	69
6.2.3	Point spread function simulation	69

6.3	Results	70
6.4	Discussion	71
6.5	Considerations for fluorescence	71
6.5.1	Multispectral matrices	72
6.5.2	Bandwidth of step-index fibers	72
6.5.3	Simulation results	73
6.5.4	Discussion	74
6.6	Conclusion	74
7	Bend translation	75
7.1	Introduction	75
7.2	Methods	76
7.2.1	Overview	76
7.2.2	Experimental setup	76
7.2.3	Speckle patterns	77
7.2.4	Spot focusing	78
7.2.5	Simulations	79
7.3	Results	81
7.4	Discussion	82
7.5	Conclusion	85
8	Conclusion	87
8.1	Summary of the results	87
8.2	Future work	88
8.3	End word	88
A	Fiber modes	91
A.1	From Maxwell's equations to the wave equation	91
A.2	Wave equation in an optical fiber	92
A.3	Continuity conditions and characteristic equation	96
A.4	Finding the amplitude coefficients	99
A.5	Rewriting the field equations	100
A.6	Normalization	102
A.7	Numerical procedure	103
	Bibliography	107
	Curriculum Vitae	124

List of Figures

1.1	Total internal reflection at the core to cladding interface of a fiber	2
1.2	Difference in image transmission between lenses and fibers	2
1.3	Imaging via a fiber bundle	4
1.4	Schematic comparison of multimode fibers versus other modalities	5
1.5	Illustration of holographic spot projection	8
2.1	Geometry for digital off-axis holography.	13
2.2	Separation of the various terms in the Fourier transform of an off-axis hologram.	14
2.3	Reconstruction of a speckle pattern from its hologram at the output of a fiber.	15
2.4	Fourier-space derivation of the optimal angle for the reference beam.	16
2.5	Optimum off-axis reference angle	17
2.6	Aliasing in off-axis holograms	18
2.7	Temporal response of a spatial light modulator	20
2.8	Unwanted diffraction orders	23
2.9	The Gerchberg-Saxton algorithm to encode amplitude in phase-only images	24
2.10	Definitions for the derivation of the required number of pixels	25
3.1	The transmission matrix model for multimode fibers	30
3.2	Fourier basis for the measurement of the transmission matrix	35
3.3	Temporal stability of the reference phase	36
3.4	Timing diagram of the matrix measurement	38
3.5	Matrix size in memory	38
3.6	Experimental setup for the transmission matrix measurement	41
3.7	Measured transmission matrix	42
3.8	Unitarity of the transmission matrix	43
3.9	Transmission maps derived from the matrix	43
3.10	Singular value decomposition of the transmission matrix	44
4.1	Experimental results for pattern projection	48
4.2	Pattern projection in the far field	49
4.3	Focused spots created through a variety of fibers	50
4.4	Bottle and vortex beam created through a fiber	51
4.5	Two-photon fluorescence imaging setup	52
4.6	Two-photon fluorescence image of a mouse cochlea	53

List of Figures

4.7	Setup for reverse image transmission	54
4.8	Results for reverse image transmission	55
5.1	Digital confocal imaging setup	59
5.2	Illustration of the two digital processing methods for confocal microscopy . . .	60
5.3	Results for the digital confocal method	62
5.4	Transversal scans of a coverslip	62
6.1	Correlation-based confocal imaging setup	68
6.2	Simulated point spread function for a pinhole size	70
6.3	Experimental results for correlation confocal imaging	71
6.4	Spectral decorrelation bandwidth of a step-index fiber	73
7.1	Experimental setup for imaging during translation of a bend in the fiber	77
7.3	Autocorrelation of the output as the bend is translated	82
7.4	Change in intensity of a focused spot due to the translation of the bend	83
7.5	Patterns at the tip of a fiber before and after the bend is shifted	83
7.6	Simulation of a U-shaped bend	84
A.1	Geometry of an optical fiber	93
A.2	Solutions of the characteristic equation	98
A.3	Examples of fiber modes	104

1 Introduction

Optical fibers are well-known for their ubiquitous use in today's telecommunication systems. A lesser known fact is that before telecommunications, the first major commercial success of fibers has actually been in the field of medical endoscopy for the visual inspection of cavities inside the human body [1]. Many crucial developments occurred in this context, such as glass-clad fibers and reliable fiber drawing techniques. These efforts led to the creation of fiber bundles, which contain several thousands of individual optical fibers in a tightly packed array. Each of these fiber cores acts as a "pixel" that can observe one point of the image on the other end of the bundle.

Recent technological and scientific improvements have opened a new door for optical fiber imaging: the possibility to make images composed of many pixels using a single fiber, as opposed to a bundle of fibers. This greatly reduces the size of the probe necessary for a given resolution. In this thesis, a tool called the transmission matrix (chapter 3) is applied to realize imaging via a single multimode fiber (chapter 4). Based on this method, confocal imaging is implemented to improve imaging contrast (chapter 5 and chapter 6). Finally, the bending sensitivity of this system is studied in various fibers (chapter 7).

This introductory chapter reviews the basics of optical fibers, and situates the present work within the broader context of imaging in biological tissue. It also reviews the literature about wavefront shaping and fiber imaging.

1.1 Basic concepts

1.1.1 Optical fibers

Optical fibers guide light by a principle known as total internal reflection, as illustrated in Figure 1.1. Fibers are made from a core material (usually glass) surrounded by a cladding of lower refractive index ($n_{cladding} < n_{core}$). Light entering the core with an angle θ_{in} below the critical angle θ_c of the fiber is prevented from leaving the core due to total internal reflection

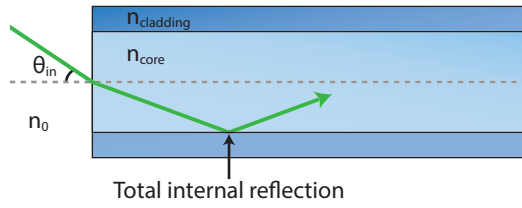


Figure 1.1: Total internal reflection at the core to cladding interface of a fiber.

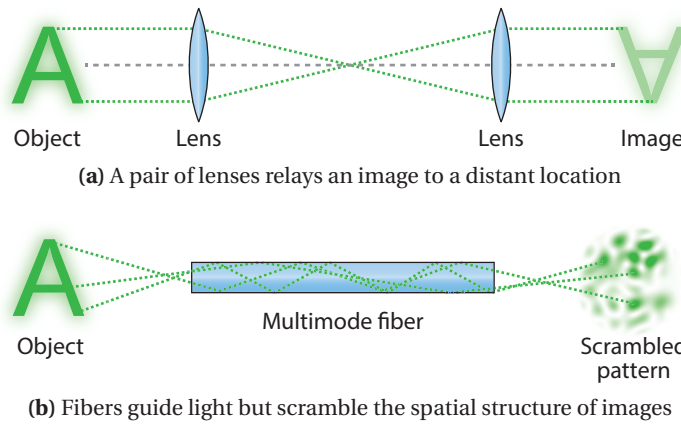


Figure 1.2: Difference in image transmission between (a) lenses and (b) fibers.

at the core-to-cladding interface. The critical angle defines the numerical aperture of the fiber, as expressed by Equation 1.1.

$$n_0 \sin \theta_c = \sqrt{n_{core}^2 - n_{cladding}^2} \triangleq NA \tag{1.1}$$

1.1.2 Modal scrambling

An optical fiber can transport light, but unlike a lens, a fiber does not by itself relay images. While lenses are able to refocus light rays from each point of an object onto an image plane, light rays follow seemingly random paths in an optical fiber and do not refocus at the output of the fiber as is necessary for imaging. This is illustrated in Figure 1.2. While the information about the image is not lost in this process, it becomes scrambled and the image is not recognizable at the output of the fiber.

In terms of electromagnetic theory, the randomization is due to the existence of modes that propagate with different phase velocities inside the fiber. A mode is a pattern of light which maintains a constant shape as it travels through the fiber. Each fiber can only guide a limited set of modes between its input and output. Single-mode fibers, as used for telecommunications, cannot be used on their own for imaging because they can guide only one specific

pattern of light (any other pattern is not transmitted)¹. Multimode fibers on the other hand are capable of guiding a variety of patterns, more so with increasing core diameter and numerical aperture. They are therefore able to transmit the spatial information contained in images.

When an image is sent through a multimode fiber, the light distributes itself into the available modes. Each of the modes has a different phase velocity, which quickly leads the various components of the image to lose their phase relationship with each other. This in turns leads to the apparent randomization of the image at the fiber's output. This effect is called modal scrambling. With sufficient knowledge about the propagation process inside the fiber, it is nonetheless possible to reconstruct the original image, as will be explained in chapter 4. A detailed mathematical derivation of modes and propagation constants can be found in Appendix A.

1.2 Motivation

This thesis describes a method to overcome modal scrambling and use multimode fibers as microscopic imaging devices. The present section explains the purpose of this work and how it relates to other methods with similar objectives.

1.2.1 Microscopy of deep tissues

Many diseases can be diagnosed based on the microscopic structure of affected tissues or cells. In general, a microscopic analysis requires the tissues to be removed from the patient (biopsy), partly because the imaging instruments are too bulky to be used in-situ and partly because the tissues may need additional preparation such as fixation and staining.

Removing tissues or cells is undesirable for multiple reasons. First, the procedure is usually invasive and may lead to complications such as infections. Second, since the microscopic analysis is only performed *after* extraction, the surgeon has no direct feedback on whether he or she is sampling the right location. Finally, in research it is sometimes desirable to observe cells in-vivo to understand their functioning.

This led to a large body of research dedicated to deep-tissue microscopy, i.e. imaging methods that can look *through* superficial tissues and observe the microscopic details of underlying layers without extracting them. Two-photon microscopy [4] and optical coherence microscopy [5] are two examples.

There are limits to deep-tissue microscopy, though. Most biological tissues are scattering, meaning that light is randomly deflected as it travels through the tissue. This leads to an exponential loss of signal and a degradation of contrast, such that after a certain penetration

¹Of course, single-mode fibers can transmit images *indirectly* if the image is first encoded into a temporal signal (as in digital telecommunication) or into a spectral signal (as in references [2,3]). However, this requires additional optics and/or electronics on both ends of the fiber. Multimode fibers accept spatial image information *directly*.



Figure 1.3: Imaging via a fiber bundle

depth images cannot be obtained anymore. Even though filtering methods can help with the issue of contrast [6], there is a depth beyond which there are simply no more useful photons that can be extracted from the sample.

1.2.2 Fiber bundles

For the cases where the target location is not accessible using deep-tissue microscopy, an endoscopic method may be used instead to obtain microscopic images in a minimally invasive way. Optical fibers are ideally suited for this purpose, as they can guide light with negligible loss over large distances, and they are very thin.

Because individual fibers blur the images they transport (subsection 1.1.2), endoscopic fiber imaging today is usually implemented by using bundles of fibers instead. Many thin fibers are joined together in a tightly packed bundle. Each single fiber core relays light from one point of the image on the other end. Since every fiber core is spatially separated from the others, light from different locations of the object does not mix and an image can be transmitted to the other end, as shown in Figure 1.3.

Fiber bundles give an undesirable pixelated appearance to images taken through them, an effect that can be mitigated by image processing algorithms [7]. More importantly, fiber bundles are sub-optimal imaging devices from a physical point of view. Each fiber core in a fiber bundle must be sufficiently spaced from the others so that light cannot leak from one core to the next. The spacing between the cores limits the resolution [8] and light collection efficiency [9] of the system. This is especially problematic when microscopic imaging is required. Magnifying optics can be attached to the tip of bundle in order to increase the resolution. However, any increase in resolution obtained this way comes at the cost of an increase in probe size and a further decrease in light collection efficiency.

To give a numerical example, let us consider the case of a thin fiber bundle with outer diameter of $300\ \mu\text{m}$ and core spacing $3.3\ \mu\text{m}$ [10]. With these specifications, the total number of independent pixels that the bundle can resolve is 7 500 pixels. In comparison, a standard single-core fiber with a relatively low numerical aperture of 0.22 reaches already $1.5\ \mu\text{m}$ of resolution at a wavelength of 532 nm. This increases the number of resolvable pixels to 38 000 for a probe of the same size, over 5 times more than the fiber bundle. The collection efficiency of bundles is harder to compute directly, because it depends on several design parameters

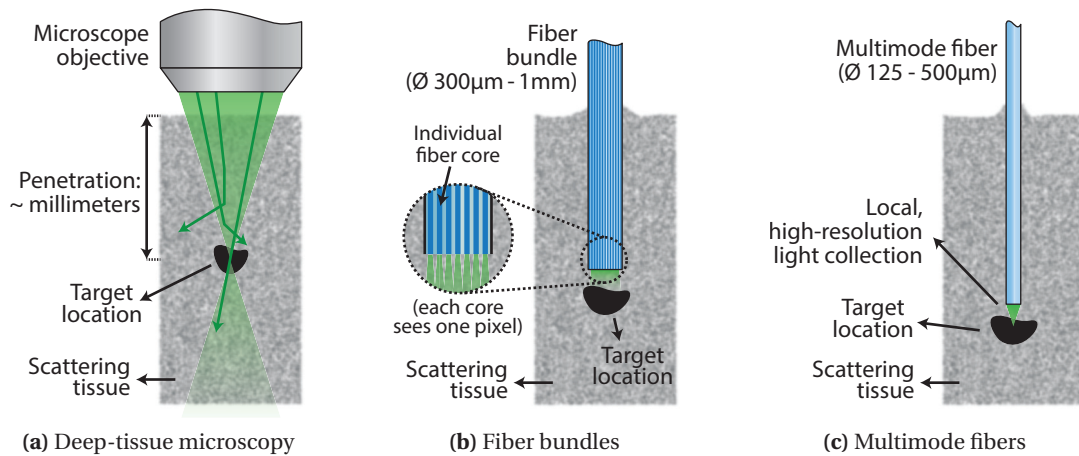


Figure 1.4: Schematic comparison of multimode fibers versus other modalities

that are rarely found in a bundle's datasheet. As an estimate [9], for a confocal fluorescence probe the light loss can exceed 90% when using bundles compared to a probe where the entire surface is light-guiding. Note, though, that double-clad multi-core fibers exist which mitigate the collection efficiency problem in bundles.

1.2.3 Multimode fiber microscopy

Transmitting images through a single multimode fiber offers a number of advantages. Step-index multimode fibers extremely thin (of the order of a few hundreds of microns), yet have a very large information capacity. Assuming modal scrambling can be compensated, no additional optics are necessary on the tip of the fiber. The whole core is light-guiding, which is beneficial for the collection efficiency of the system. This makes it possible to do high-resolution microscopy with an instrument that is itself of microscopic size.

There is no fundamental limit on the penetration depth that one can achieve, since fibers can guide light efficiently over distances of several kilometers. Tissues can therefore be probed at any depth in a minimally invasive way, for example by fixing the fiber in a small needle. Incidentally, fibers are made from inert, biocompatible and cheap materials.

In summary, multimode fibers have potential as a minimally invasive tool for microscopy in biological tissues. They can respond to the unmet need for a microscopy instrument that simultaneously has high resolution, high collection efficiency, and can be used at any location in tissue with minimal damage. These points are schematically illustrated in Figure 1.4.

1.3 Literature review

1.3.1 Scattering media

Imaging through a single multimode fiber, despite the disorderly way in which light propagates inside it, is closely related to the problem of imaging through scattering media. A brief review of the important developments in this field is in order, since they parallel similar developments for multimode fiber imaging.

A scattering medium is a medium in which light is deflected one or more times into random directions by irregularities such as particles or refractive interfaces. Common examples include fog, clouds, milk and skin. Light can travel through a scattering medium, but due to the randomization of the light rays, images are lost in the process and the medium appears opaque. Scattering media exhibit many interesting physical properties [11], and are an important topic of research because many biological tissues fall into this category [12].

Like multimode fibers, scattering materials cause a randomization of the transmitted light, but this process is deterministic and can be compensated. Early demonstrations used phase conjugation with an analog hologram² to form an image behind a scattering layer [13, 14]. More recently, light was made to focus into a point behind a scattering layer by shaping the input wavefront using a high-resolution spatial modulator and a computer-controlled feedback optimization algorithm [15]. The technique was termed *wavefront shaping*. Around the same time, a digital version of phase conjugation was demonstrated for imaging through turbid media [16].

In hindsight, the transition to digital processing of the light fields proved to be significant, because it gave much more flexibility in the way the holographic measurements could be used [17]. Holograms about scattering media could for example be stored for later use, analyzed to derive properties of the medium, modified or combined to create new patterns. More comprehensive characterizations of scattering media became possible, such as measuring transmission matrices [18–20]. This allowed identifying correlations [21–23], finding channels of maximum or minimum transmission [24–27], imaging of arbitrary patterns through a scattering layer [19, 28], increasing the imaging depth in biological tissue [6], and other applications [29–31].

Initially, many of these methods required physical access to both sides of the scattering layer. This is a problem for applications such as imaging through live biological tissue. Subsequent efforts focused on the non-invasive methods to compensate scattering, using e.g. speckle correlations [32], guide-stars [33], photoacoustics [34–37] or nonlinear approaches [38, 39].

²The term “analog” hologram refers here to a physical hologram recorded in a photosensitive material, as opposed to the digital recordings used throughout thesis.

1.3.2 Multimode fiber imaging

Wavefront shaping for fibers

Since wavefront shaping can be used to control light through a random scattering material, it can just as well be used to control light propagating through a multimode fiber. The goal in this case is different, though. When wavefront shaping is used in a scattering material (e.g. biological tissue), the purpose is usually to image what is hidden behind or inside the material. Special procedures must be used to obtain this information non-invasively. When wavefront shaping is used in a multimode fiber, the purpose is to turn the fiber into an optical relay element that can be used to transmit and receive images through it, much like a microscope objective. The fiber can for example be fixed into a small needle and used to probe targets deep inside biological tissue. Learning the optical properties of the fiber can be done in a controlled environment, requiring less involved procedures than in the case of a scattering media approach to tissue imaging.

Early work

As with scattering media, image transmission through a multimode fiber was first demonstrated in the 1960s using phase conjugation with holographic plates [40], and later with nonlinear crystals [41–45]. However, these early methods were somewhat restricted in applicability because phase conjugation reconstructs the distorted image only after it is sent back through the same fiber in reverse. In terms of endoscopy, this means that the image from inside the tissue is reconstructed inside the tissue itself, not on the experimenter's side of the fiber.

To work around this problem, one idea was to send the phase conjugated signal through an identical fiber away from the location of interest, so that the phase-conjugate reconstruction of the distorted image would appear at a location that is accessible to the experimenter [46,47]. This principle was demonstrated experimentally [48, 49], but creating an exact copy of the imaging fiber for distortion compensation proved difficult and as a result the image quality was not optimal. In addition, reliance on nonlinear mixing or photorefractive effects for phase conjugation meant that reconstructing weak signals would be troublesome [49].

Other researchers proposed to separate the fiber modes optically and correct their phases on the receiving end with a mask [50, 51]. Unfortunately, no real-world optical element is known to efficiently separate a large number of modes from a fiber with a circular core. In the case of a square core, though, this could in theory be done by a simple lens [52]. Still, this solution operates under the assumption that modes do not mix with each other, which may not always be true especially in bent fibers.

A final idea was holographic spot projection, which is illustrated in Figure 1.5. In an initial recording step, a spot is projected on one end of the fiber, and the distorted pattern is recorded holographically on the other end (Figure 1.5(a)). After this, the holographic recording can be

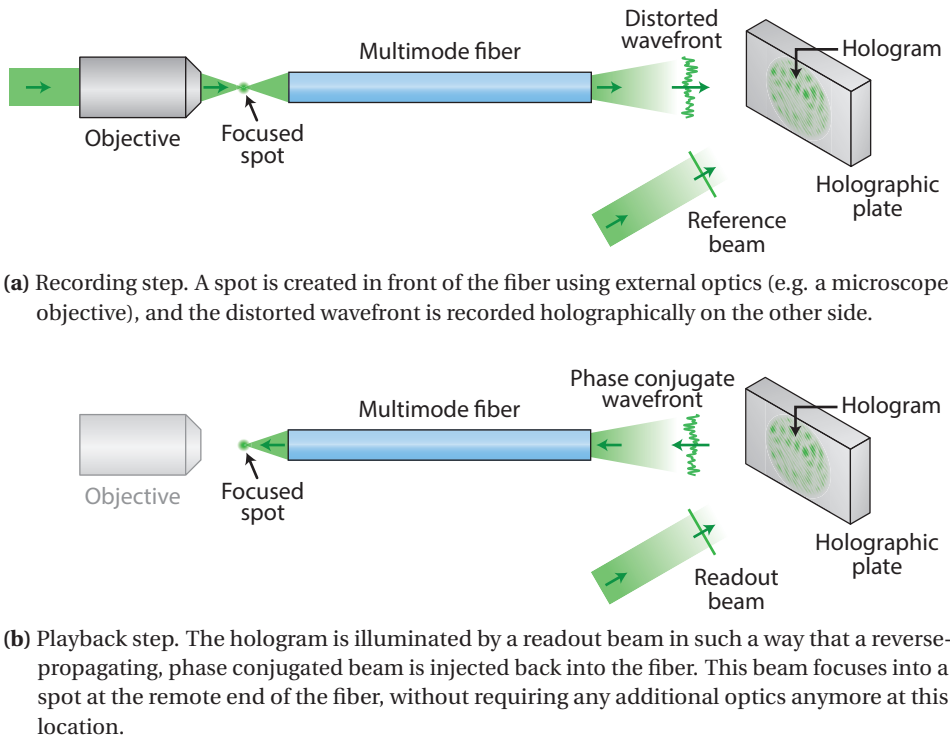


Figure 1.5: Illustration of holographic spot projection

used to recreate the spots remotely in the reverse direction by phase conjugation (Figure 1.5(b)). Multiple spots can be recorded and projected at the same time to transmit an image [53]. The difficulties here are the holographic multiplexing losses and crosstalk, which severely limit the achievable resolution and contrast. Alternatively, multiple spots at different locations can be replayed one after the other, to probe a remote sample in a spot-wise fashion [54]. Light collected back through the fiber is then used to reconstruct the image. The main obstacle for high-resolution imaging with this method is the large number of holographic recordings needed, which are technically very difficult to process when using optical means only.

Digital imaging methods

Computer-controlled wavefront shaping substantially expanded the range of possibilities of multimode fiber imaging. “Digital” experiments soon appeared where light was made to re-focus into a spot after it had traveled through a multimode fiber, using a spatial light modulators to shape the input wave. This input wavefront could be found by iterative optimization algorithms [55, 56] or more efficiently with digital holography [57–59].

Spot-scanning microscopy, which used to be impractical with analog holography, could now be implemented efficiently using digital phase conjugation [60] and transmission matrix algorithms [61–63]. A wide range of contrast mechanisms were investigated: fluorescence [60, 61, 64–67] (and variations such as light sheet [68] or saturated excitation [69] microscopy), two-

photon fluorescence [70–72], photoacoustic [66], reflection [73–75] and confocal reflection [76, 77] (see chapter 5 and chapter 6 in this thesis). Imaging is possible through a variety of waveguides: step-index multimode fibers [60–62, 65, 69, 73, 78], graded index fibers [70, 72], multi-core fibers [64, 71] and even capillary tubes [66].

In most of these demonstrations, the spot excitation and the returning signal were guided via the same fiber (i.e. an endoscopic configuration). Transmission imaging (i.e. with a different detection pathway than the fiber) was reported multiple times as well [58, 62, 67, 74, 79–81], usually as an intermediate step [58, 67, 79, 81] to endoscopic imaging, or because the purpose of the experiment was different than endoscopy [68, 74, 80].

Instead of scanning spots, a number of implementations used speckle illumination instead. Reflection imaging is then possible by averaging over many different speckle illuminations [78, 82] or by speckle-based object recognition [83]. With multi-core fibers, scanning speckles even allows to retrieve images without pre-calibrating the characteristics of the fiber [67, 84, 85].

Current topics

Next to the imaging method itself, several other aspects of multimode fiber imaging are under active research. Probably the most important one is bending: after a fiber is bent a certain amount, the propagation characteristics change and the system must be re-calibrated before imaging is possible again. This is an impediment to fully-flexible endoscopic imaging. Several authors have advocated immobilizing the fiber in a rigid needle as a solution [60, 62], which would be necessary anyway to probe sensitive areas such as the brain in a controlled fashion. Bending does not affect all types of fibers equally. In step-index multi-mode fibers, propagation is constant for deformations of the order of a few millimeters [65, 78, 86], whereas multi-core fibers allow a larger range of deformations [87, 88]. Likewise, not all types of bends are as problematic: as discussed in chapter 7, sliding a fiber through a static bend does not necessarily change the propagation characteristics in step-index fibers.

One solution to extend the bending range in the other cases is to record the fiber for multiple bending states, and load the appropriate calibration depending on feedback from a distal beacon [86]. Other efforts have focused on correcting the initial calibration using reflections from the distal facet [88, 89] or fast feedback from a photodiode [90]. In the case of graded-index fibers, the calibration can be fully determined by nonlinear feedback from a distal reference element [91]. Finally, for step-index fibers the propagation characteristics can be fully predicted from theory if the physical parameters and shape of the fiber are known [74], which could lead to new bending compensation algorithms.

Another important topic is speed. Spatial light modulators are the most commonly used devices to shape wavefronts in multimode fibers. Unfortunately, they have a rather slow temporal response (discussed further in subsection 2.2.2). To palliate for this, they have sometimes been used in conjunction with faster modulators [62, 68, 72, 79, 92, 93]. Another class

Chapter 1. Introduction

of modulators, digital micromirror devices, can reach much higher frame rates [64, 65, 90, 94] but is light-inefficient due to being restricted to binary amplitude modulation.

There is a thread of research that explores the spectral and temporal characteristics of fibers [95–99]. This can be motivated by telecommunication purposes [100], spectrometry [101–103], or imaging methods that require broadband signals such as two-photon microscopy [104]. Certain forms of imaging through fibers have been demonstrated that rely solely on spectral information [2, 3].

Finally, some attention has been dedicated to increasing the imaging resolution achievable with fibers [105–107]. Reducing number of parameters necessary for characterization [74, 108] is also a concern.

2 Digital light control

This chapter introduces the basic experimental tools used throughout this thesis: digital off-axis holography, and wavefront shaping with spatial light modulators.

Some of the material presented in this chapter can be found in the following papers:

- Damien Loterie, Salma Farahi, Demetri Psaltis, and Christophe Moser. Complex pattern projection through a multimode fiber. In *Adaptive Optics and Wavefront Control for Biological Systems*, volume 9335, pages 93350I–1 to –6, 2015.
- Damien Loterie, Salma Farahi, Ioannis Papadopoulos, Alexandre Goy, Demetri Psaltis, and Christophe Moser. Digital confocal microscopy through a multimode fiber. *Optics Express*, 23(18):23845–23858, September 2015.

2.1 Digital off-axis holography

2.1.1 Choice of the method

Modal scrambling is fundamentally a problem related to the phase of the various components of light traveling in optical fibers. To study this, it is therefore necessary to use methods which can not only characterize the amplitude distribution of a light field (as in a photograph), but also its phase (as in a hologram). We are especially interested in methods that allow recording the light distribution in digital form on a computer. This gives flexible and high-volume data processing capabilities that would be hard to achieve by purely optical means. The present section discusses only the most common methods found in the recent literature about multimode fiber imaging.

Phase shifting

In phase-shifting holography, the beam under test (also called object beam) is superposed with a reference beam, and the phase between the two is varied in successive measurements.

Chapter 2. Digital light control

By processing these holograms acquired with different phase shifts, it is possible to deduce the phase and amplitude relationship between the two beams. For stability reasons, phase shifting is typically used with a co-propagating [61,65,72,94,110] or nearly co-propagating [57,62,74,93] reference beam.

Modal decomposition

If the test beam originates from a fiber, it must be composed exclusively of the modes that are allowed to propagate inside that fiber. Therefore, the field can be decomposed in a basis of those modes. By optically correlating the output beam with each possible mode of the fiber (e.g. displayed sequentially on a spatial light modulator), one can deduce the amplitude of the modal coefficients of the beam. To find the phase, the modes still have to be compared to each other using a phase-stepping scheme, so that this method could be seen as a form of phase-shifting holography as well. The method was used in a series of studies mainly directed at telecommunication applications [97–99, 111, 112], but can be used for fiber imaging as well [113].

Off-axis holography

In off-axis holography, the reference beam is tilted at a slight angle compared to the test beam. The resulting interferogram contains the amplitude and phase information of the test beam, modulated at a carrier frequency set by the off-axis angle. This method has been used for phase conjugation experiments [60, 69, 70, 81, 114] and for the measurement of transmission matrices [76–78, 82].

Selected method

For all the holographic measurements in this thesis, the off-axis holography approach was used because it is the most economical in terms of measurements: only one camera acquisition is necessary to get the phase and amplitude distribution of a light field, while phase shifting requires two or more depending on the particular implementation. The disadvantage of off-axis holography is that it requires physical separation of the reference and object beam. This leads in practice to stability issues, which can nonetheless be overcome as will be shown in a later chapter.

2.1.2 Theory

Off-axis holography, also called Leith-Upatnieks holography [115, 116], uses the geometry shown in Figure 2.1. The object wave O (which we wish to record) is superposed with a reference wave R on a recording medium, in our case a camera sensor. The reference wave R arrives with a slight off-axis angle θ compared to the the direction of the object wave.

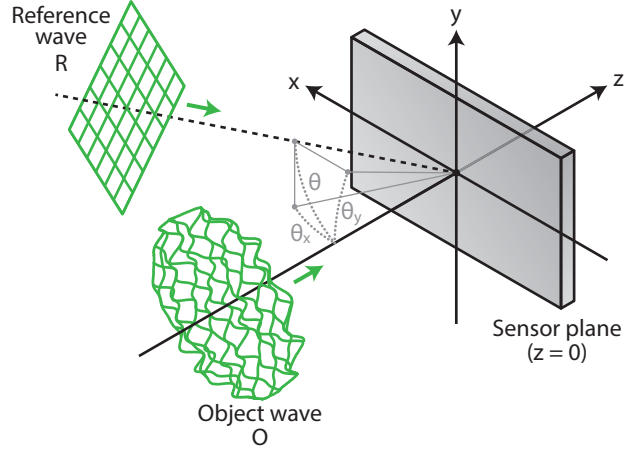


Figure 2.1: Geometry for digital off-axis holography.

Because the camera is an intensity detector, it records only the magnitude squared of the sum of both waves. This recording is called the hologram, and it is composed of the following terms:

$$\begin{aligned}
 I &= |O + R|^2 \\
 &= (O + R)(O + R)^* \\
 &= |O|^2 + |R|^2 + OR^* + O^*R
 \end{aligned} \tag{2.1}$$

Let's assume that the reference wave is a plane wave with an amplitude A . For generality, we express the reference's off-axis angle θ in 3-dimensional space using the components θ_x and θ_y , which represent the off-axis angle projected on the xz - and yz -plane respectively (see Figure 2.1). In the sensor plane ($z = 0$), the reference wave is thus written as $R(x, y, z = 0) = Ae^{jk_0(\sin\theta_x x + \sin\theta_y y)}$, and therefore the intensity distribution on the sensor is:

$$I(x, y, z = 0) = |O|^2 + |A|^2 + Ae^{-jk_0(\sin\theta_x x + \sin\theta_y y)} O + Ae^{jk_0(\sin\theta_x x + \sin\theta_y y)} O^* \tag{2.2}$$

The structure of the hologram becomes apparent when this expression is Fourier-transformed:

$$\begin{aligned}
 \mathcal{F}\{I(x, y)\}(k_x, k_y) &= \mathcal{F}\{|O|^2\}(k_x, k_y) \\
 &\quad + \mathcal{F}\{|A|^2\}(k_x, k_y) \\
 &\quad + A\mathcal{F}\{O\}(k_x + k_0 \sin\theta_x; k_y + k_0 \sin\theta_y) \\
 &\quad + A\mathcal{F}\{O^*\}(k_x - k_0 \sin\theta_x; k_y - k_0 \sin\theta_y)
 \end{aligned} \tag{2.3}$$

In other words, the object term is separated from the other terms in Fourier space by a shift $(-k_0 \sin\theta_x; -k_0 \sin\theta_y)$ which is caused by the off-axis angle. The object's conjugate can be found on the opposite side of the Fourier space, at a shift $(k_0 \sin\theta_x; k_0 \sin\theta_y)$. This is represented graphically in Figure 2.2.

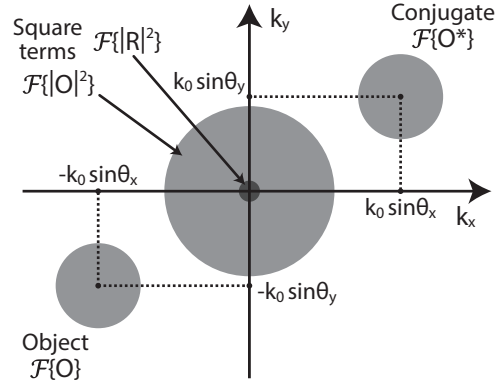


Figure 2.2: Separation of the various terms in the Fourier transform of an off-axis hologram.

2.1.3 Reconstruction procedure

Equation 2.3 suggests a simple algorithm to reconstruct the object wave from an off-axis hologram:

1. Calculate the Fast Fourier Transform (FFT) of the hologram.
2. Mask out all areas except the object term.
3. Re-center the object term in Fourier space. This step is optional. It cancels the off-axis angle of the reference beam, which would otherwise appear as a linear phase modulation on the reconstructed object wave.
4. Calculate the inverse FFT to recover the object wave in the spatial domain.

This procedure is illustrated using a real dataset in Figure 2.3.

Note that many other reconstruction algorithms exist. For example, it is possible to bypass the calculation of an FFT and an inverse FFT by using a suitably chosen spatial convolution filter instead, which may be more efficient. In the present work, the computational load of reconstructing holograms was not a limiting factor in any of the experiments, so the conceptually simple FFT-approach outlined before was used to process all the holograms.

2.1.4 Practical aspects

Off-axis angle

What should be the angle between the reference beam and the object beam? The optimal angle θ is determined by two conditions:

- *Sampling period of the sensor.* For a sensor with a sampling period (i.e. pixel pitch) of L_{pixel} , the two-dimensional region of spatial frequencies that can be properly sampled is $(k_x, k_y) \in [-\frac{\pi}{L_{pixel}}; \frac{\pi}{L_{pixel}}] \times [-\frac{\pi}{L_{pixel}}; \frac{\pi}{L_{pixel}}]$ (Nyquist frequency). The object's spatial frequency content must fit inside this region in Fourier space.

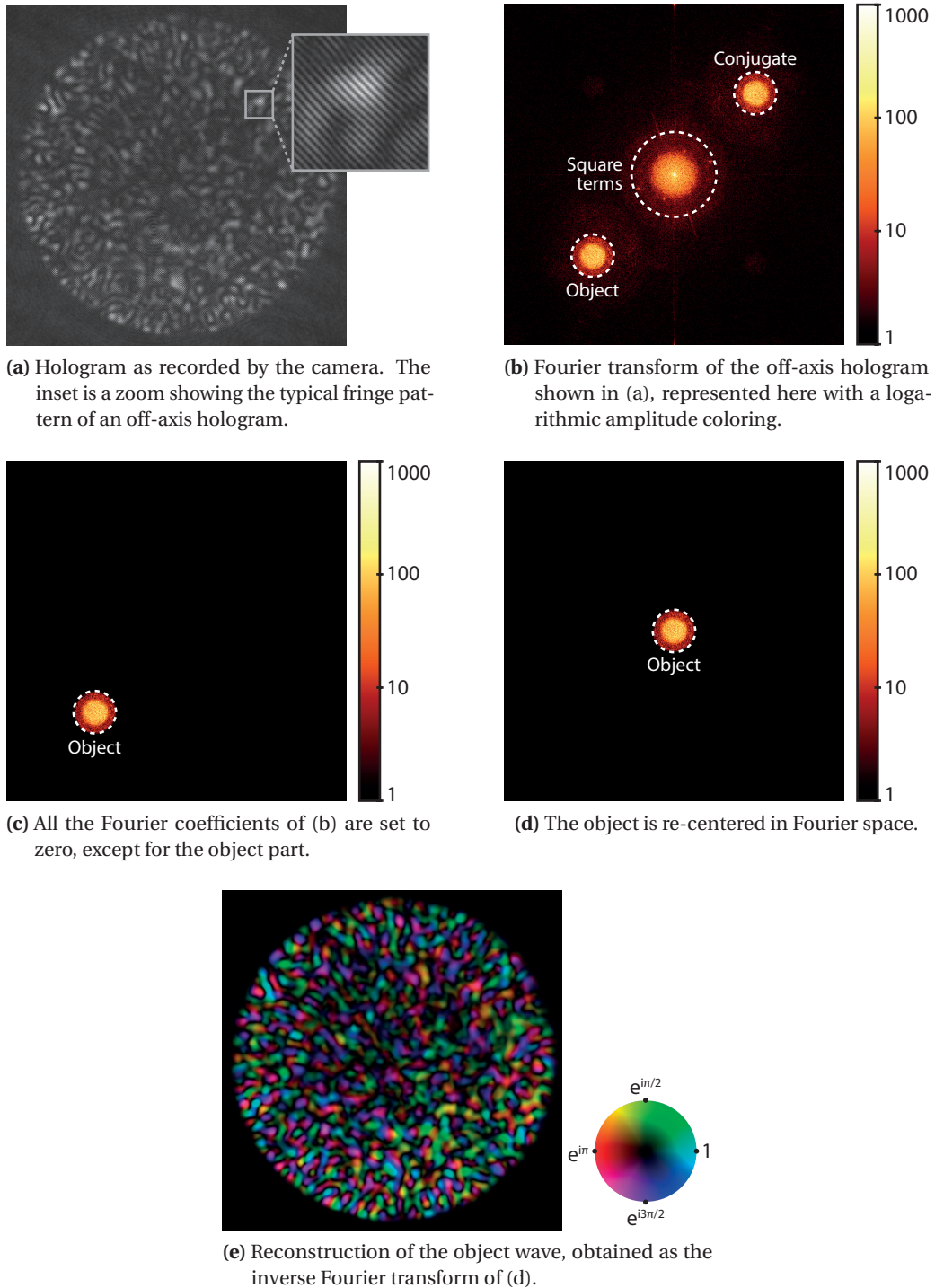


Figure 2.3: Reconstruction of a speckle pattern from its hologram at the output of a fiber.

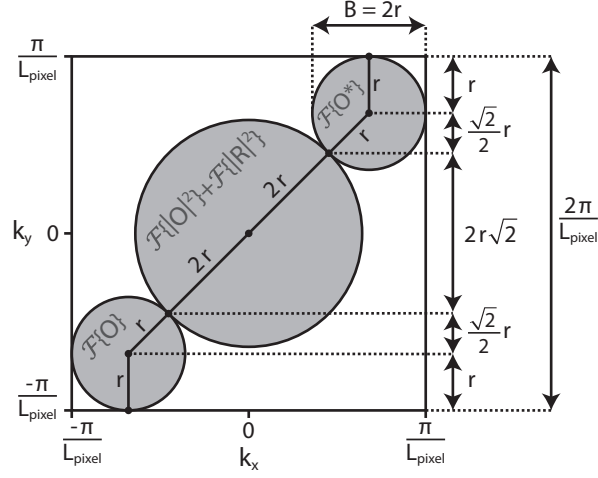


Figure 2.4: Fourier-space derivation of the optimal angle for the reference beam.

- *Maximal bandwidth without overlap.* We are looking for the maximal spatial frequency bandwidth B of the object content that does not cause overlap with the other terms in Fourier space (refer to Figure 2.2). Note that the square term of the object has bandwidth $2B$.

The most efficient layout of the various components in Fourier space under these conditions is shown in Figure 2.4. From simple geometric considerations, the following formula can be derived for the maximum object bandwidth $B = 2r$:

$$\begin{aligned}
 \frac{2\pi}{L_{pixel}} &= (2 + 3\sqrt{2})r \\
 &= \left(1 + \frac{3}{2}\sqrt{2}\right)B \\
 \rightarrow B &= \frac{2\pi}{1 + \frac{3}{2}\sqrt{2}} \frac{1}{L_{pixel}}
 \end{aligned} \tag{2.4}$$

From the same Figure 2.4, we find that the off-axis reference angle corresponds to a spatial frequency $k_{ref} = 3r = \frac{3}{2}B$. Using the relationship $k = \frac{2\pi}{\lambda} \sin \theta$, we obtain:

$$\begin{aligned}
 \sin \theta_{ref} &= \frac{\lambda}{2\pi} k_{ref} \\
 &= \frac{\lambda}{2\pi} \frac{3}{2} B \\
 &= \frac{3}{2 + 3\sqrt{2}} \frac{\lambda}{L_{pixel}}
 \end{aligned} \tag{2.5}$$

$$\rightarrow \theta_{ref} [^\circ] \approx 27.5 \frac{\lambda}{L_{pixel}} \tag{2.6}$$

where the approximation 2.6 in degrees is accurate to within 1% for $L_{pixel} \geq 2\lambda$. The relation-

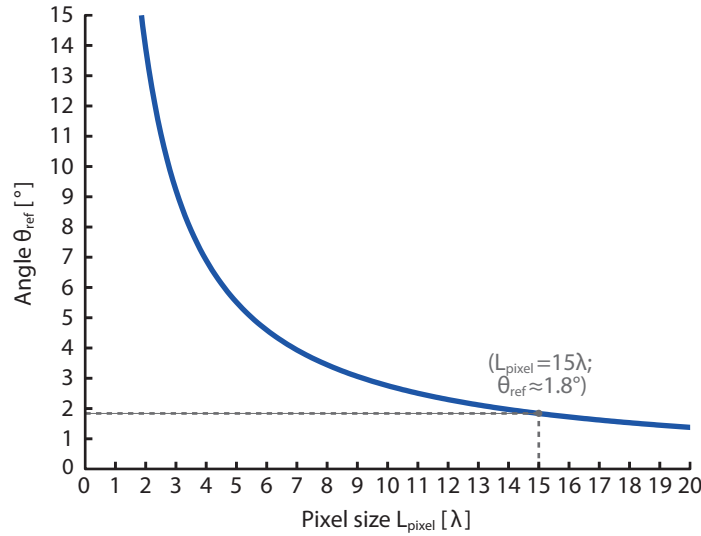


Figure 2.5: Optimum off-axis reference angle θ_{ref} versus pixel pitch of the camera sensor L_{pixel} . Note that the axis L_{pixel} is in units of the working wavelength (e.g. $L_{pixel} = 15\lambda$ means approximately $8\mu\text{m}$ at 532nm).

ship 2.5 between the angle θ_{ref} and the pixel pitch L_{pixel} is plotted in Figure 2.5. Sensors with large pixel sizes require shallow off-axis angles; in practice, this may require combining the object and reference waves via a beam splitter instead of superposing them directly.

Aliasing

It is important to correctly estimate the required off-axis angle, because an experimental determination can be misleading. When the angle is increased so much that the object term crosses the boundary of the discrete Fourier domain, the object term does not simply disappear but it is replicated on the other side of the Fourier domain instead. This phenomenon is known as aliasing [117], and can occur in any sampled measurement. It is illustrated in Figure 2.6.

The non-zero extent of the camera pixels causes a spatial averaging (low pass) filtering of the aliased replica, leading to a significantly reduced signal-to-noise (SNR) ratio. For this reason, aliasing is undesirable and should be avoided. It is difficult to tell if aliasing has occurred only by looking at the recorded hologram. Experimentally, there are two solutions:

- Manually measure the off-axis angle between object and reference in the far field (without a camera), and make sure this angle is correct.
- Start from a state where object and reference are perfectly superposed (zero angle). Then, slowly increase the off-axis angle of the reference using adjustable mirrors, while monitoring the Fourier transform of the camera hologram to make sure the object terms stays within the boundaries.

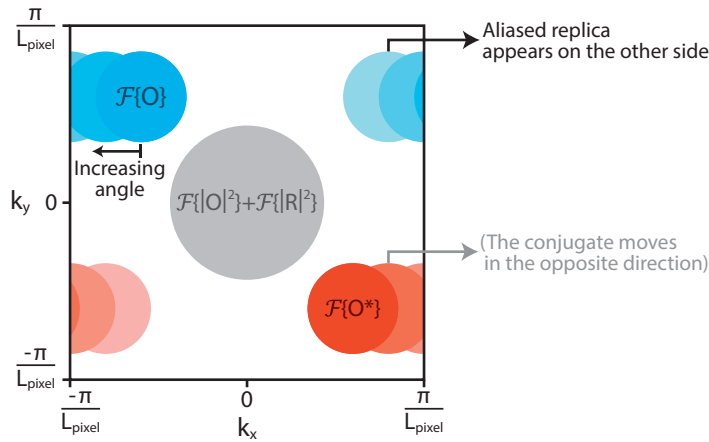


Figure 2.6: Aliasing when the off-axis angle shifts the object beyond the Fourier boundaries.

2.2 Liquid crystal phase modulators

2.2.1 Choice of the modulator

Creating specific illumination patterns at the output a multimode fiber requires a device that can create or “shape” arbitrary wavefronts at the input of that fiber, i.e. spatial light modulators (SLM). This section briefly reviews the various types of modulators encountered in the recent multimode fiber imaging literature.

Liquid crystal modulators

A common type of modulator is the liquid crystal phase-only modulator [118]. The orientation of the birefringent liquid crystals inside each pixel is controlled by an electric signal, thereby varying the phase delay imparted by each pixel to the incoming beam of light. The response time of these devices is of the order of 20 Hz to 200 Hz. They suffer from a number of problems such as flicker, non-flat active areas, and nonlinear modulation characteristics which must be calibrated. This is discussed further in subsection 2.2.2 and subsection 2.2.3. The strong points of SLMs are a high resolution, a high precision (bit-depth) of modulation, and good light efficiency.

Phase-only SLMs have mostly been used to create and scan spots through multimode fibers for fluorescence [60–62, 68, 69], reflection [73, 74, 76, 77], photoacoustic [81, 114] and two-photon [70, 72] microscopy. In general, liquid crystal phase modulators give the flexibility to generate any kind of patterns [68, 77, 93, 99, 111].

To increase the effective speed of modulation, multiple holograms can be loaded during each refresh cycle of the SLM. These holograms can then sequentially be addressed using a fast angle-scanning device such as an acousto-optic deflector [62, 92, 93]. Combinations of phase-only SLMs with fast galvo scanners [79] and deformable mirrors [72] have also been

reported for imaging through multi-core fibers.

Digital micromirror devices

A digital micromirror device (DMD) is an array of micromirrors that can individually be turned into an “on” or “off” state. The angle between both states is usually 24° . When a micromirror is “on” the light is reflected into the beam path, and when it is “off” the light is deflected out of the beam path. This achieves a binary amplitude modulation. The binary constraint on the modulation is very limiting, but DMDs have the advantage of reaching modulation speeds over 20 kHz and do not suffer from flicker [119].

Phase and amplitude information can be encoded in a binary pattern using the Lee method [119–122] or by pixel-combining approaches [123, 124]. This makes it possible to use DMDs to focus light through fibers [90, 94, 105, 108] and implement fast spot-scanning fluorescence microscopy [64, 65]. The disadvantages of using DMDs in this way are the poor light-efficiency (a few percent) and the reduced effective resolution.

Selected modulator

Liquid crystal phase modulators were used in all experiments described in this thesis. Since they are phase devices, they can precisely and efficiently create linear phase gradients. This allowed the accurate measurement of transmission matrices in a Fourier basis (as will be further explained in chapter 3). Another main reason for the choice of the phase-only SLMs is the high light-efficiency, without which some experiments (such as confocal imaging in chapter 5) would not have been possible. Finally, the higher effective resolution of phase SLMs compared to DMDs (where pixel-combining methods are needed to obtain phase modulation) allowed measurement of a wider range of fibers, as will be explained in section 2.3.

2.2.2 Temporal response

Understanding the temporal response of typical liquid crystal modulators is crucial to the success of experiments requiring a high number of pattern projections in a short time (e.g. the transmission matrix in chapter 3). In practice, three effects must be taken into account: delay, response time and flicker. These are illustrated in Figure 2.7 using experimental data obtained with the SLM used throughout this work (HoloEye Pluto VIS).

Delay

SLMs are usually controlled by a computer via a graphical link or a dedicated interface. When a command is executed on the computer to load a new phase mask, this phase mask does not appear instantaneously on the device. There is a delay that can last up to several refresh cycles of the SLM.

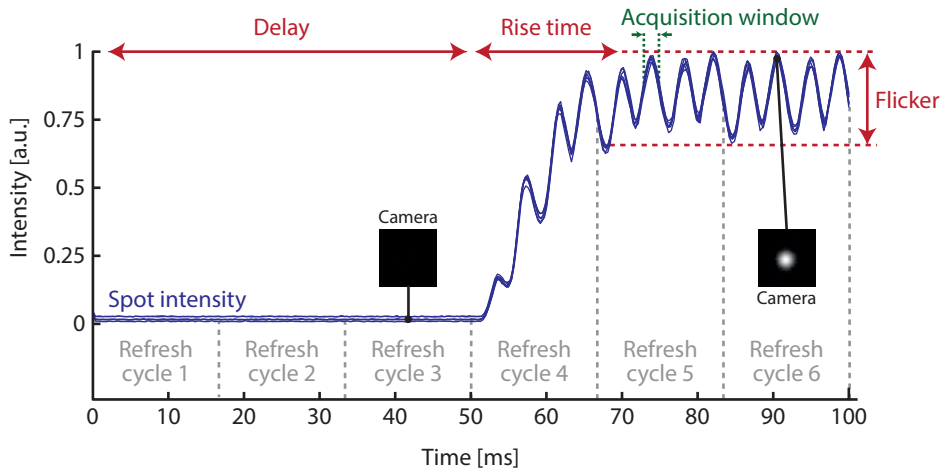


Figure 2.7: Temporal response of the SLM (HoloEye Pluto VIS). At time 0, a phase mask is rendered by the computer’s graphics processing unit. The phase mask is designed to create a spot through a multimode fiber. A camera observes the delay and buildup of the spot intensity at a frame rate of 3 kHz. The multiple intensity traces correspond to multiple repetitions of this experiment. The refresh cycles are shown based on the synchronization (vsync) signal of the SLM.

It is important to take this delay into account, especially when using SLMs in combination with acquisition devices such as cameras for off-axis holography. Otherwise, the camera may acquire holograms before any pattern is displayed on the SLM, or it may acquire holograms corresponding to previously displayed patterns, leading to inconsistent data.

Part of the delay is caused by buffering inside the SLM’s driving electronics and is constant. For SLMs with a graphical link, an additional source of delay is the computer’s graphics processing unit which usually has its own double- or triple-buffering mechanism to improve visuals in 3D applications. This type of buffering is unnecessary for SLMs and can cause very large timing inconsistencies with certain graphics cards. It should therefore be disabled if possible, and SLM phase masks should be loaded using code with sufficiently low-level access to the graphics rendering pipeline to ensure consistent timing. Finally, another source of delay inconsistencies is the preemptive multitasking mechanism implemented in most modern operating systems. It interrupts running processes unpredictably after certain time slices (usually of the order of 10 ms). This can be mitigated by tweaking process priorities and using graphics API calls that proactively yield processor time when the application is waiting for a new refresh cycle.

Response time

For phase modulation to occur, the liquid crystals inside each pixel must be physically re-aligned using an electrical signal. This realignment suffers from a certain viscosity, such that

the response is not immediate. This is the rise time illustrated in Figure 2.7. The response time limits the effective frame rate of the modulator to maximum 30 Hz with our modulator.

Flicker

Once the phase mask has been loaded, a periodic flickering of the phase pattern is observed. The origin of flicker is the electronic pulse modulation signal used to address the pixels [125], and is reduced in more recent modulators by improved and higher-frequency addressing schemes. In our case, the flicker is quite significant since it causes intensity fluctuations of over 30% when spots are created through an optical fiber Figure 2.7.

Synchronization

To alleviate artifacts due to the aforementioned problems, a combination of software and hardware synchronization mechanisms coordinated the camera with the refresh cycles of the SLM.

The software used throughout this thesis is a purpose-written C++ application, addressing the graphics card (AMD FirePro V4900) via the DirectX 11 graphics application interface on Windows 7. The application is based largely on publicly available source code [126], modified to generate hardware synchronization signals via an acquisition card (National Instruments PCIe-6323) and to communicate with a separate numerical processing software (MATLAB).

Each time a new frame is loaded by this application, a pulse is scheduled on the acquisition card. The pulse is scheduled only after a specified number of refresh cycles (corresponding to the buffering delay), and is ultimately triggered by the synchronization (vsync) signal of the SLM. This allows targeting a precise moment in the refresh cycle of the SLM when the phase mask is optimal, even when many phase masks are displayed in a rapid sequence. The interval used for most measurements in the following chapters is denoted as the “acquisition window” in Figure 2.7.

2.2.3 Other non-idealities

Besides the non-ideal temporal response of liquid crystal SLMs, several other effects cause deviations from the expected behavior. A brief overview is given below, for reference.

Phase response curve

Liquid crystals have a nonlinear phase response to the electrical modulation signals. In addition, this response depends on the operating wavelength. To linearize the response, a calibration is needed using one of various methods [127–129]. This calibration must be done for each new wavelength the SLM is used at. For the SLMs used in this thesis, the

calibration was done using off-axis holographic measurements. The response of the SLM can vary across different regions of the device [130–133]. It can also include an undesired amplitude modulation [127]. These last two effects were not corrected.

Aberrations

SLM panels are usually not perfectly flat [134–136], because of limitations in the manufacturing process. With phase SLMs, this can be corrected simply by measuring the wavefront distortion and adding an opposite phase shift to the displayed patterns. More general correction methods [137] can compensate other defects in the optical train at the same time, such as a non-flat illumination beam or lens aberrations. The transmission matrix method (see chapter 3) used in this thesis naturally compensates all these distortions as well.

Diffraction effects

Another typical problem is the appearance of multiple orders of diffraction when displaying simple phase gratings on phase SLMs. A first set of diffraction orders is simply due to the pixelated structure of the device: the pixels form a regular grating, from which light is diffracted at regularly-spaced angles related to the grating period (i.e. pixel pitch). This happens even when the SLM is off. Second, when displaying a phase pattern, not all of the light is modulated and some of the incoming light is simply reflected from the SLM panel. This is usually called the zero-order component.

Both preceding types of unwanted diffraction orders can be suppressed by spatial filtering. First, a small angle should be imparted to the desired phase pattern, to separate it from the zero-order reflection. This is done by multiplying the SLM phase pattern by a linear phase grating $e^{i(k_x x + k_y y)}$ where (x, y) are the spatial coordinates and (k_x, k_y) are the spatial frequencies defining the angle. This multiplication is equivalent to a shift of the Fourier coefficients away from the center of the Fourier transform of the pattern. The angle imparted to the pattern should then be compensated by physically rotating the SLM. This way, the desired phase pattern is aligned on the optical axis, but the zero order component (reflection) propagates slightly off-axis. Finally, this zero-order (and any other unwanted orders) can be blocked away for example by using an aperture in the Fourier plane of a lens. In this work, spatial filtering was carried out instead by exploiting the finite numerical aperture of the optical fibers: the waves with higher angles are not guided through the fiber, which allows blocking the undesired diffraction orders.

Some other diffraction orders are due to multiple reflections inside the display [138] and to the quantized nature of the phase modulation (256 bit in our case). An illustration is shown in Figure 2.8. The SLM panels are also slightly scattering. This last set of unwanted light components cannot be completely blocked off, but usually represents only a small fraction of the signal.

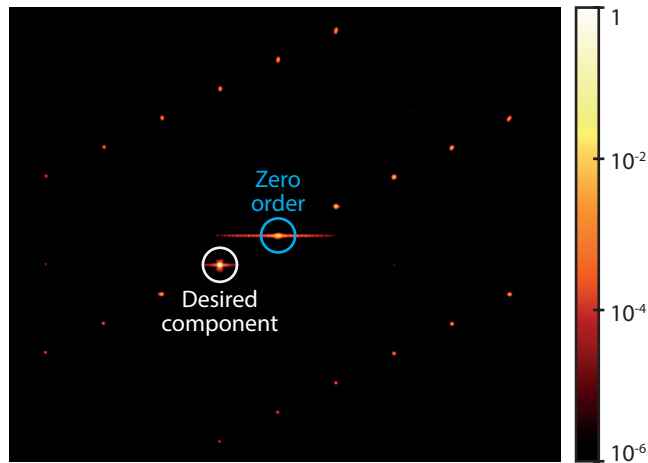


Figure 2.8: Unwanted diffraction orders. A linear phase grating is displayed on the SLM, and the modulated light is observed in the Fourier plane of a lens. Next to the desired component (corresponding to the displayed grating) and the expected zero-order, additional diffraction orders are present.

2.2.4 Amplitude coding

Phase-only modulation is the most effective modulation scheme when the experimenter’s goal is to focus as much light as possible through a distorting medium into a single point¹. It has successfully been applied several times for this purpose through multimode fibers [55, 57, 59].

When the goal is instead to obtain accurate patterns, with both a high signal and a low background noise over the whole field of view, then modulating the amplitude in addition to the phase becomes necessary. Methods found in the multimode fiber imaging literature include algorithms such as Gerchberg-Saxton [57, 61, 77, 93] or simulated annealing [100]. Other schemes exist using one [139–143] or two [144–146] SLMs.

Here, the Gerchberg-Saxton algorithm is described since it was used for various experiments in the course of this work. In general, the Gerchberg-Saxton algorithm is used to calculate a complex field that respects certain constraints both in the spatial domain and the Fourier domain [147]. These constraints are applied iteratively until a satisfactory solution is found. In this case, the constraint in the spatial domain is that the complex field should be “phase-only”, i.e. it should have everywhere a constant amplitude. The constraint in the Fourier domain is that the Fourier coefficients compatible with the numerical aperture of the fiber are fixed. These coefficients describe the field that the experimenter wants to inject into the fiber. All the other Fourier coefficients can be freely adapted by the algorithm since they correspond to plane waves outside the acceptance angle of the fiber’s core.

¹Mathematical explanation: Assume that x_n is the input modulation at input pixel n , y_m is the spot amplitude at output pixel m , and both are linearly related by $y_m = \sum t_{mn} x_n$ (transmission matrix model, see also chapter 3). Given that the input coefficients x_n cannot exceed unity (modulators provide no gain), the optimal strategy to maximize $|y_m|$ is to use the pixels x_n to cancel the phase of the coefficients t_{nm} , so that all terms in the sum add up coherently: $x_n = e^{-i \arg t_{nm}} \Rightarrow y_m = \sum |t_{mn}|$. This is a phase-only solution.

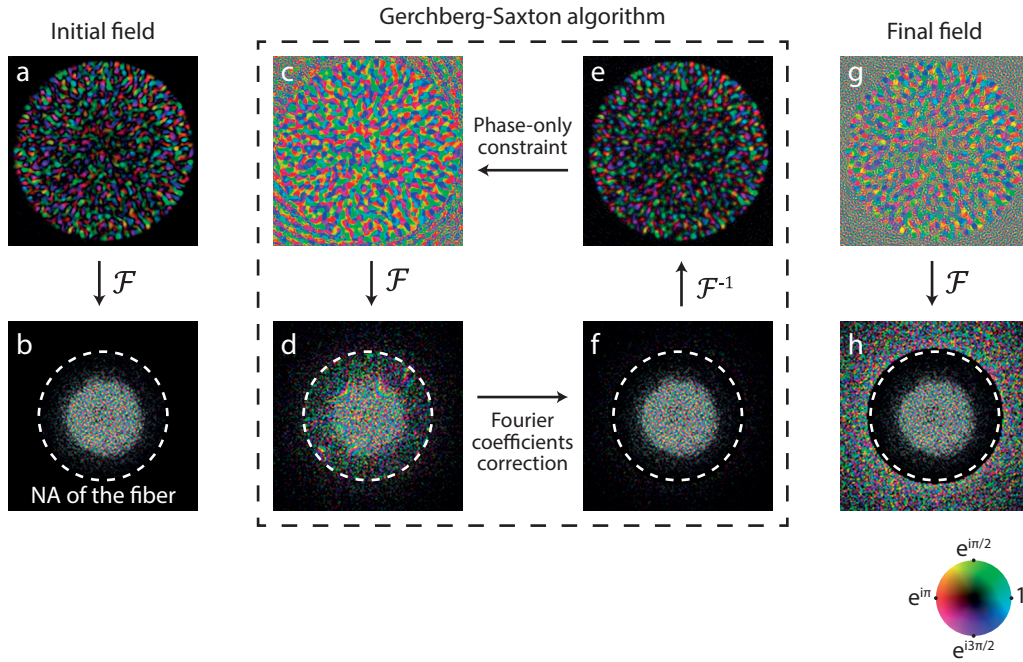


Figure 2.9: The Gerchberg-Saxton algorithm to encode amplitude in phase-only images.

This process is illustrated in Figure 2.9. The initial field is shown in (a) and its Fourier transform in (b). The Fourier transform is a decomposition into plane waves with varying angles with the optical axis. In the Fourier domain, two zones can therefore be distinguished with respect to the fiber: there are coefficients corresponding to plane waves within the numerical aperture (NA) of the fiber, and plane waves outside the NA of the fiber. The boundary between both zones is shown with a dashed line. In the first step of the algorithm (c), the field is made phase-only in the spatial domain by setting the amplitude of each pixel to 1. In the Fourier transform (d), this phase-only operation creates additional components outside the NA of the fiber, and also distorts the components within the NA of the fiber. The second step of the algorithm (e) is to correct Fourier coefficients that were distorted by the phase-only operation. Here, these coefficients are simply replaced with the undistorted coefficients of the initial field within the NA of the fiber. The coefficients outside the NA of the fiber are left as calculated by the algorithm; their value can be freely modified since this corresponds to light that will not be guided by the fiber. In the spatial domain (f), the correction of the Fourier coefficients has recreated a non-constant distribution of amplitude. The process (c) to (f) is therefore repeated for several iterations. After 50 iterations, a phase-only field is obtained as shown in (g). The final field has the desired Fourier components within the numerical aperture of the fiber as shown in (h). Note that in this example dataset, the fields (a), (c), (e), (g) and their Fourier transforms (b), (d), (f), (h) have a resolution of 800 by 800 pixels, but for clarity only the central 125 by 125 pixels of the Fourier transforms are shown in (b), (d), (f), (h).

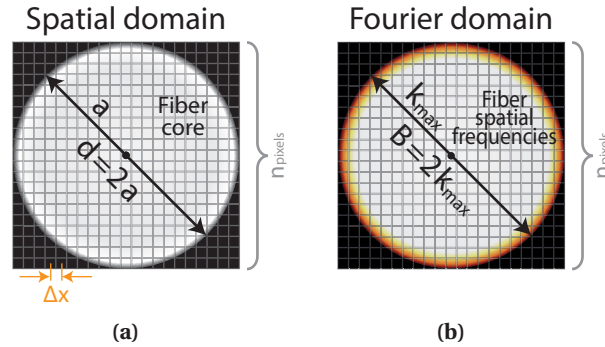


Figure 2.10: Definitions for the derivation of the required number of pixels. (a) Spatial domain and (b) Fourier space. The grid overlay represents sampling.

2.3 Resolution

Cameras and spatial light modulators are devices with a finite number of pixels. How many pixels are needed for fiber imaging? And how tightly spaced must these pixels be?

To answer the first question, we will make some assumptions. First, we assume that the light coming in or out of the fiber is limited in spatial extent to a diameter d (i.e. the core diameter). We will also assume the light signal is band-limited² to spatial frequencies below $k_{max} = \frac{2\pi}{\lambda_0} NA$, where NA is the numerical aperture and λ_0 is the optical wavelength in vacuum.

We are looking for the number of pixels that is just sufficient to record the complete field of view (core) and the spatial frequency space (numerical aperture) of the fiber, as shown in Figure 2.10. The spatial frequency bandwidth $B = 2k_{max}$ of the optical signal determines the required sampling interval:

$$\begin{aligned} \Delta x &= \frac{2\pi}{B} \\ &= \frac{\pi}{k_{max}} \\ &= \frac{\lambda_0}{2NA} \end{aligned} \tag{2.7}$$

The sampling interval (2.7) corresponds to the classical diffraction limit, as expected. Combined with the known spatial size d of the light distribution, we can now determine the

²Physically, a signal cannot be limited both in spatial and in frequency extent due to the uncertainty principle. The limits are to be understood here in an approximate sense as boundaries defining the important part of the light distribution, outside which the signal is negligible.

required number of pixels along each dimension of the device:

$$\begin{aligned}
 n_{pixels} &= \frac{d}{\Delta x} \\
 &= \frac{2}{\lambda_0} d NA \\
 &= \frac{2}{\pi} V
 \end{aligned} \tag{2.8}$$

In the last row of (2.8), the dimensionless parameter $V = \frac{2\pi}{\lambda_0} a NA$ is inserted (where $a = \frac{d}{2}$ is the radius). This V-number is commonly used in the context of multimode fibers, but the formulas derived in this section are valid in general for any type of optical field with specified λ_0 , d and NA . Note that n_{pixels} is the *side-length* of the device in pixels, and the total number of pixels is therefore n_{pixels}^2 . Using (2.8), one can e.g. calculate that controlling or observing light in a fiber with a V-number of 100 requires a device (SLM or camera) of at least 64×64 pixels.

The derivation above assumes that all of the device's frequency space is available to process the light distribution. This is not the case in off-axis holography [148], as illustrated in Figure 2.4 on p. 16. Also with spatial light modulators it is sometimes necessary to sacrifice a certain amount of resolution e.g. to implement multi-pixel phase and amplitude modulation schemes on constrained (phase-only or binary) devices, or to separate the output wave from undesirable zero-order reflections using a tilt (shift in frequency space). Table 2.1 summarizes the minimum number of pixels under various conditions. Note that in practice one must allow an extra experimental margin on top of those numbers, to facilitate alignment.

Case	Criterion	Pixel side-length	Approximation
Ideal case	Object fills exactly 100% of the spatial and frequency space of the device.	$\frac{2}{\pi} V$	$0.64V$
Phase-only SLM	Double resolution, to allow for amplitude modulation schemes and to shift wavefront away from the zero-order reflection.	$\frac{4}{\pi} V$	$1.3V$
Off-axis holography	Optimal frequency space layout without overlap (Figure 2.4), for one or two object beams.	$\frac{2+3\sqrt{2}}{\pi} V$	$2.0V$
Binary SLM	Quadruple resolution for superpixel-based modulation or Lee holograms.	$\frac{8}{\pi} V$	$2.6V$

Table 2.1: Lower bounds on the number of pixels required (along each dimension of the device), in function of the V-parameter.

Concerning the second question, i.e. the required pixel spacing, this parameter is usually fixed and depends on the choice of the device. Typically, it is many times larger than the sampling period found with Equation 2.7, so that the fiber output must first be magnified before being imaged on the device. This magnification scales the spatial extent d and the numerical aperture NA in inverse proportions³, so that the required number of pixels in Equation 2.8 remains the same overall. The magnification factor should be large enough to use at least the minimum number of pixels of Table 2.1 on the device, and small enough not to exceed the device's active area.

³Here we assume that an afocal magnification system is used. It must map plane wave inputs to plane wave outputs, with no change in convergence or divergence compared to the incoming beam. This is the case e.g. for an infinity corrected objective and a tube lens aligned in a 4f-configuration. For a more general discussion of other cases, refer to [148].

3 Transmission matrix

This chapter introduces the method used to characterize and control light propagation in optical fibers: the transmission matrix.

Some of the material presented in this chapter can be found in the following papers:

- Damien Loterie, Salma Farahi, Demetri Psaltis, and Christophe Moser. Complex pattern projection through a multimode fiber. In *Adaptive Optics and Wavefront Control for Biological Systems*, volume 9335, pages 93350I–1 to –6, 2015.
- Damien Loterie, Salma Farahi, Ioannis Papadopoulos, Alexandre Goy, Demetri Psaltis, and Christophe Moser. Digital confocal microscopy through a multimode fiber. *Optics Express*, 23(18):23845–23858, September 2015.

3.1 Theory

3.1.1 Introduction

The first step in controlling light in a multimode fiber is to know how light is transformed between the fiber’s input and output. This is done in this thesis with the transmission matrix.

The transmission matrix is a concept derived from the scattering matrix commonly used in physics. In this framework, the process under study is described by an “incoming” wave Ψ_{in} and an “outgoing” wave Ψ_{out} which are related by a linear operator S . If the states are expressed as vectors in a suitably chosen basis, the relationship is a matrix operation $\Psi_{\text{in}} = S\Psi_{\text{out}}$, where S is called the S-matrix or scattering matrix [149, 150].

In general, the S-matrix allows interactions in any direction. For example, a traveling wave coming in from a source direction is allowed to scatter or reflect back towards the source. If reflections are neglected and only waves transmitted forward between a source and a detector plane are considered, then only a part of the full scattering matrix is needed. This is the transmission matrix [18, 19]. The notation used in this chapter is $Y = TX$, where X and Y are

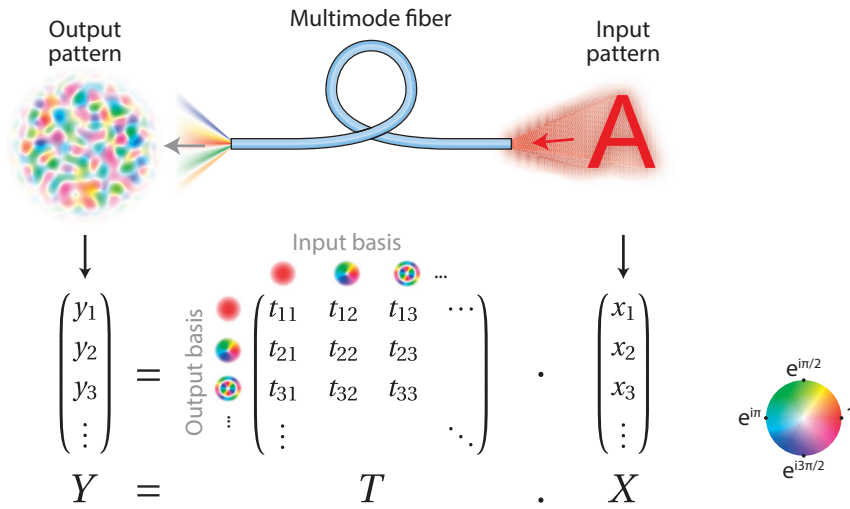


Figure 3.1: The transmission matrix model for multimode fibers. The input pattern X is injected into the fiber, where it undergoes a transformation T , and exits as the output pattern Y . X and Y are a vectors of complex coefficients describing the optical fields at input and output respectively in a suitable basis. In this illustration, the input and output bases consist of the fiber modes, but other choices are possible too. T is the transmission matrix relating the input coefficients X and the output coefficients Y .

the complex field values at input and output respectively, and T is the transmission matrix. This is illustrated for fibers in Figure 3.1.

Multimode fibers fit well in the framework of transmission matrices. They exhibit negligible backscattering and have a finite set of modes, so they can be completely described by a transmission matrix of finite size¹. In addition, barring any deformation, fibers are stable in time [114, p. 47-49] and do not exhibit decorrelation as in biological media [151–153].

The transmission matrix model does not make any assumptions about the process under study, other than a linear relationship between input waves and output waves. In a certain sense, this is too general for optical fibers because the propagation of modes can be predicted from theory using a small set of physical parameters [74], whereas the matrix approach requires a very large number of parameters (allowing any input-output transformation to take place). Nevertheless, the transmission matrix is convenient in practice because in addition to modal scrambling it can capture common imperfections in experimental setups, such as misalignments, aberrations, or even the refractive transition from fiber to air [154], effects which must otherwise be modeled. The matrix is also useful with a variety of fibers, such as multi-core fibers [155] or graded index fibers [72], for which propagation properties are more difficult to predict.

¹This assumes monochromatic light. Modes vary with wavelength, so multispectral transmission matrices grow in size proportionately to the wavelength interval [99].

Experimentally, the matrix is measured by applying a set of inputs one by one to the system with a spatial light modulator (SLM), and recording the corresponding output fields holographically [18]. The transmission matrix is then able to predict any future output by linear combination of the known input-output measurements.

3.1.2 General properties

Scattering matrices obey certain useful properties depending on the system under consideration [150, p. 5-7]. Assuming energy conservation, the scattering matrix is unitary: $S^\dagger = S^{-1}$. In a reciprocal system, the scattering matrix is symmetric: $S = S^T$. These two properties hold for theoretical scattering matrices in general. This section discusses how they apply in the case of experimentally measured transmission matrices of fibers. It also discusses properties specifically related to fibers.

Unitarity

When using a transmission matrix model instead of the full scattering matrix, we neglect the reflection component. In theory, an optical fiber features no reflections or backscattering, so that its idealized transmission operator remains unitary on its own as well [74]:

$$T^\dagger = T^{-1} \tag{3.1}$$

Experimentally, however, there are certain caveats. Unitarity requires conservation of energy. Therefore, every possible way in which light can be transmitted through the system must be mapped out and observed without loss. Experimentally, this is not feasible for multiple reasons. Limitations in the optics or the measurement apparatus can cause losses. Light may be coupled out of the fiber due to bends, inhomogeneities, or simply when the input exceeds the fiber's numerical aperture. Only a single polarization may be measured, for experimental convenience, leading to an incomplete transmission matrix. The matrix may be described in a basis with more degrees of freedom than the fiber it describes. All these effects cause "lossy" channels to appear in the experimental transmission matrix, so that it is not strictly unitary in practice [74, 99].

Reciprocity

Reciprocity makes the *scattering* matrix symmetric, but this does not imply that the *transmission* matrix is symmetric. Reciprocity says that a coupling between an input wave n and an output wave m occurs with the same amplitude and phase when the process is reversed (i.e. when the output is sent back through the system exactly as it came) [150]. For transmission matrices, this means that the matrix for one direction $T_{A \rightarrow B}$ is the non-conjugate transpose of

the matrix in the opposite direction $T_{B \rightarrow A}$, as described by Equation 3.2.

$$T_{A \rightarrow B} = T_{B \rightarrow A}^\top \quad (3.2)$$

Note that the two matrices operate on a different set of basis vectors. Since $T_{B \rightarrow A}$ describes the reverse propagation process, its basis vectors are the time-reversed² versions of the corresponding basis vectors of $T_{A \rightarrow B}$. As a simple illustrative example with one input mode and one output mode: if $T_{A \rightarrow B}$ describes the conversion of a plane wave into a converging spherical wave, both traveling in the $+z$ direction, then $T_{B \rightarrow A}$ describes the conversion of a diverging spherical wave into a plane wave, both traveling in the $-z$ direction.

In certain respects, reciprocity is more robust to experimental imperfections than unitarity. Reciprocity holds even in the presence of loss or gain. More generally, it applies in linear, time-invariant materials with symmetric dielectric and magnetic tensors [156]. This is the case in all the experiments presented in this work. The main difficulty in exploiting reciprocity is the requirement to swap the places of the source (spatial light modulator) and the detector (camera) exactly in order for the reverse transmission matrix $T_{B \rightarrow A}$ to be valid. As will be shown later in section 4.3, this is not a trivial problem in practice.

Limited mode coupling

Step-index fibers possess a specific set of propagation-invariant modes (see Appendix A). Mode coupling (i.e. the transfer of energy between different modes) is limited in general. It happens only in bent fibers, and is proportional to the curvature of the bends and the interaction length. Consequently, the matrix is sparse if expressed in a basis of fiber modes. For short segments of fiber without sharp bends, the matrix is nearly diagonal [74].

The existence of modes with well-defined propagation constants can be related to the geometric picture of ray propagation in fibers. When light rays enter the fiber and reach the core-to-cladding interface, the law of reflection prohibits the momentum to change in a plane tangent to the interface. Therefore, in a straight fiber the axial momentum of the light (which corresponds to the propagation constant) is conserved [62]. The light always exits the fiber with the same longitudinal angle of propagation, but with a possibly randomized direction in the transverse plane. This corresponds to the experimental observation that a plane wave injected in a step-index multimode fiber at a certain angle tends to come out of the fiber as a hollow cone of light with the same aperture angle. So if the transmission matrix is expressed in a basis of plane waves, one expects the high-amplitude coefficients to be concentrated around the diagonal.

In graded-index fibers, there are large groups of degenerate modes which share the same propagation constant [100]. Significant coupling within these mode groups is observed even over a distance of a few meters. However, coupling between modes of different propagation

²This is equivalent to “phase conjugated” in the monochromatic regime.

constants is low. This gives the matrix a sparse and approximately block-diagonal structure in a basis of fiber modes ordered by propagation constants [99]. Due to the continuously varying refractive index profile inside graded index fibers, one cannot say anymore that the input angles will be conserved.

Polarization properties

A vectorial calculation of the propagation-invariant modes in a step-index fiber (see Appendix A) reveals that most modes are predominantly circularly polarized. And indeed, in transmission matrices of step-index fibers, the sub-matrices connecting both polarizations are almost zero if circularly polarized basis vectors are used [74]. This is true whether the basis consists of the actual fiber modes, or whether it consists of any other set of circularly polarized fields. On the contrary, the transmission matrix contains significant cross-coupling coefficients when linearly polarized basis vectors are used instead. Practically, this means that a circularly polarized input field tends to exit the fiber almost entirely with the same circular polarization.

The conservation of circular polarization is a good approximation in most cases. Of course, in bent fibers a certain amount of polarization cross-coupling is to be expected due to mode coupling. However, even in an ideal straight fiber, there is a small set of modes that cannot be approximated only with a single uniform circular polarization component. As the numerical aperture of a fiber grows, increasingly more modes exhibit a non-uniform polarization distribution. How well the circular polarization is maintained depends on the modal parameters of the input field, and the physical parameters and shape of the fiber.

Graded-index fibers seem to have more complicated polarization properties. Experimentally, they are found to preserve neither linear nor circular polarizations [98]. More in-depth modeling studies of light propagation in these fibers will be needed in order to fully elucidate their polarization behavior.

3.2 Experimental aspects

3.2.1 Fourier basis

The choice of the basis in which to represent the transmission matrix deserves some attention. The fiber modes themselves can serve as basis [74, 99, 111], as suggested also by Figure 3.1. However, any other basis can work as long as it can completely describe all fields coming in and out of the fiber³. Examples found in literature include localized spots [57, 65] or plane waves with varying angles [63, 72]. The input and output bases can be different from each other [63, 72]. The input basis can also be different from the input patterns actually used to measure the fiber [61, 74], in which case a linear transformation links the input-output

³In algebraic terms, the chosen basis should contain the modes of the fiber as a subspace.

Chapter 3. Transmission matrix

measurements to the matrix. In the present work, the matrix is always measured in a basis of plane waves, which is called here a “Fourier basis”. The reasons are explained in the following paragraphs.

Current modulators and cameras have active areas in the megapixel (1 000 000 pixels) range. On one hand, it is desirable to expand the fiber image to cover as many of those pixels as possible on the device (beyond even the minimum outlined in Table 2.1 on p. 26). Using more pixels reduces sampling artifacts, and some methods such as off-axis holography require extra resolution anyway for proper operation (see chapter 2). On the other hand, the full resolution is usually too high to fit all the pixels in a transmission matrix. Indeed, with optical fields of 1000 by 1000 pixels on both sides of the fiber, the matrix would require computation and storage of 1000^2 by 1000^2 elements, i.e. multiple terabytes of data, which is currently above a typical computer’s memory capacity.

One way around this problem is to build the matrix not with the field values at every pixel on each end of the fiber, but with a reduced set of Fourier coefficients describing these fields. As evidenced by the off-axis hologram in Figure 2.3(b) on p. 15, the fiber’s optical field is concentrated in a compact area in Fourier space. This is because the number of Fourier coefficients depends on the NA of the fiber and the size of the field of view around the core⁴, but not on the actual resolution used to sample this field of view. The conversion between the Fourier coefficients and the actual field values is efficiently carried out by a Fast Fourier Transform (FFT).

There are multiple advantages to using a Fourier basis. First, the full resolution of the modulator and camera can be used while keeping the size of the transmission matrix manageable. For example, for a fiber with a 105 μm core and a measured NA of 0.23 at 532 nm, approximately 7800 Fourier coefficients are needed to describe each side of the fiber in one polarization (while this fiber supports about 5100 modes per polarization at this wavelength). The result is that the matrix can be built with only 7800 by 7800 elements, i.e. a few hundred megabytes of data. The size of the matrix grows rapidly with NA and core diameter, though, as elaborated further in subsection 3.2.3.

Second, with a Fourier basis the natural choice of input patterns for measurement of the matrix is a set of plane waves with varying angles. Luckily, this is a type of pattern that phase-only modulators can display very accurately, since these are linear phase masks without amplitude component. In addition, each such phase mask covers the whole field of view on the SLM. This means that a maximum amount of light is injected into the fiber during each input-output measurement [61] in contrast to pixel-grouping schemes [57], where the small active zone of SLM can for example be overwhelmed by stray light scattered from the SLM chip. These factors improve the accuracy of the measurement.

⁴To have the minimum number of coefficients in Fourier space, the field of view should be limited to the core and not include too much margin around it. If the field of view is extended with a wider margin around the core, then the number of Fourier coefficients will increase unnecessarily due to the Fourier scaling property.

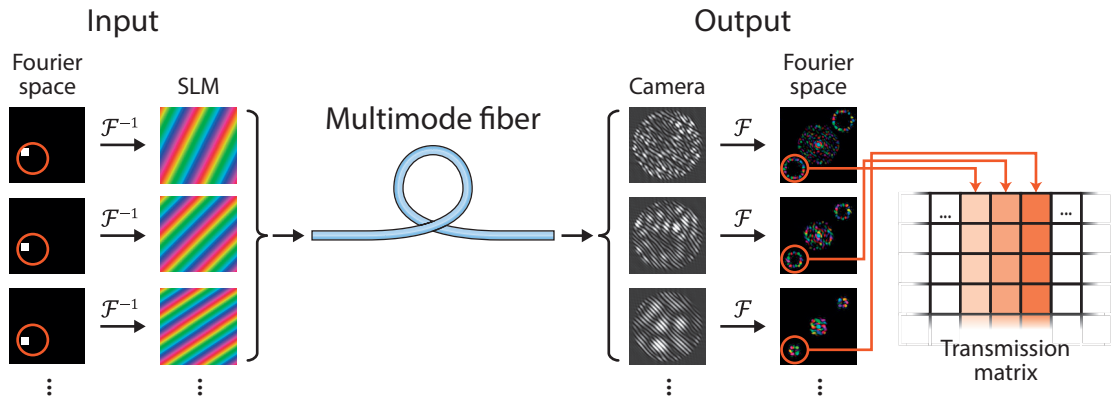


Figure 3.2: Fourier basis for the measurement of the transmission matrix.

The transmission matrix is thus measured by sequentially turning every “Fourier pixel” of the SLM on. In the spatial domain, the Fourier pixels correspond to phase gratings of varying period and orientation on the SLM. For each input grating, the corresponding Fourier coefficients of the output are recorded by the camera in an off-axis hologram. Each such Fourier input-output measurement fills one column of the transmission matrix. This is illustrated in Figure 3.2. Only Fourier components that are compatible in angle with the NA of the fiber are used as input or output. These areas are denoted with an orange circle in Figure 3.2. As an added bonus, the procedure skips the inverse Fourier transform required to reconstruct the output field from the off-axis hologram (see subsection 2.1.3 on p. 14), leading to a lower computational cost.

An important pitfall must be noted here. Off-axis holograms contain both a real and a conjugate order, as explained in subsection 2.1.2. Selecting the correct order, i.e. the real order, is crucial in transmission matrix experiments. If the conjugate order is selected, each input coefficient will be related with the conjugate of the output. This is not a linear relationship, and will cause problems e.g. when trying to invert the matrix for imaging (as will be needed later in chapter 4). In theory, one can figure out where the real order is in the Fourier domain based on the physical direction of the reference beam relative the object beam. A simpler alternative in wavefront shaping setups is to use the spatial modulator for this purpose: simply shift the phase of the input beam using the SLM (e.g. by $\pi/4$) and compare the Fourier domain of the off-axis hologram before and after the shift. The order that shifts with the same phase as the SLM is the real order, and the one that shifts with opposite phase is the conjugate order.

3.2.2 Phase drift tracking

One inconvenient aspect of interferometric measurements is that they are generally very sensitive to environmental perturbations such as temperature changes and vibrations. This is especially true for methods with separate reference and object beams, such as off-axis holography. Over time, the relative phase between the reference beam (plane wave) and the

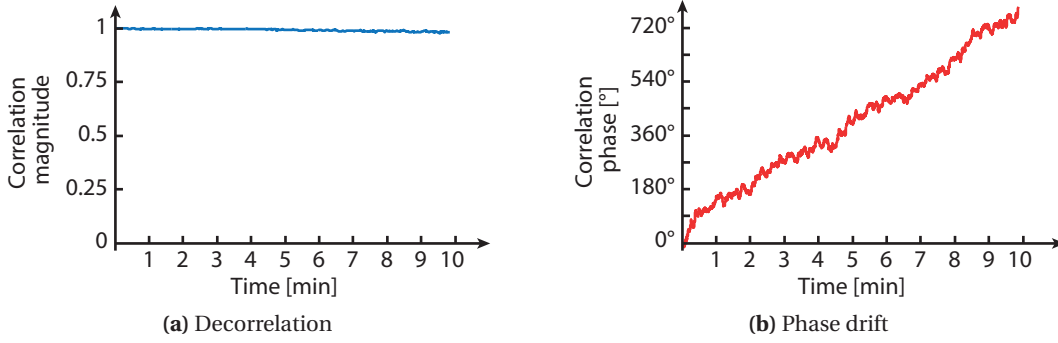


Figure 3.3: Temporal stability of the recorded reference field, as measured by the complex correlation coefficient.

object beam (output of the fiber) can drift. Unfortunately, all basis vectors must be measured with respect to the same phase reference; otherwise they cannot be used coherently with each other in the transmission matrix. Other perturbations such as mechanical instabilities can modify not only the phase but also the amplitude distribution of the output. This greatly affects the measurement, since the matrix method requires the system to be time-invariant. In literature, similar issues are discussed in connection with the process of recording physical hologram [157].

To quantify the effect of drifts and instabilities in the fiber measurement system, we introduce the complex correlation coefficient,

$$\rho_{\mathbb{C}} = \frac{\langle f, g \rangle}{\|f\| \|g\|} = \frac{\sum_{k=1}^N f_k g_k^*}{\sqrt{\sum_{k=1}^N |f_k|^2} \sqrt{\sum_{k=1}^N |g_k|^2}} \quad (3.3)$$

where f and g are vectors with N elements and g_k^* denotes the complex conjugate of g_k . The complex correlation coefficient is a straightforward extension of the linear correlation coefficient in statistics to complex numbers: its magnitude estimates the degree of linear similarity between two datasets, and its phase estimates the overall phase rotation [158]. Because of Plancherel's theorem, it has the same value whether it is calculated from the complex field values or from the Fourier coefficients.

Figure 3.3 shows the typical behavior of the correlation coefficient over a time period of 10 minutes in this system. A constant input field is fed to the fiber and the output field is monitored. At each point in time, the current output field is correlated with the first measured output field in the sequence. As evidenced by Figure 3.3(a), there is no decorrelation in this measurement since the magnitude of the correlation coefficient remains very close to 1. Figure 3.3(b) shows that the phase varies slowly over time, with an average rate of 72° per minute in this experiment.

The topic of interferometric stability is covered briefly in a number of textbooks [159–161]. The following destabilizing influences were identified in the course of this work:

- *Air flow*: Moving air is a problem in long-running interferometric measurements because of the associated temperature gradients. Air that is 1°C hotter or cooler has a difference of refractive index of the order of 10^{-6} (around an ambient temperature of 20°) C [162]. This is sufficient to cause a 2π phase shift over a distance of 50 cm at 532 nm. An effective way to block external sources of air flow is to build an enclosure around the experimental setup. Air flow cannot be entirely eliminated in experiments with an SLM, because the SLM itself generates a significant amount of heat which displaces the air.
- *Wavelength shifts*: Diode-pumped solid state (DPSS) lasers can be found with linewidths down to 1.5 MHz. It is rarely specified, however, that this laser line can drift over time over an interval that is much larger than the linewidth itself. If the wavelength shift is $\Delta\lambda$ and there is an optical path length difference ΔL between the reference and object arm, a corresponding phase shift $\Delta\phi = \frac{2\pi}{\lambda^2} \Delta L \Delta\lambda$ will be observed in the hologram. For this reason, it can sometimes be useful to equalize the path lengths of reference and object arms ($\Delta L = 0$) even when using lasers with long coherence lengths. An alternative is to use wavelength-stabilized laser sources.
- *Mechanical and thermal drift*: Most translation stages and adjusters drift slowly over time. Temperature changes can also modify the relative positioning of optical elements due to thermal expansion. It is best to limit the number of adjustable elements, avoid the use of very sensitive elements (e.g. pellicle beam splitters) and wait for the thermal equilibrium of the setup and all the devices to be reached before running experiments.
- *Vibrations*: Optical setups should be built on rigid, vibration-isolated tables in quiet rooms. With these precautions, vibrations should not affect measurements appreciably.

Realistically, not all perturbations can be prevented, so a correction mechanism should be used. Decorrelation (i.e. a decrease in $|\rho_C|$) cannot easily be fixed in post-processing, and should be limited as much as possible. Phase drifts (i.e. changes in the phase of ρ_C), however, can be estimated and corrected provided they are sufficiently regular in time.

In order to eliminate the phase drift in the transmission matrix measurements, a monitoring scheme was used. Instead of measuring the input-output response for every basis vector in a sequence, a constant reference input was inserted after one out of every 2 inputs. Each of the corresponding reference output measurement was then correlated with the first reference output measurement to estimate the relative phase drift. Then, the phase was interpolated (cubic spline interpolation) to estimate the phase drift in the time intervals between each of reference measurement. Finally, this estimation was used to correct the output measurements forming the matrix. This is shown in Figure 3.4. For longer measurements, a correction was also included for slight lateral movements of the fiber core within the field of view, due to the mechanical drift of translation stages. In recent literature, phase drift has been mitigated by similar phase correction schemes [92] or by using co-propagating reference fields [18].

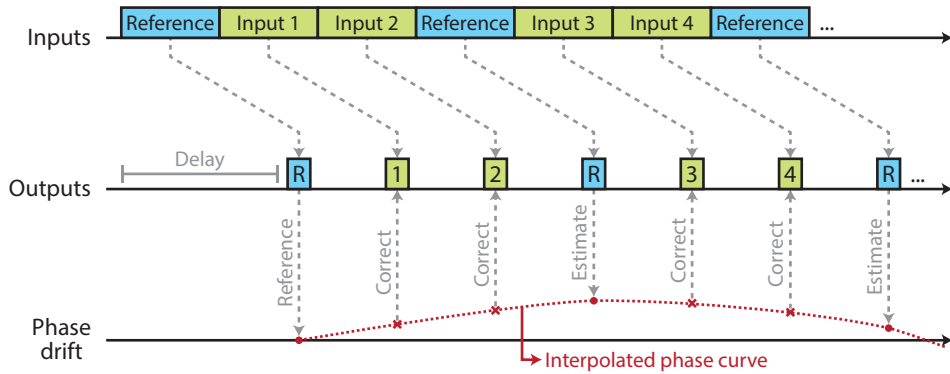


Figure 3.4: Timing diagram of the matrix measurement with correction for phase drift. Reference frames are interleaved with the input-output measurements. From these reference measurements, the overall phase drift is estimated at various points in time. The input-output measurements are then corrected by interpolation. For consistency, this timing diagram also includes the input-output delay and the limited acquisition window for the output, as explained in subsection 2.2.2 on p. 19.

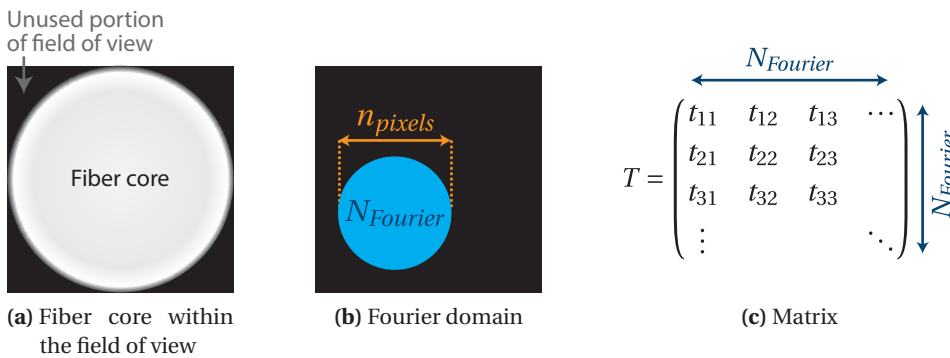


Figure 3.5: Size of the transmission matrix

3.2.3 Memory requirements

Transmission matrices connect every possible input of a system with every possible output. As the number of inputs and outputs increase, the number of combinations can quickly run out of hand. This section discusses how big of a matrix can be measured given the limited amount of computer memory available to store it. The calculations below apply specifically to the case of a Fourier basis measurement as described in subsection 3.2.1 on p. 33.

Let us assume that the fields of view of both SLM and camera are adjusted so that the fiber core just fills the image area as in Figure 3.5(a). Assume also that on each side only a minimal region of Fourier space is included in the matrix. Then, the lateral size of this region is given by n_{pixels} as calculated in Equation 2.8 on p. 26. This is independent of the physical pixel counts of the devices.

Now, n_{pixels} is the *diameter* of the Fourier region needed to describe the input or output. The actual number of coefficients within this region, $N_{Fourier}$, depends on the *area* of the region. This is drawn in Figure 3.5(b). Assuming a circular area of Fourier coefficients is cut out, then $N_{Fourier}$ is approximated by:

$$\begin{aligned}
 N_{Fourier} &= \pi r_{pixels}^2 \\
 &= \pi \left(\frac{n_{pixels}}{2} \right)^2 \\
 &= \frac{V^2}{\pi}
 \end{aligned} \tag{3.4}$$

Equation 3.4 might raise the eyebrows of readers who remember that the number of modes in step-index fiber [163, p. 705] is $N_{modes} = \frac{V^2}{2}$. The difference between both formulas is explained as follows. Here, $N_{Fourier}$ is the number of coefficients in a circular region of the Fourier domain. Even though we cut out a circular area in the Fourier domain, this limited set of coefficient still describes a rectangular field of view in the spatial domain. Yet, the fiber core is circular in the spatial domain. Hence, the set of $N_{Fourier}$ Fourier coefficients we selected here overdetermines the fiber's optical field by enclosing it within a rectangular field of view, as shown in Figure 3.5(a). The proportion of “useful” coefficients within $N_{Fourier}$ is given by the ratio between the area of the round fiber core and the area of the square field of view around it. This is precisely $\frac{\pi}{4}$. An additional factor 2 comes from the fact that N_{modes} counts the modes in both polarizations, whereas for $N_{Fourier}$ in Equation 3.4 we consider only one polarization.

$N_{Fourier}$ gives the minimal number of coefficients needed to describe either the input or the output (assuming the procedure from subsection 3.2.1 is used). The matrix connects every input coefficient with every output coefficient, and contains therefore $N_{Fourier}^2$ elements as illustrated in Figure 3.5(b). The size of the matrix is therefore:

$$\begin{aligned}
 N_{matrix} &= N_{Fourier}^2 \\
 &= \left(\frac{V^2}{\pi} \right)^2 \\
 &= \pi^2 \left(\frac{d NA}{\lambda_0} \right)^4
 \end{aligned} \tag{3.5}$$

With Equation 3.5, the problem of scaling becomes apparent. Doubling either the field of view or the resolution of the fiber results in a 16-fold growth of the matrix size. Note also that N_{matrix} is the minimum size for one polarization; including both polarization increases this number by an extra factor of 4.

Practically, a matrix of a fiber of core diameter 105 μm and NA 0.22 at 532 nm uses at least 535 Mb of computer memory, for a single polarization and assuming complex numbers stored as pairs of 64-bit floating point values. A fiber of core diameter 200 μm and NA 0.39 at 488 nm takes minimum 96 Gb.

Scaling the method to fibers of any size would require escaping the fourth-power law of Equation 3.5. This would be possible by exploiting the sparsity of the matrix as discussed in subsection 3.1.2 and in references [74, 113]. By storing only the matrix coefficients describing significant coupling between modes, the number of matrix elements would be drastically reduced. This requires using a fiber mode basis for the matrix, though, so an efficient and scalable algorithm is necessary to transform experimental data to a fiber mode basis. The problem of aligning the fiber mode basis to the experimental data is also non-trivial [74, 98].

In this work, only full matrices in a Fourier basis are used. Despite the memory limitations, the algorithm is very fast and can process holograms in real-time even for relatively large fibers. In addition, the procedure requires only minimal tuning when the fiber parameters (core size, NA, index profile,...) are changed.

3.3 Measurement

The experimental setup for the measurement of the transmission matrix in this section is shown in Figure 3.6. Light from a 532nm diode-pumped solid state continuous wave laser (CNI MSL-FN-532-100mW) passes successively through a variable attenuator (VA), a half-wave plate ($\lambda/2$), a beam expander (lenses L1 and L2), and a spatial filter (objective OBJ1 and pinhole P), after which it is collimated by a lens (L3). Then, a polarizing beamsplitter splits the light towards each side of a multimode fiber. The half-wave plate and the polarizing beamsplitter allow adjusting the amount of light sent to each arm. A second half-wave plate ensures that the polarization is the same in both arms. The multimode fiber (Thorlabs M43L01, $\text{\O}105\ \mu\text{m}$ core, NA 0.22, FC-APC connectors) is taped in place on the optical table and a few posts. It is 1 m long and has in this experiment a single bend with an approximate radius of curvature of 10 cm. On one side of the fiber, there is a phase-only spatial light modulator (HoloEye Pluto) that reflects part of the incoming light via a beamsplitter towards the multimode fiber. It can be used to send controlled input patterns to the multimode fiber. On the other side of the fiber, a camera (PhotonFocus MV1-D1312(IE)-G2-100) records the light fields coming out of the fiber through a magnifying system (L4/L5 and OBJ2/OBJ3) and a beamsplitter. The collimated beam coming through the other port of the beamsplitter is tilted slightly in angle (1.5°), to serve as a reference for off-axis holography. Note that only a single polarization was measured (linear). In Figure 3.6, the term “proximal side” refers to the experimenter’s side of the fiber (with the spatial light modulator). The other side is called the “distal side”; when imaging (in chapter 4), this is the side of the fiber that is brought close to the target location.

As explained in the previous sections, the matrix was measured in a Fourier basis. The matrix described in this section contains 7213 by 7845 coefficients and took approximately 10 min. to measure. The amplitude of the matrix coefficients in function of the input and output angles they connect is represented in Figure 3.7. The distribution of the energy among the matrix coefficients shows the conservation of momentum: light injected with a particular angle tends to come out of the fiber at the same angle, even in this bent fiber.

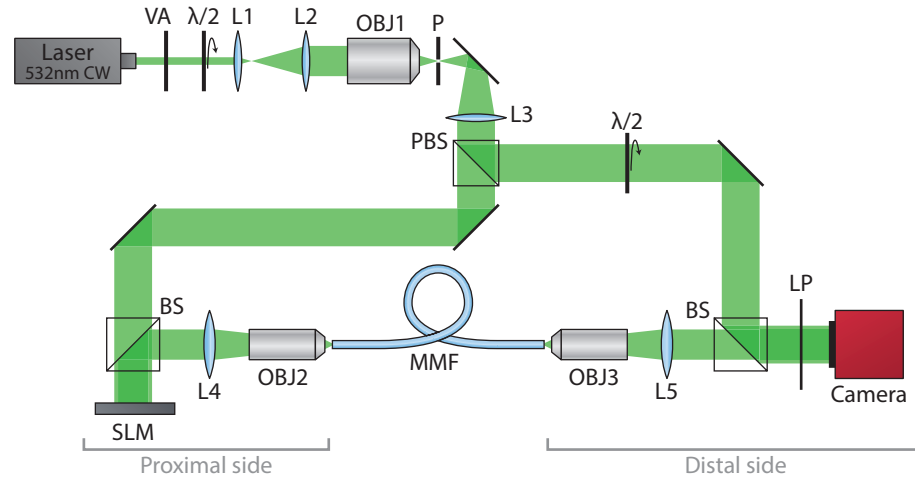


Figure 3.6: Experimental setup for the transmission matrix measurement.

VA: variable attenuator; $\lambda/2$: half-wave plate; L1: $f = 30$ mm lens; L2: $f = 75$ mm lens; L3: $f = 200$ mm lens; OBJ1: infinity corrected 10x microscope objective; P: $10 \mu\text{m}$ pinhole; L3: $f = 200$ mm lens; PBS: polarizing beamsplitter; BS: beamsplitter; LP: Linear polarized; SLM: spatial light modulator; L4, L5: $f = 250$ mm lens; OBJ2, OBJ3: 40x microscope objective; MMF: multimode fiber with $\text{Ø}105 \mu\text{m}$ core and NA 0.22.

Another general property of the matrix can be readily verified. In the product matrix TT' (shown in Figure 3.7), all the high-amplitude coefficients are concentrated on the diagonal and they have a fairly uniform amplitude, approximating the identity matrix. This illustrates that the measured transmission matrix is close to unitary. Perfect correspondence is difficult to obtain experimentally as explained in subsection 3.1.2.

A set of transmission maps can be calculated from the matrix. These maps describe for each point on the facet of the fiber how much light will be transmitted there on average in comparison to the other points. This is shown in Figure 3.9(a) and (c) for the input and output respectively. The same can be done in the Fourier domain for angles (i.e. how much light will be transmitted for any given angle), as shown in Figure 3.9(b) and (d). Note that there is more attenuation for off-axis propagation angles. This effect is also seen with straight fibers in other reports in literature (e.g. in the supplementary information of [74]), but may have been exacerbated here due to bend losses or limitations in the optics. The sharp edges of the Fourier maps are due here to the artificial limitation of the angles that are scanned and recorded during the measurement of the matrix (see subsection 3.2.1).

The singular values of the matrix were calculated and drawn in Figure 3.10. The singular value decomposition gives a representation of the rank of a matrix, i.e. the number of independent components it contains. This in turn gives an indication of the number of modes in the fiber under study. Next to the experimental singular values found for this fiber in this particular configuration, a simulated curve is also shown in Figure 3.10. The simulation is based on

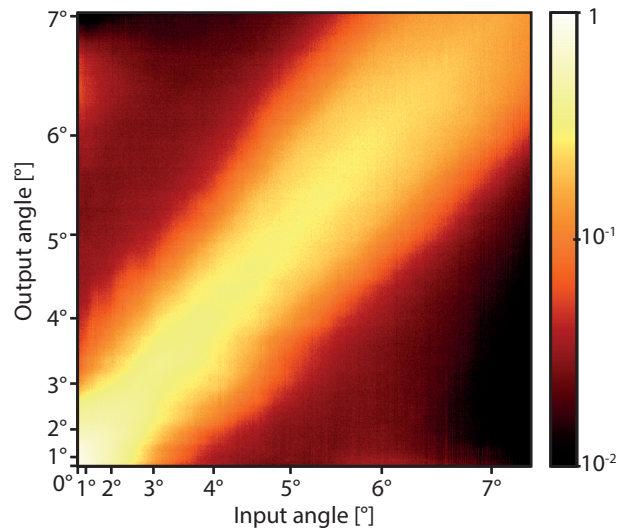


Figure 3.7: Amplitude of the measured transmission matrix coefficients. This illustration is a scaled down version of the full matrix where coefficients with equal input and output angles have been grouped together and averaged (RMS value).

the mode propagation model of optical fibers (see Appendix A), and creates a “synthetic” transmission matrix by virtually replicating the Fourier basis measurement procedure outlined in subsection 3.2.1. The nominal fiber specifications were used ($\text{\O}105\ \mu\text{m}$ core, NA 0.22). The simulation takes into account that only a single linear polarization is measured, but assumes a straight fiber. The comparison between the simulated and experimental curve reveals that there are slightly more modes than expected in this fiber. In theory, this fiber should support approximately 4 500 modes per polarization, whereas over 5 000 are found experimentally. Partly, this is due to the manufacturing tolerances on the fiber parameters (core of $105\ \mu\text{m} \pm 2\%$, NA of 0.22 ± 0.02). With parameters estimated from the transmission maps in Figure 3.9, there should be approximately 4 800 modes. The remaining difference may be due to residual cladding modes that are insufficiently suppressed in this relatively short length of fiber. Finally, the beginning of the experimental curve also shows a lower overall magnitude of the singular values compared to the simulation. This can be explained by the bending of the fiber (and associated losses) which is not taken into account in the simulation.

3.4 Conclusion

The transmission matrix method presented in this chapter allows relating the input and the output of the fiber via a simple algebraic formula. It is measured here in a Fourier basis which allows exploiting the full resolution of the modulator and camera while keeping the number of coefficients down. Phase drift is tracked and corrected during the measurement. A number of general properties of transmission matrices of fibers were verified experimentally, such as conservation of momentum, unitarity and the number of independent modes.

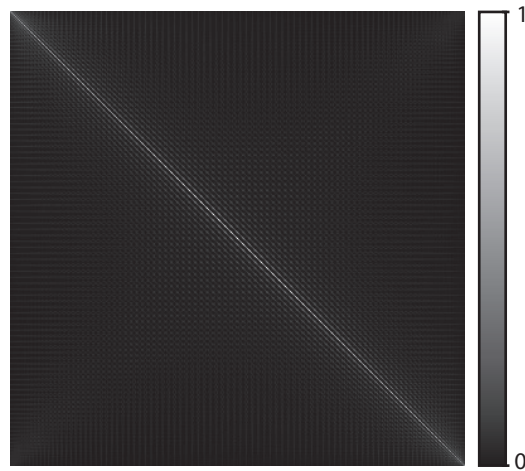


Figure 3.8: Amplitude of the product TT' . This illustration is a scaled down version of the full matrix TT' (20:1 reduction with box averaging), in order to make the diagonal visible at this scale.

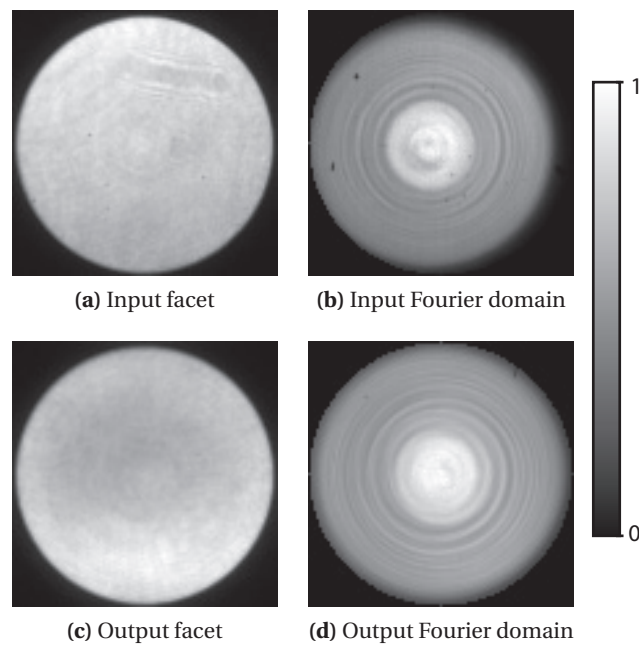


Figure 3.9: Intensity transmission maps derived from the matrix.

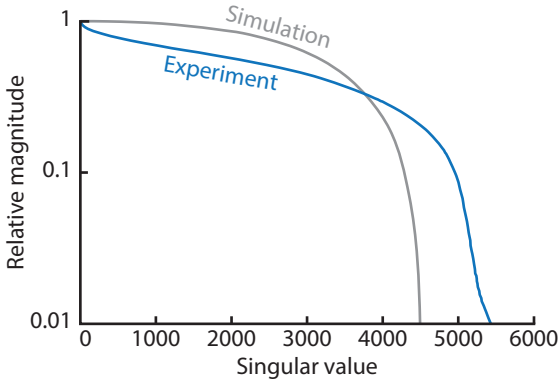


Figure 3.10: Singular value decomposition of the transmission matrix (considering only a single linear polarization).

4 Image transmission

In this chapter, the transmission matrix is used to project and reconstruct images through multimode fibers. Results are presented for image transmission from the proximal end to the distal end, and in the reverse direction.

Some of the material presented in this chapter can be found in the following papers:

- Damien Loterie, Salma Farahi, Demetri Psaltis, and Christophe Moser. Complex pattern projection through a multimode fiber. In *Adaptive Optics and Wavefront Control for Biological Systems*, volume 9335, pages 93350I–1 to –6, 2015.
- Damien Loterie, Salma Farahi, Ioannis Papadopoulos, Alexandre Goy, Demetri Psaltis, and Christophe Moser. Digital confocal microscopy through a multimode fiber. *Optics Express*, 23(18):23845–23858, September 2015.

4.1 Pattern projection

In pattern projection experiments, the goal is to obtain a chosen pattern at the distal end of the fiber by feeding the correct input wavefront into the proximal tip of the fiber. Sending controlled patterns through a fiber can be useful for structured illumination or compressed sensing, or simply to do scanning microscopy using spots.

4.1.1 Inversion of the matrix

To calculate the required input wavefront, the first step is to invert the transmission matrix. The algebraic inverse T^{-1} cannot be used due to measurement noise and rank-deficiencies. Two different stable methods were investigated instead.

In *phase conjugation*, the Hermitian transpose of the matrix is used as its inverse: $T_{inv} = T^\dagger$. As discussed in subsection 3.1.2 on p. 31, this would be a perfect inverse were it not for losses and other experimental limitations. Using T^\dagger is equivalent to performing optical phase

conjugation [18]. This inversion method requires very little computations.

With *Tikhonov inversion*, the inverse is calculated as $T_{inv} = (T^\dagger T + \lambda I)^{-1} T^\dagger$. It can alternatively be calculated via spectral filtering: $T_{inv} = V \Sigma^+ U^\dagger$, where $T = U \Sigma V^\dagger$ is the singular value decomposition of T , and Σ^+ is a diagonal matrix containing the singular values σ_i of T filtered by the function $f(\sigma_i) = \frac{\sigma_i}{\sigma_i^2 + \lambda^2}$. Via the regularization parameter λ , this inversion method strikes a balance between algebraic inversion and phase conjugation [20]. In general, this achieves lower reconstruction errors than phase conjugation alone.

4.1.2 Results

Intensity patterns

Both inversion methods can be compared with the experimental results presented in Figure 4.1 using the setup of Figure 3.6 on p. 41. With each inverse matrix, the input pattern was calculated to obtain a chosen pattern at the output of a multimode fiber. For Tikhonov inversion, the regularization parameter λ was 10% of the largest singular value σ_1 of the transmission matrix. This value was found empirically to optimize the contrast of the patterns. The inputs were optimized using the Gerchberg-Saxton amplitude coding algorithm (subsection 2.2.4) before being displayed on the SLM. The resulting output pattern was then recorded on the camera (without a reference beam, i.e. non-holographically). For this set of measurements, a polarizing filter was placed in front of the camera to suppress the uncontrolled polarization (as shown in Figure 3.6).

For a correct interpretation of the experimental results, I state here how the camera images were processed in Figure 4.1. In each image, the fixed pattern noise of the camera was compensated by subtracting a background image taken with the same exposure time but without laser light. The experimental data was then scaled to fit within the range of representable colors with minimal clipping (less than 0.1% of out-of-range pixels). The black level was however not modified (apart from the background subtraction). No spatial averaging or image size reduction was used. The camera's data is linear, i.e. without gamma modification.

It is not straightforward to choose a “general” quantitative error metric for the output patterns that would be meaningful for any application. In Figure 4.1, the linear correlation coefficients is stated for each measurement to give an indication of the linear similarity with the target pattern. It ranges here between 58.1% for a grating pattern calculated with phase conjugation and 99.3% for a line pattern calculated with Tikhonov inversion.

The subjective visual quality of the patterns depends mostly on the contrast between the pattern and the background noise. In this experiment, the signal-to-background ratio depends on how much the light is concentrated inside the pattern. For a pattern with a small area such as the line in Figure 4.1, the signal-to-background is over 1000:1, whereas for the letter “A” it is approximately 24:1 (Tikhonov inversion).

By applying the appropriate propagation factors, patterns can be projected at any distance in front of the fiber. This is demonstrated in Figure 4.2 for projection in the far field. Note that the vertically mounted experimental setup shown in Figure 4.2 is different from the setup used for Figure 4.1 (which was horizontally mounted and corresponds to Figure 3.6). The vertical setup was mounted in collaboration with my colleague Paul Delrot.

Focused spots

Many microscopic imaging mechanisms are possible once a spot can be scanned over a target location at the distal end of a fiber. Examples include fluorescence [60–62, 64, 65, 69, 164], two-photon fluorescence [70–72], reflection [73, 74] and photoacoustic [66, 81, 114] microscopy.

The advantage of using a transmission matrix for this purpose is that the imaging plane can be dynamically changed without requiring any physical adjustment of the system. Images can be made at variable distances in front of the fiber, within the constraints imposed by the aperture of the fiber [60]. The image plane can also be freely re-oriented to make transversal cuts through the sample (e.g. for confocal microscopy as in chapter 5).

As with the intensity patterns, the correct measure of performance for spots will depend on the particular application. The most common measure in the multimode fiber imaging literature is the “enhancement” [55, 58, 59, 65, 71, 86, 90], a contrast metric borrowed from the scattering media literature [15]. It can be calculated as the ratio between the peak intensity of the spot and the average intensity of the whole beam (including the background noise). The relevance of this figure of merit in microscopy can be debated, because the enhancement does not account for the area over which the background noise is spread out. If spots A and B have the same enhancement, but the area of the noise in A is twice as large as in B, then A will create twice as much spurious signals as B during spot-scanning microscopy.

To account for the overall noise level, an additional metric is used in this section: the ratio between the power in the central lobe of the spot versus the total power of the beam. This number conveniently describes what fraction of the light will convert to useful signal during spot-scanning microscopy. For an ideal Airy spot, the maximum percentage of power in the central lobe is approximately 84%.

The experimental results of spot focusing are presented in Figure 4.3 using both metrics and three different fibers: 200 μm core and NA 0.39 (Thorlabs FT200EMT), 105 μm core and NA 0.22 (Thorlabs FG105LGA), and 50 μm core and NA 0.22 (Thorlabs FG050LGA). The fiber length was 7.5 cm for the 200 μm core fiber and 25 cm for the two other fibers. The spots were displayed using Gerchberg-Saxton amplitude coding (see subsection 2.2.4). The matrix was measured here in a circularly polarized basis using quarter-wave plates on each end of the setup [74]. Unlike the patterns of Figure 4.1, this set of measurements is done without a polarizer in front of the camera. The displayed image therefore corresponds to the total of the light transmitted through the fiber (i.e. both the measured circular polarization and the “uncontrolled” opposite

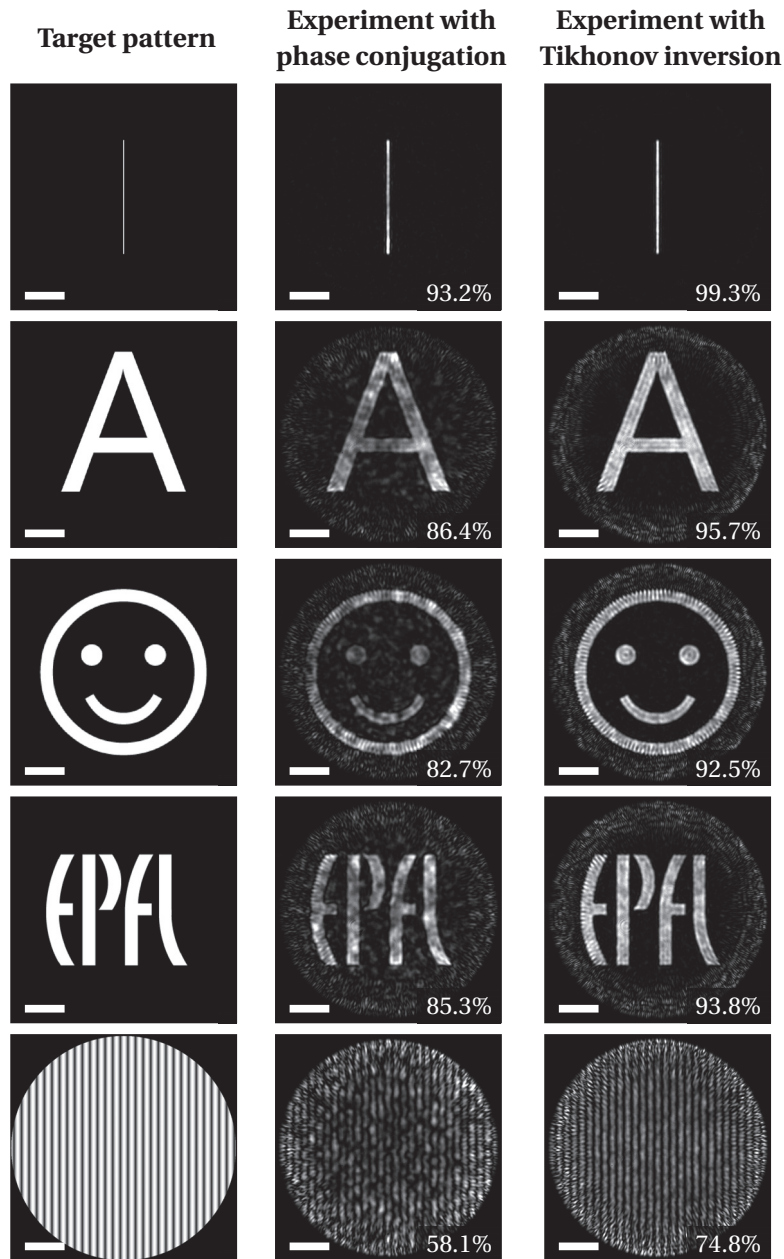


Figure 4.1: Projection of patterns at the distal side of the fiber. Fiber: Thorlabs M43L01, $\text{\O}105\ \mu\text{m}$ core, NA 0.22, 1 m length, FC-APC connectors. Wavelength: 532 nm. Scale bars: $20\ \mu\text{m}$. Bottom right corner: correlation coefficient versus the target pattern. The setup used here is the same as for the measurement of the matrix in Figure 3.6 on p. 41. Note the use of a polarizing filter to suppress one of the two polarizations.

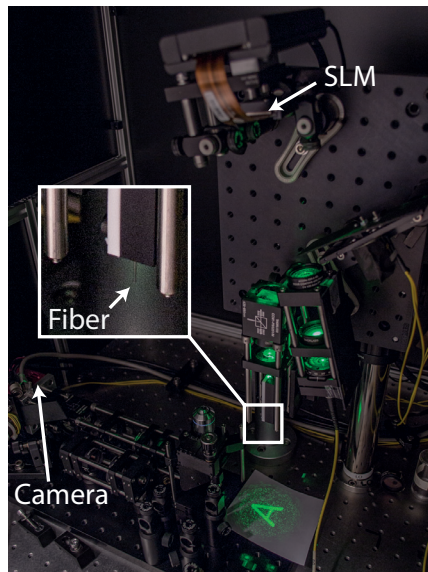


Figure 4.2: Photograph of pattern projection in the far field. This is a vertically mounted setup with a fiber (Thorlabs M43L01, $\text{\O}105\ \mu\text{m}$ core, NA 0.22, 7.5 cm length) immobilized inside a needle.

polarization). For each image, multiple camera exposures were combined in order to increase the dynamic range, which is necessary to detect the background noise properly [55, 57]. The matrix of the largest fiber, i.e. with the $200\ \mu\text{m}$ core and NA 0.39 in Figure 4.3(a), was measured at 488 nm and inverted by phase conjugation (due to the large number of modes). The other two were measured at 532 nm and inverted with the Tikhonov formula.

The enhancement is very high for a fiber with many modes such as the $200\ \mu\text{m}$ core, NA 0.39 fiber in Figure 4.3(a). However, the experimental apparatus concentrates approximately the same fraction of energy (around 50%) inside the spot when a much smaller fiber is used, i.e. the $50\ \mu\text{m}$ core, NA 0.22 fiber in Figure 4.3(c). The enhancement values differ by a factor of 40. In Figure 4.3(d-f) the line profiles of the spots in the corresponding images Figure 4.3(a-c) are given. The resolution is quantified with both the full width at half maximum, and the distance between the zeros around the main lobe. This resolution is close to the diffraction limit: the size of the main lobe is $0.81\ \mu\text{m}$ for NA 0.39 at 488 nm (diffraction limit: $0.74\ \mu\text{m}$) and $1.6\ \mu\text{m}$ for NA 0.22 at 532 nm (diffraction limit: $1.5\ \mu\text{m}$).

Special beams

Certain special types of beams find applications in advanced microscopy techniques, such as “donut” beams or bottle beams [165] in optical trapping [166, 167] and stimulated emission depletion (STED) microscopy [168]. Without going into further details, Figure 4.4 shows that these exotic beam shapes can be produced via fibers also, simply by loading the appropriate phase mask on the SLM.

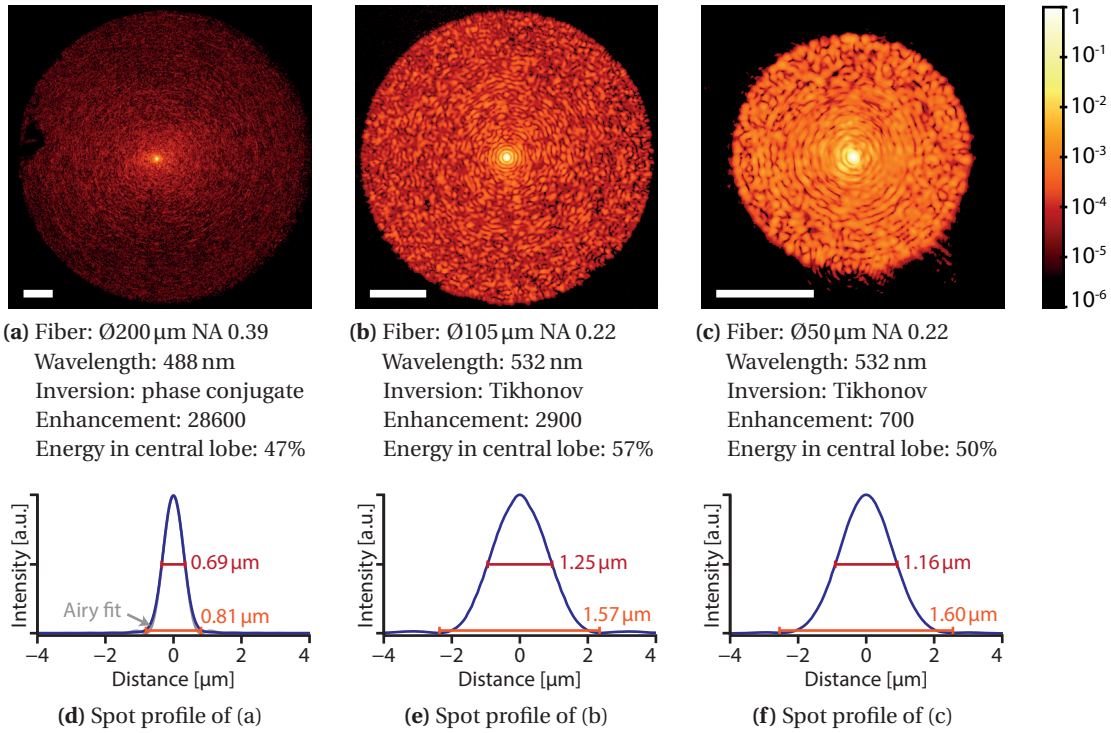


Figure 4.3: Focused spots created through a variety of fibers. (a)-(c) Logarithmic intensity images, with the value 1 representing the peak intensity of the spot. The scale bars represent $20\ \mu\text{m}$. (d)-(f) Line profiles of the spots, with full width at half maximum (in red) and distance between the zeros around the main lobe (in orange). In (d), the zeros were estimated from a fit to an Airy profile.

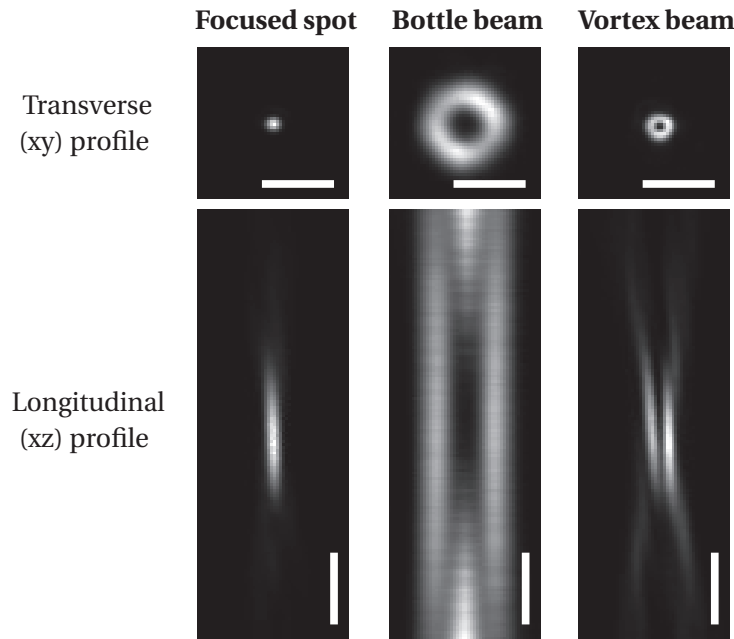


Figure 4.4: Bottle and vortex beam created through a fiber, with a focused spot for comparison. Fiber: $\text{\O}200\ \mu\text{m}$ NA 0.39. Wavelength: 488 nm. Inversion by phase conjugation. Scale bars: $5\ \mu\text{m}$. Linear intensity coloring.

4.2 Scanning microscopy

By sweeping focused spots over a sample area and collecting the signal returning back through the fiber, microscopic images can be reconstructed through a multimode fiber [60–62, 64–66, 69, 74]. This section shows briefly the application of the transmission matrix for two-photon fluorescence microscopy. Chapter 5 discusses in more detail the case of confocal reflection microscopy.

Unlike the other experiments presented in this thesis, I did not build the setup for the two-photon experiment or prepare the samples myself. Credit for this goes to my colleagues Donald Conkey, Nicolino Stasio, Edgar Morales Delgado, Jacob Staley and Marilisa Romito. My personal contribution here is to implement the transmission matrix algorithm on their setup as an alternative to digital phase conjugation. This setup is almost the same as the one of reference [155]. Our lab’s work on two-photon microscopy in multimode fibers is also further described in references [70, 71, 104]. For these reasons, the discussion here is kept brief.

A simplified diagram of the experimental setup is shown in Figure 4.5. There are several important differences with the setups described before. First, this setup uses a broadband femtosecond pulsed laser (Coherent Chameleon, 140 fs, operated at $\lambda = 785\ \text{nm}$). A delay line matches the path lengths of the object and reference beam, as is necessary for holographic recordings with the camera. Second, a photo-multiplier tube behind a dichroic mirror records the two-photon fluorescence signal collected by the fiber. Third, the fiber here is a multi-core

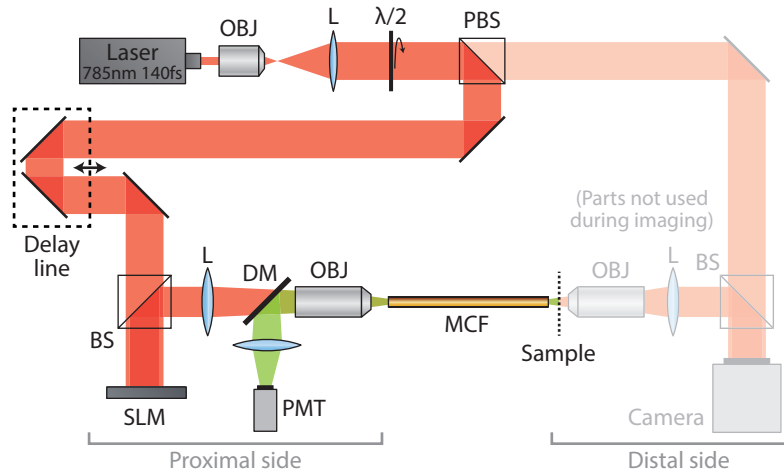


Figure 4.5: Simplified diagram of the two-photon fluorescence imaging setup.

The components in faded colors are needed during the measurement of the matrix, but not during imaging. OBJ: objective, L: lens, $\lambda/2$: half-wave plate, PBS: polarizing beam splitter, BS: beam splitter, SLM: spatial light modulator, PMT: photomultiplier tube, MCF: multi-core fiber.

fiber (Fujikura, FIGH-03-215S) instead of a step-index multimode fiber. This is because the dispersion properties of step-index fibers do not allow correcting modal scrambling over a broad range of wavelengths (as required for ultrashort pulses) for reasonable lengths of fiber. Graded-index fibers do provide enough bandwidth, but have a lower power threshold due to the self-focusing effect of light inside them. Because a multi-core fiber was used, the end facets of the fiber were placed out-of-focus. This effectively mixes the contributions from the different cores in the focal plane and spreads the energy more evenly on the active areas of the camera and SLM. The distance between the distal facet and the sample plane was 300 μm .

This setup was used to image the cochlea of a mouse *ex-vivo*. M. Romito prepared the cochlea samples. The cochleas were extracted from young mice (strain NMRI), and stained with Phalloidin 488 which binds to the protein F-actin. The fluorophore was Alexa Fluor 488, which has a sufficient two-photon cross section at the operating wavelength and emits in the green around 525 nm. All animal procedures were approved by EPFL.

The resulting two-photon images in Figure 4.6 show the structure of the cochlea and the hair cells. A depth section through a row of cells (indicated with a blue line) shows the sectioning effect obtained with by two-photon imaging. A measurement with a commercial two-photon microscope determined that the cochlear layer is approximately 16 μm thick.

In general, the advantages of the transmission matrix (with phase drift correction) are a dynamically adaptable scan plane and less stringent alignment requirements [155]. On the other hand, the main advantage of the digital phase conjugation approach is that only a fraction of the data of a full transmission matrix must be recorded if spots are needed only over a small field of view compared to the fiber.

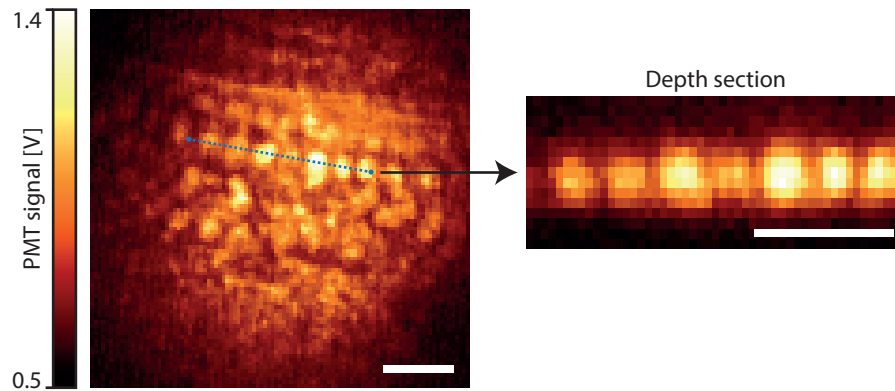


Figure 4.6: Two-photon fluorescence image of a mouse cochlea. The image on the left is a transverse (xy) scan of the cellular layer. The image on the right is a depth-section (xz) through the layer. The area of the depth section is indicated with the blue dotted line. Scale bars: $20\mu\text{m}$.

4.3 Reverse image transmission

The transpose of the transmission matrix describes light propagation in the reverse direction through the same system (see subsection 3.1.2 on p. 31). This recovering images traveling from the distal end to the proximal end of a fiber, i.e. the opposite direction of the pattern projection experiments in section 4.1. Incidentally, the inverse of the “backwards” matrix is also just the transpose of the inverse of the “forward” matrix, so that no new inversion is necessary.

4.3.1 Setup

The experimental setup is shown in Figure 4.7. It is the same setup as introduced for the matrix measurement in Figure 3.6 on p. 41, with two changes. First, an additional camera (also a PhotonFocus MV1-D1312(IE)-G2-100) is present at the proximal end of the fiber. It allows recording the fields coming from the distal to the proximal end. Second, a sample is placed in front of the distal fiber facet (between OBJ3 and the MMF). A variable aperture controls the field of illumination. The sample is illuminated from behind (in transmission) and the resulting light distribution is collected by the fiber.

Note that with the present acquisition system, the object beam coming from the distal end must be coherent with the reference beam in the proximal end. Otherwise, a holographic recording of the amplitude and the phase is not possible. This constraint could however be lifted by implementing a reference-free method of holography [169, 170].

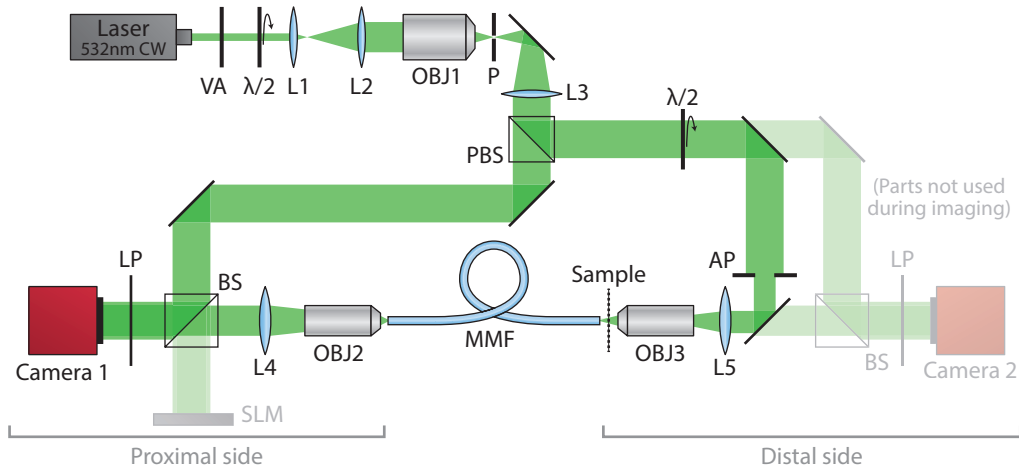


Figure 4.7: Setup for reverse image transmission.

The components in faded colors are needed during the measurement of the matrix, but not for reverse image transmission. VA: variable attenuator; $\lambda/2$: half-wave plate; L1: $f = 30$ mm lens; L2: $f = 75$ mm lens; L3: $f = 200$ mm lens; OBJ1: infinity corrected 10x microscope objective; P: $10\ \mu\text{m}$ pinhole; PBS: polarizing beamsplitter; BS: beamsplitter; LP: Linear polarized; SLM: spatial light modulator; L4, L5: $f = 250$ mm lens; OBJ2, OBJ3: 40x microscope objective; MMF: multimode fiber with $\text{Ø}105\ \mu\text{m}$ core and NA 0.22.

4.3.2 Alignment of camera and SLM

As discussed in subsection 3.1.2 on p. 31, applying the reciprocity property for reverse imaging poses a significant practical challenge. The transmission matrix is measured using the SLM, but the field must be recorded separately with a camera. For an accurate reconstruction, the camera must record the field exactly as it exists at the position of the SLM.

This is possible by placing the SLM and the camera in equivalent planes behind a beam splitter, as in phase conjugation experiments [59]. The two devices must then be aligned very precisely in position and in angle, and should ideally have the same pixel pitch (otherwise scaling is necessary). To reach the required precision quickly and easily, I used a digital registration approach. A known sample was placed in the distal end, and the object field was recorded on the proximal camera. This field was then interpolated, displaced, and tilted until it could be reconstructed properly with the transmission matrix. At this point, the camera matches the coordinate system of the SLM. The alignment parameters can be tuned only once and stay stable until either component is moved. Similar strategies can be found in literature for the alignment of digital phase conjugation mirrors [16, 171].

4.3.3 Results

Two different patterns were projected on the fiber's output facet. The samples were illuminated from the back using a collimated beam. On the proximal side, camera 1 (see Figure 4.7)

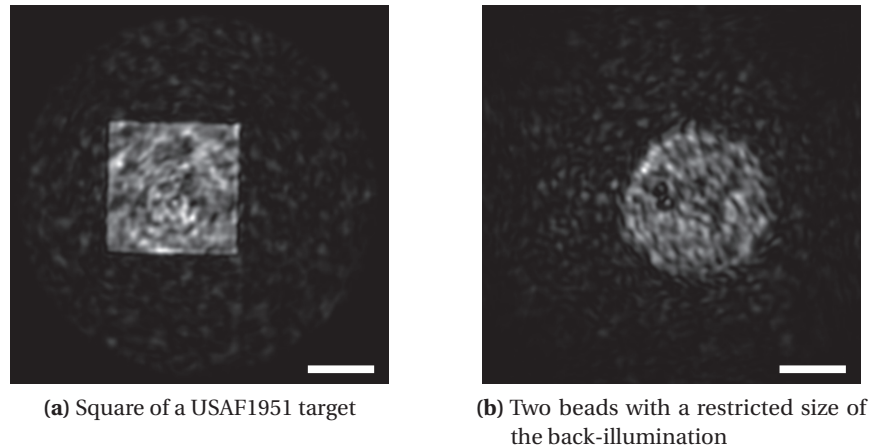


Figure 4.8: Results for reverse image transmission. Scale bars: 20 μm .

recorded the transmitted field with off-axis holography. The proximal Fourier coefficients were then decoded with the transposed inverse transmission matrix to reconstruct the distal output field. The reconstructed intensity images (calculated as the square of the reconstructed amplitude) are shown in Figure 4.8. The first pattern is a square from a Thorlabs USAF1951 resolution target, and has a signal-to-background ratio of 17:1. The second pattern consists of two beads on a microscope cover glass, illuminated from behind by a disk-shaped beam. The disk has a signal-to-background ratio of 10:1 with the surrounding speckle.

The quality of the reconstruction is visibly lower in this set of measurements than for pattern projection (section 4.1). This is most likely due to the imperfect matching of the camera and the SLM. While the alignment differences were compensated here, a more thorough matching algorithm that captures aberrations and other defects would achieve better results.

The results presented here beg the question whether it is possible to illuminate a sample through a fiber, and simultaneously view the light reflected from this sample via the same fiber (i.e. wide field reflection microscopy). This is indeed possible, but in that case the large amount of stray reflections in the proximal optics causes additional degradation of the image. Practically, this limits the field of illumination over which acceptable signal quality can be obtained. The maximum SNR is obtained with a spot-wise illumination, and this is applied in the next chapter for confocal filtering. High quality wide-field reflection microscopy with a single holographic acquisition could probably be achieved by suppression of reflections (e.g. through coatings or coherence gating), comprehensive matching of SLM and camera, and processing of both polarizations of the light in the fiber (which would increase the SNR).

4.4 Conclusion

As shown in this chapter, images can be transmitted through multimode fibers by inverting the transmission matrix. This allows high-quality patterns to be projected from the proximal end to the distal end. By creating intense focus spots at the distal facet of the fiber, a sample can be probed by spot-scanning microscopy. Here, this was demonstrated with two-photon microscopy through a multi-core fiber. Finally, thanks to the reciprocity property, the same matrix can be used for imaging in the reverse direction to recover patterns propagating back from the distal end to proximal end.

5 Digital confocal imaging

In this chapter, the imaging capabilities of multimode fibers are put to use to implement confocal imaging.

This chapter corresponds to the following publication, with minor adaptations: Damien Loterie, Salma Farahi, Ioannis Papadopoulos, Alexandre Goy, Demetri Psaltis, and Christophe Moser. Digital confocal microscopy through a multimode fiber. *Optics Express*, 23(18):23845–23858, September 2015.

5.1 Introduction

5.1.1 Fiber-based confocal endoscopes

Confocal microscopy is an important tool in biological imaging, because it substantially improves the contrast of images compared to wide field microscopy, and it allows depth-sectioning [172, 173]. In essence, the confocal microscope is based on a double filtering operation: a certain volume inside the sample is selectively illuminated by a focused beam, and light originating from this focal volume is selectively observed using a pinhole in the detection pathway. The pinhole is located in a plane conjugated with the focal plane, and suppresses light originating from any location other than the focal volume. With this method, a point of a sample can be probed with higher contrast with respect to its surroundings. Images are built by scanning the probed focal volume inside the sample.

In typical biological media, confocal microscopy allows us to obtain clear, background-free images only up to a certain point. Indeed, when focusing at a depth larger than the scattering mean free path, photons on the illumination path are scattered away before they can reach the focal volume. On the detection side, they are diverted from the detection path and blocked by the pinhole. The resulting loss in sensitivity ultimately limits the confocal imaging depth to the superficial layers of the tissue.

To image biological structures that are located deep in tissue, fiber-based endoscopes can

provide a minimally invasive solution. The existing confocal fiber endoscopes can be divided into two categories: fiber bundle systems and distal scanning systems [9, 174].

In fiber bundle systems, a coherent fiber bundle relays the spots created by a conventional confocal microscope to the distal facet of the bundle. The plane of imaging is either the distal facet of the bundle itself (the sample must then be placed in contact with this surface), or an extra lens (e.g. a GRIN rod lens) can be attached to the distal tip of the bundle in order to move the focal plane some distance away from the tip [10, 175, 176]. This arrangement allows for thin endoscopes (300 μm – 1 mm), but the resolution is limited because of the required inter-core spacing of the bundle, which is in general 3 μm or more. A magnifying element can be used at the tip to improve the effective resolution, but in that case diffraction-limited spots may overfill the individual cores of the bundle, decreasing the system's collection efficiency [9]. In addition, magnification reduces the field of view below the probe's size.

Another approach is to add a miniature scanning mechanism at the tip of a single-mode fiber. For example, a MEMS scanner can be used to scan the light beam [177, 178] or the fiber tip itself can be scanned [179–181]. Such devices can reach diffraction-limited resolution, but have large probes of several millimeters.

5.1.2 Multimode fiber confocal microscopy

Here I investigate a digital implementation of confocal microscopy combined with multimode fiber imaging. For this, modal scrambling needs to be compensated both ways in order to select a particular focal volume during both excitation and detection. In the digital variant of confocal microscopy [182, 183], the light returning from the sample is recorded with digital holography in an intermediate plane, instead of being filtered by a physical pinhole in a conjugate plane. The field is then digitally propagated up to a virtual conjugate plane, where it forms a focus. The digitally focused field can finally be filtered with a virtual pinhole mask, making the detection spatially selective as in classical confocal microscopy. The digital detection of the optical fields provides a large flexibility in the signal processing, allowing for example the dynamic adjustment of the pinhole size as well as the measurement of new contrast metrics such as the focal phase or the focal width [184]. Here, it also allows correcting for the distortions due to the fiber before filtering with a pinhole.

Practically, a multimode fiber guides light to and from the location of interest of a sample, and reflection-mode (non-fluorescent) digital confocal detection is implemented for the light collected back through the fiber's tip. Prior to the experiment, the transmission matrix of the multimode fiber is measured. This matrix allows projecting arbitrary output patterns, as well as decode the fields propagating in the reverse direction through the same fiber (as explained in chapter 4). Then, the digital filtering is implemented as required for confocal microscopy. The purpose is to increase the imaging contrast in spot-scanned images, which is important for applications such as imaging inside scattering tissues. A correlation-based filtering technique is also introduced, which offers similar performance for a reduced computational cost.

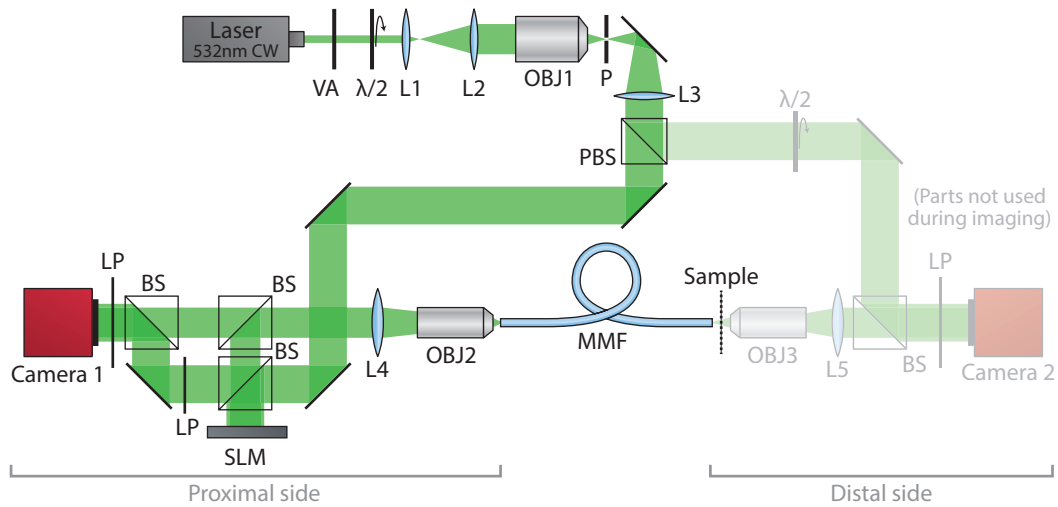


Figure 5.1: Digital confocal imaging setup. The components in faded colors are needed during the measurement of the matrix, but not during imaging. VA: variable attenuator; $\lambda/2$: half-wave plate; L1: $f = 30$ mm lens; L2: $f = 75$ mm lens; L3: $f = 200$ mm lens; OBJ1: infinity corrected 10x microscope objective; P: $10\ \mu\text{m}$ pinhole; L3: $f = 200$ mm lens; PBS: polarizing beamsplitter; BS: beamsplitter; LP: Linear polarized; SLM: spatial light modulator; L4, L5: $f = 250$ mm lens; OBJ2, OBJ3: 40x microscope objective; AP: variable aperture; MMF: multimode fiber with $\text{Ø}105\ \mu\text{m}$ core, NA 0.22 and 1 m length (Thorlabs M43L01).

5.2 Methods

5.2.1 Experimental setup

The output of a diode-pumped solid-state laser at 532nm (CNI MSL-FN-532-100mW) is spatially filtered and collimated to form a plane wave reference beam. After being split by a beamsplitter, the plane waves travel to each side of the multimode fiber. Off-axis holography is used to measure the fields coming out of the fiber. On each side, the fiber facet is first magnified with a microscope objective and imaged via a lens onto a camera sensor, where the light field is interfered with the reference plane wave. This is detailed in Figure 5.1. The angle between the reference and the object beam for off-axis holography is approximately 1.5° .

In the distal side, the holographic acquisition system is used only for calibration. It is the side where the sample is located, and during imaging no hardware is needed there besides the fiber itself. In the proximal side, a spatial light modulator (HoloEye Pluto) is used to illuminate the fiber with controlled patterns at a maximal rate of 20Hz, and a camera records the returning light fields.

There are two main differences with the “reverse image transmission” setup presented in section 4.3. First, the the sample is now illuminated via the fiber. Second, on the proximal side the same reference beam is no longer used for the SLM and Camera 1 (referring to Figure 5.1).

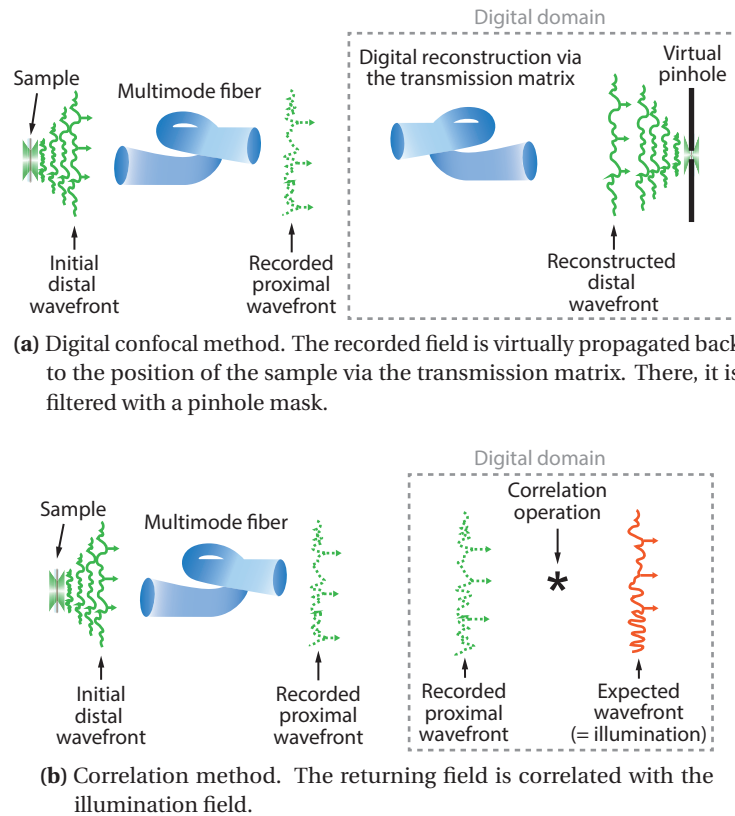


Figure 5.2: Illustration of the two digital processing methods for confocal microscopy

Instead, the reference is split by a beam splitter and a set of linear polarizers is used to reduce the intensity of the reference on Camera 1. This was necessary because the signal levels of the illumination and the reflected light beam are too different, and a too strong reference beam on Camera 1 would degrade the contrast of the holographic acquisition.

5.2.2 Digital processing algorithms

For the confocal scanning, the appropriate pattern is displayed on the proximal SLM in order to generate an excitation spot at a distance of approximately 100 μm in front of the distal fiber facet. This spot interacts with the sample at that location, and the reflected and backscattered light is collected back through the fiber. The field is then recorded holographically at the proximal side. One such measurement is performed for each position of the sample.

Three ways of processing the acquired data were tested. The first method simply integrates the total intensity of the proximally recorded field. This serves as a reference image, showing the contrast that would be obtained if the returning light were measured with a bucket photodetector without any further processing.

The second method is the “digital confocal method”. Here, the transmission matrix is used

to virtually propagate the backscattered field back through the fiber, and reconstruct it as it existed at the position of the sample. There, a digital pinhole mask is applied to suppresses all light contributions except those found within a radius of $1\ \mu\text{m}$ of the position of the excitation spot. Note that the Rayleigh radius for this wavelength (532 nm) and fiber NA (0.22) is $1.5\ \mu\text{m}$. The intensity that remains after filtering with the digital pinhole is integrated, and this value forms one pixel of the final image. This filtering scheme is illustrated in Figure 5.2(a).

The last method is the “correlation method”, and it is based on a different filtering principle. Consider the field that is sent from the proximal end in order to create a focus spot at the distal end of the fiber. The light originating from that same spot at the distal end and carrying the sample information propagates back through the fiber towards the proximal side, where it should lead to a similar field as was used for excitation (neglecting losses), simply because of the reciprocity of light propagation in this system. The phase conjugation literature [59, 185] provides formal and experimental proof of this principle. Any contribution of light not originating from the focal point should, on the contrary, lead to a proximal field that is uncorrelated with the excitation field due to the randomizing nature of modal scrambling. Therefore, the distal spot intensity can be estimated simply by calculating the linear projection (or correlation) of the returning field with respect to the excitation field, as shown in Figure 5.2(b). This operation is done for each scanning spot and the image is constructed pixel by pixel.

5.3 Results

The first set of experiments consisted of imaging of a human epithelial cell dried on a microscope cover glass. The results are shown in Figure 5.3(a-c). In each image, the signal is normalized between 0 and the maximum intensity. The image area is $81\ \mu\text{m}$ by $76\ \mu\text{m}$, and the step size is $1.1\ \mu\text{m}$. A control image made in white light transmission is shown in Figure 5.3(d).

A similar experiment with polystyrene beads spread on the surface of a cover glass is shown in Figure 5.3(e-g), with a control image in Figure 5.3(h). Here the area is $22.5\ \mu\text{m}$ by $22.5\ \mu\text{m}$, and the step size is $0.55\ \mu\text{m}$. To have an estimate for the resolution, I calculated the full width at half maximum of one of the reconstructed spots in the digital confocal image (Figure 5.3(f)), which is $1.5\ \mu\text{m}$.

In a second experiment, I made a transversal scan (z-scan) of a cover glass, as sketched in Figure 5.4(e). This is to illustrate the sectioning capability that can be obtained using the proposed filtering techniques. The results are shown in Figure 5.4(a-c). A control image is shown in Figure 5.4(d); it was taken on a commercial laser-scanning confocal microscope (Zeiss LSM 710) with an NA 0.3 objective. The average full width at half maximum of the interface is $12.7\ \mu\text{m}$ in the digital confocal image, $15.8\ \mu\text{m}$ in the correlation image, and $10\ \mu\text{m}$ in the control image. The ratio of the coverslip signal to the average background intensity between the interfaces is 22.5:1 in the digital confocal image (Figure 5.4(b)), 8.4:1 in the correlation image (Figure 5.4(c)) and 270:1 in the control image (Figure 5.4(d)).

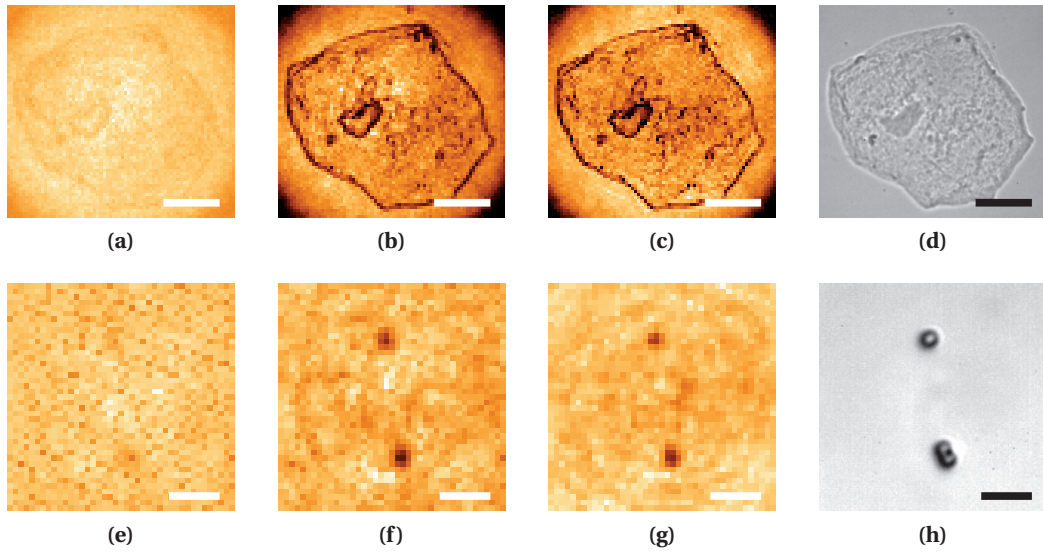


Figure 5.3: Results for the digital confocal method. (a-d) Microscopic image of a human epithelial cell reconstructed using (a) the total intensity method, (b) the digital confocal method, (c) the correlation method. (d) Control image taken in transmission, i.e. observed from the distal end under white-light illumination with a microscope objective and a camera. (e-h) 1 μm polystyrene beads imaged with (e) the total intensity method, (f) the confocal method, (g) the correlation method, (h) control. (a-d) Scale bar is 20 μm . (e-h) Scale bar is 5 μm .

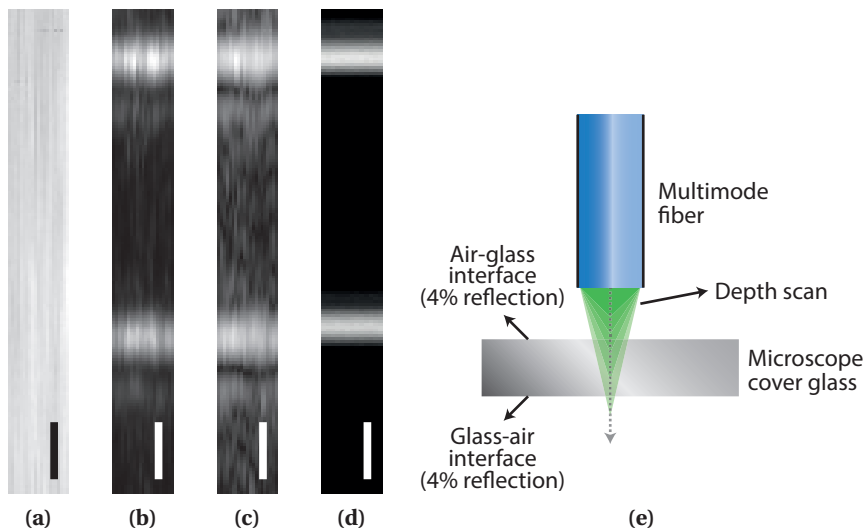


Figure 5.4: Transversal scans of a coverslip with the (a) total intensity method, (b) digital confocal method, (c) correlation method and (d) control image taken with a commercial confocal microscope. The scale bars represents 20 μm of distance in air. Note that the thickness of the coverslip is approximately 150 μm , but due to refraction it appears thinner in these images. The vertical axis is perpendicular to the coverslip, and the horizontal axis represents a lateral scan. (e) Schematic of the experiment.

5.4 Discussion

5.4.1 Contrast, sectioning and image quality

The comparison of the various methods in Figure 5.3 reveals that a significant increase in image contrast is achieved when filtering the backscattered light, versus the case where the whole field is integrated. By digitally implementing spatial selectivity in the detection, the walls and the nucleus of an epithelial cell in Figure 5.3(b,c) can clearly be distinguished. Also in the case of polystyrene beads, the filtering scheme was useful. With this sample, the intensity image has very little contrast in Figure 5.3(e), but the beads appear clearly on the confocal and correlation images Figure 5.3(f,g).

Similarly, the depth scans of Figure 5.4 show that reflective interfaces could not be resolved by simply recording the total backscattered intensity (Figure 5.4(a)), but they were made visible by the proposed filtering schemes (Figure 5.4(b,c)). Due to the limited numerical aperture of the fiber (NA 0.22), the axial resolution is relatively low in Figure 5.4 6(b,c). The numerical aperture explains part of the difference between these images and the control image from a traditional microscope (NA 0.3) in Figure 5.4(d). Note that the transmission matrix method is general and can be used with any type of fiber. Therefore, the steps outlined in this chapter can be extended to fibers with a higher numerical aperture or a larger core. However, this implies that a greater number of modes need to be sampled during calibration, and with a slow modulator it is preferable to keep this number low. The calibration takes 10 min. in this experiment.

Other factors play a role as well in determining the image quality obtained with this approach. In the experiments presented here, only one polarization of the light was used for experimental simplicity. Since the fiber acts as a depolarizing medium for linear polarization, half of the light is therefore lost each way. Polarization multiplexing techniques [74, 111] may improve the sensitivity by processing all of the light traveling through the fiber. An added benefit of polarization multiplexing would be the capability to do confocal polarization microscopy.

Finally, most phase-only spatial light modulators are known to cause aberrations due to the fact that their surfaces are not perfectly flat (as discussed in section 2.2). This induces a systematic error in the measurement of the transmission matrix. Because the same aberration is not present on the camera used for recording backscattered field, it is not possible to perfectly reconstruct the distal field from the proximally measured data. One possible solution is to use a modulator that is flat or corrected for such errors, or measure the deformation experimentally and correct for it [137].

5.4.2 Speed

The experiments presented here are currently limited in speed by the modulator. With a point-scanning rate of 20 Hz, the measurement shown in Figure 5.3(a-c) took 4 min 15 s to

acquire, Figure 5.3(e-f) took 1 min 24 s, and Figure 5.4(a-c) took 3 min. Faster modulators can be used, such as digital micromirror devices or a combination of an acousto-optic deflector with a spatial light modulators. These have been shown to work for similar applications [62, 64, 90, 124], and reach point-scanning rates of over 20 kHz.

The next limiting factors would be the speed of the acquisition (i.e. the frame rate of the camera), and lastly the computational load of reconstructing holograms. Digital off-axis holography is used here, and with this method the speed of reconstruction is mainly determined by speed of the necessary Fourier transform. On a computer with an Intel Xeon E5-2620, using the FFTW library, holograms of 800 by 800 pixels could be processed at a speed of 400 frames per second. Note that in the digital confocal method, two Fourier transforms are required: one to reconstruct the off-axis hologram captured in the proximal side, and one to reconstruct the distal field from the unscrambled Fourier coefficients calculated with the transmission matrix. With the correlation method, only the first transform is needed (for the holographic reconstruction).

The processing speed can be increased by making lower-resolution holograms. A lower-resolution means that the field of view has to be reduced, and/or the magnification of the optical detection system (OBJ2, L4, OBJ3 and L5 in Figure 5.1) should be reduced, leading to a smaller spatial frequency bandwidth. The resolution of 800 by 800 pixels that is used here is enough for fibers with a V number up to 400, e.g. a fiber with a core of 105 μm and NA 0.65 or a fiber with NA 0.22 and a core of 310 μm at 532nm. This can be calculated with the formulas derived in section 2.3.

5.4.3 Digital pinhole versus correlation method

In effect, the pinhole method performs the same operation as a classical confocal microscope, while the correlation method acts more like a matched filter [186] measuring the amount of backscattered light bearing the same signature as the excitation light. The correlation method has a lower computational cost, because the returning field does not need to be transformed or reconstructed. However, there is also less flexibility in the signal processing, since the pinhole size cannot be adjusted and the reconstructed spots are not available for further analysis.

As opposed to the digital confocal method, the correlation method can be completely hardware-implemented by letting the backscattered field reflect on the SLM. This field will then be demodulated by the phase pattern currently being displayed. In other words, the backscattered field (the field to be filtered) will be multiplied by the illumination pattern (the field we wish to correlate with). After this operation, the light can simply be focused through a lens to obtain the Fourier transform, and a pinhole can be used to extract the DC-term of the resulting field. In this case, the acquisition speed would only be limited by the modulator.

5.4.4 Bending and stability

The proposed methods depend on the characterization of the fiber by the transmission matrix, and this transmission matrix changes depending on the bending state of the fiber. While there is a certain limited tolerance to bending [78, 86, 187], for practical applications it may be preferable to use a fiber immobilized inside a needle [60], as a rigid endoscope. The small outer diameter (125 - 300 μm) of multimode fibers is compatible with some of the thinnest needle gauges, so this constitutes a minimally invasive method for deep-tissue microscopy.

Bending will be discussed in more detail in chapter 7. The solutions proposed in the prior literature are listed here briefly. One idea is to use a semi-rigid probe, with a calibration stored for a discrete set of bending states [86], or compensating bending in real-time with a fast feedback system [90]. By using two-photon fluorescence as a feedback signal and exploiting the structure of light patterns in graded-index fibers, it is possible to obtain the calibration of the fiber without access to the distal end [91].

Recently, it was demonstrated that the transmission matrix of a fiber can be calculated instead of being measured [74]. It is also possible to calculate the matrix for different bending states of the fiber. This study suggests that it may be possible to compensate for the bending of the fiber by recalculating the matrix in real-time. The images acquired through the fiber endoscope could be used as feedback signal in order to estimate the bending state.

Another important point with regard to the proposed applications is the temperature stability of the transmission matrix. According to a previous report [102], the temperature variation needed to decorrelate a speckle pattern through a 1 m long fiber is 8°C, and this scales inversely with fiber length. Therefore, it may be necessary to calibrate the fiber at the temperature of the body, but there is otherwise enough temperature margin for most endoscopic applications.

5.5 Conclusion

The principle of confocal filtering is broadly applicable, even in cases where the light paths towards the focal volume are severely distorted. The schemes presented here can be generalized to any system a transmission matrix can be measured, e.g. also in scattering media [18].

In the context of biomedical imaging, the multimode fiber can be calibrated outside the tissue of interest, and then inserted at another location (i.e. inside the tissue) for imaging. The proposed system does not have any distal scanning optics, and the probe diameter can therefore be as thin as the fiber itself. The focal plane can be chosen dynamically by appropriate modulation from the proximal side.

In summary, two different ways of obtaining a confocal filtering effect via multimode fibers were demonstrated (with a digital pinhole or using correlation). Confocal reflectance imaging via a multimode fiber has potential applications in the endoscopic high-contrast imaging of cells, either label-free or with scattering probes such as nanoparticles.

6 Correlation-based confocal imaging

This chapter builds on the results of the digital confocal method and proposes an all-optical technique to obtain sectioning through a distorting medium such as a fiber.

This chapter corresponds to the following publications:

- Damien Loterie, Sebastianus A. Goorden, Demetri Psaltis, and Christophe Moser. Confocal microscopy through a multimode fiber using optical correlation. *Optics Letters*, 40(24):5754–5757, December 2015.
- Damien Loterie, Demetri Psaltis, and Christophe Moser. Confocal microscopy via multimode fibers: fluorescence bandwidth. volume 9717, pages 97171C–1 to –6, 2016.

6.1 Introduction

When imaging inside a thick sample, light signals originating from any given image plane will always be superposed on an undesired contribution of light emanating from parts of the tissue outside the focal plane. This causes a blurring effect on the final image and decreases the overall contrast.

This problem can be solved in a number of ways. For example, two-photon fluorescence [70–72] or saturated excitation [69] have been proposed for imaging instead. As an alternative approach, I have demonstrated two computational methods to obtain confocal images via a multimode fiber (see chapter 5). Here, I improve upon these results and propose a way to obtain confocal images using optical correlation of the light signals returning from a multimode fiber. The main advantage of this optical implementation versus the digital approach reported before is that it is no longer necessary to record holograms during the imaging phase. This benefits the overall imaging speed (which is now limited only by the modulator), and the accuracy of the system: aberrations due to the non-flat surface of the SLM are automatically canceled out when the field returns back to the SLM. This was not possible in the digital implementation, because the returning field was processed using a camera, i.e. a separate device.

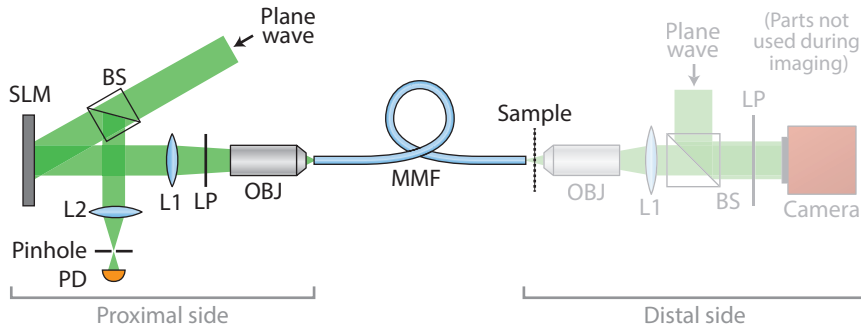


Figure 6.1: Diagram of the experimental setup.

BS: 50/50 beam splitter, SLM: HoloEye Pluto SLM, L1: $f = 250$ mm lens, L2: $f = 150$ mm lens, OBJ: Newport MV-40x objective, PD: Thorlabs PDA36A-EC photodiode, LP: linear polarizer, CAM: camera, MMF: multimode fiber. Proximal side: an incoming plane wave is shaped by an SLM, and relayed to the input facet of a multimode fiber via a lens (L1) and a microscope objective (OBJ). The light signals returning from the fiber are relayed back onto the SLM, and focused via a lens (L2) through a pinhole. A photodiode (PD) records the resulting signal. Distal side: during calibration, an off-axis holographic system records the output fields from the fiber using a camera (CAM). During imaging, a spot is scanned over the sample and the scattered/reflected light is collected back through the same fiber. The components in faded colors are needed during the calibration, but not during imaging.

6.2 Methods

6.2.1 Setup and fiber characterization

The first step of the measurement is to characterize the modal scrambling occurring in the fiber. This is done with a transmission matrix approach as described in detail in chapter 3. The experimental setup is illustrated in Figure 6.1. Briefly, a series of linearly independent input patterns is applied to one end of the fiber (Thorlabs M43L01, $\text{\O}105\ \mu\text{m}$ core, 0.22 NA) with a spatial light modulator (SLM), and the resulting output speckle patterns are recorded holographically on the opposite end. A complete set of such input-output measurements yields the transmission matrix. By inverting this matrix, it is possible to calculate which field needs to be shown on the SLM so that it creates a desired pattern on the opposite end, for example a spot. The side of the fiber with the modulator is referred to as the proximal side, and to the side where the sample is located as the distal side. During the calibration phase, the distal facet of the fiber is observed using an off-axis holographic acquisition system, but during imaging this hardware is no longer needed and only the sample should be present at the distal end.

6.2.2 Optical correlation

In the next step, a spot is scanned over a rectangular grid inside the sample by appropriate modulation on the SLM. For each spot, the light scattered or reflected from the sample is collected back through the multimode fiber, and re-imaged onto the SLM. Here, this returning light is modulated by the illumination pattern shown on the SLM at that time. This is the first part of the correlation operation. If the returning light signal is originating from the same spot that is currently being illuminated by the SLM, then this returning signal retraces the same path as the illumination light back through the fiber. The resulting wavefront at the SLM must be the phase conjugate of the illumination pattern, assuming time-reversal symmetry [60, 185]. If the returning light does not come back from the same spot that was illuminated (for example, it comes from a point in the background), then the resulting wavefront at the SLM will be decorrelated from the illumination pattern, due to the randomizing nature of modal scrambling in fibers.

After being modulated by the SLM, the returning signal is focused using a lens and then filtered by a pinhole in the Fourier plane of the lens. The pinhole extracts the zero-order term from the Fourier plane, i.e. the "average" of the incoming field. This completes the correlation operation: indeed, by multiplying a field with the conjugate of the pattern we want to extract from it, and then averaging out, we have carried out an optical equivalent [189–191] of the (non-normalized) correlation in mathematics, as shown in Equation 6.1.

$$\rho = \sum_i x_i y_i^* \quad (6.1)$$

The signal from the photodiode (PD in Figure 6.1) is proportional to $|\rho|^2$. A large amount of light returning from the illuminated spot results in a large photodiode signal. Light not originating from the illuminated spot is filtered away by the pinhole.

6.2.3 Point spread function simulation

The point spread function (PSF) of this system was calculated using a numerical simulation. For this purpose, a synthetic transmission matrix was generated based on the theory of mode propagation in step-index multimode fibers. It assumes a straight fiber of 1 m length, NA 0.22 and 105 μm core. Each step of the scheme described before was then simulated. The phase-only nature of the modulator is taken into account, as well as the modal scrambling of the fiber and the use of linear polarizers. The simulation does not account for aberrations due to the optics, and it assumes paraxial propagation.

The longitudinal (xz) sections of the PSF are shown in Figure 6.2 for various pinhole sizes: Figure 6.2(a) is for a pinhole of 1 Airy unit, Figure 6.2(b) is for 5 Airy units and Figure 6.2(c) is the wide field case without a pinhole. Note that the Airy unit is used in confocal microscopy to denote the size of a diffraction-limited spot when imaged in the pinhole plane. This unit allows representing the pinhole diameter on a scale that is independent of the magnification

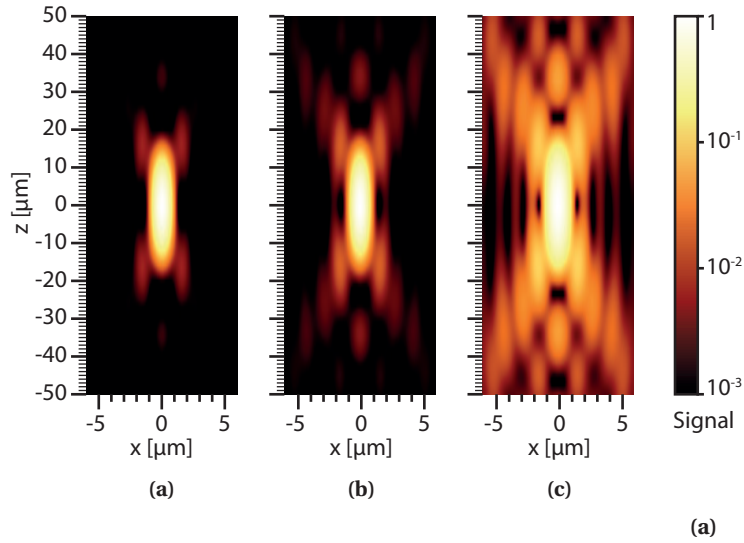


Figure 6.2: Simulated point spread function for a pinhole size of (a) 1 Airy unit, (b) 5 Airy units, and (c) without pinhole. The images are rendered using a logarithmic color scale.

of the optics used. In the present case, the pinhole is not in an image plane but in the Fourier plane relative to the SLM. Therefore, the Airy unit is defined here by the Airy spot obtained as the Fourier image of the fiber core through OBJ, L1 and L2.

The PSF with a 1 Airy unit pinhole (Figure 6.2(a)) is roughly proportional in magnitude to the square of the PSF without pinhole (Figure 6.2(c)). The total response integrated over each transverse plane (xy -slice) is comparable in every plane of the PSF without pinhole, whereas it decreases quickly as we move away from the focus when using a pinhole (sectioning effect). The lateral full width at half maximum (FWHM) resolutions are $0.95\ \mu\text{m}$, $0.96\ \mu\text{m}$ and $1.3\ \mu\text{m}$ respectively for Figure 6.2(a), (b) and (c). The axial FWHM resolutions are respectively $15.4\ \mu\text{m}$, $15.9\ \mu\text{m}$ and $21\ \mu\text{m}$.

6.3 Results

I experimentally verified the validity of the correlation confocal procedure on multiple samples. For comparison purposes, I used similar samples as in my previous study with computational processing (chapter 5). I made images "without" pinhole (Figure 6.3(a, c, e)) and with a $30\ \mu\text{m}$ pinhole, which is approximately 1 Airy unit in this implementation (Figure 6.3(b, d, f)). The images "without" pinhole actually use a large 2 mm pinhole, because otherwise stray light signals (e.g. an unmodulated portion of light from the SLM) also reach the detector; these signals are not related to the sample and would make a comparison inaccurate.

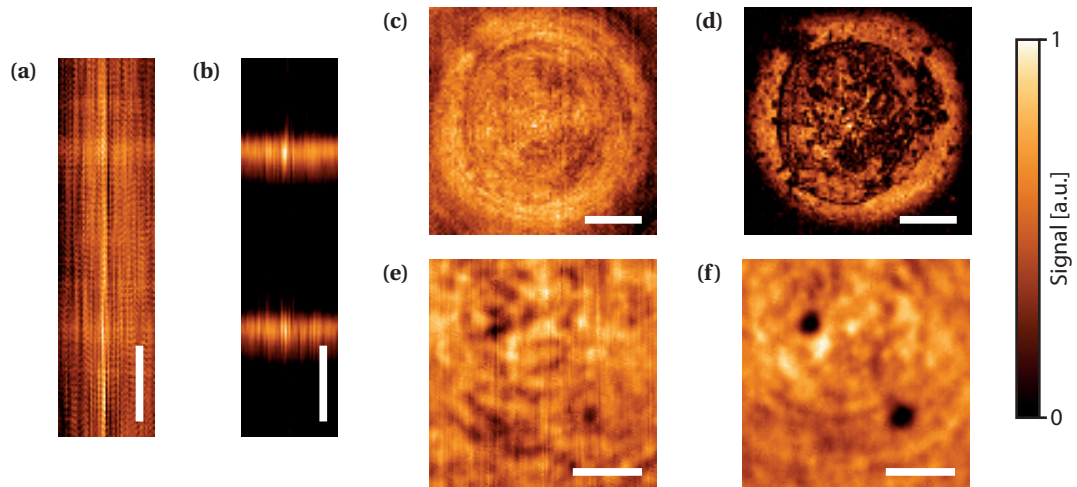


Figure 6.3: Experimental results (a,c,e) with a 2 mm pinhole and (b,d,f) with a 30 μm pinhole. (a-b) Depth-scan of a 150 μm cover glass. (c-d) Lateral scan of a human epithelial cell on the surface of a cover glass. (e-f) Lateral scan of 1 μm polystyrene beads on the surface of a cover glass. Each image is normalized between 0 and 1, where 0 is the minimum photodiode voltage recorded in the image and 1 is the maximum voltage.

6.4 Discussion

As shown in Figure 6.3(b), the optical correlation method clearly resolves the reflective interfaces of a cover glass. This is not possible without pinhole (Figure 6.3(a)). In the case of an epithelial cell (Figure 6.3(d)) or polystyrene beads (Figure 6.3(f)), the correlation method dramatically increases the obtained contrast versus non-filtered images (Figure 6.3(c, e)). To quantify the axial resolution, the average FWHM was calculated for the interface in Figure 6.3(b), and is 14.9 μm . The lateral FWHM resolution was estimated from a lateral scan of a 100 nm nanoparticle on a cover glass, and is approximately 1.3 μm . The difference with the simulation may be due to the low signal levels when measuring small nanoparticles with the current NA. The point-scanning rate is limited by the spatial light modulator at 20 Hz.

In this experiment, a fiber with NA 0.22 was used to limit the size of the transmission matrix (940 Mb of computer memory using double-precision complex numbers). This facilitates processing with commonly available computer resources. Note however that the scheme is adaptable to fibers with arbitrary NA, as well as other usage cases such as scattering media.

6.5 Considerations for fluorescence

Until now, only reflection confocal imaging was considered. The reflection mode has the advantage for in-vivo operation that no fluorescent probes need to be injected to the area of interest before it can be imaged, i.e. the technique works label-free [192, 193]. If a label is

desired, for example to target specific parts of a tissue, one should use scattering probes such as nanoparticles.

Since confocal microscopy is often used in biology to image fluorescent specimens, the current section discusses whether the proposed method can be extended to this case and what kind of performance can be expected.

6.5.1 Multispectral matrices

Modal scrambling, and therefore the transmission matrix, varies with wavelength [102]. In fluorescence imaging, at least two different wavelengths are needed (the excitation wavelength and the emission wavelength), so the transmission matrix should either be calculated [74] or measured [99, 194–196] at both wavelengths. Note that measurement requires a coherent laser source for both wavelengths.

Point illumination at the distal tip of the fiber can be obtained as before. The returning fluorescence signal, though, must be processed on the SLM with a different hologram adapted for the emission wavelength. The excitation and emission holograms must either be superposed at the same place on the SLM (but this leads to multiplexing losses), or both wavelengths must be separated by a dichroic beamsplitter and processed using separate SLMs or different portions of the same SLM.

6.5.2 Bandwidth of step-index fibers

Fluorescent emissions can have a considerable bandwidth. For example, the emission intensity full width at half maximum of Alexa-488 is 40 nm. It is therefore important to know over which span of wavelengths a single hologram can process fluorescent emissions captured through the fiber (i.e. the spectral decorrelation bandwidth).

In general, the achievable bandwidth will depend on the dispersion characteristics of all the components in the measurement chain. The calculations below will neglect the wavelength-dependent response of liquid crystal SLMs, the chromatic dispersion of glass and the detector's bandwidth. Only the effects of modal dispersion in step-index multimode fibers are taken into account.

I wrote a simulation that calculates the theoretical modes of a step-index optical fiber (see Appendix A). The modes and their associated propagation constants are used to simulate the propagation of a light field originating from a spot on the fiber facet through a certain length L of straight fiber at a given central wavelength λ_0 . Because each mode has a different propagation constant, the initial spot is quickly randomized to a speckle field as it propagates through the fiber. The same simulation is run again for a range of different wavelengths λ' around λ_0 , searching for when the speckle pattern at λ' decorrelates from the speckle pattern at λ_0 after a distance L of fiber propagation. This allows determining the correlation bandwidth

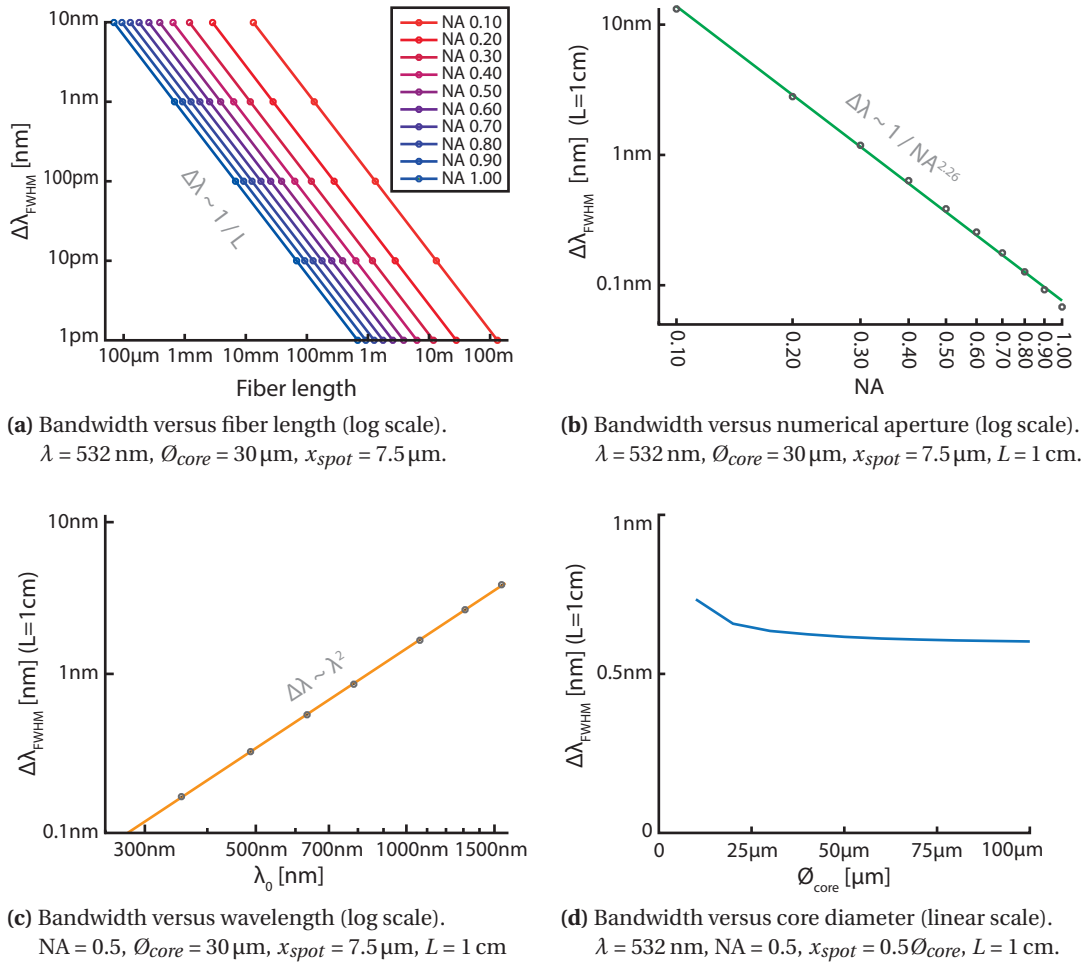


Figure 6.4: Dependence of the spectral decorrelation bandwidth of a step-index fiber versus various parameters.

$\Delta\lambda_{FWHM}$, which is defined here as the full width at half maximum bandwidth over which the correlation coefficient between the speckle patterns at λ' and λ_0 is above 0.5 in amplitude. Note that this bandwidth is calculated using field amplitudes. In an experimental setting, one must take into account the squaring effect of intensity detectors so that the bandwidth as defined here turns into a full width at *quarter* of maximum.

6.5.3 Simulation results

The results of the simulations can be found in Figure 6.4. Figure 6.4(a) is a graph of the FWHM correlation bandwidth $\Delta\lambda_{FWHM}$ for various numerical apertures in function of the fiber length L . The dependence of the bandwidth on the numerical aperture itself is shown on a logarithmic scale in Figure 6.4(b) for a fiber with a length of 1 cm. The dependence on the wavelength is shown in Figure 6.4(c), and on the core diameter in Figure 6.4(d). In each graph,

Chapter 6. Correlation-based confocal imaging

the dots represent results from the simulation. In Figure 6.4(a-c) the solid lines are fitted.

Except where otherwise noted, the central wavelength of emission λ_0 is 532 nm, the diameter of the core \varnothing_{core} is 30 μm , the refractive index of the core n_{core} is 1.4607, the numerical aperture $NA = \sqrt{n_{core}^2 - n_{cladding}^2}$ is 0.5 and the length of the fiber L is 1 cm. The position of the initial emission spot relative to the center of the fiber core is denoted x_{spot} and is 7.5 μm .

In addition to these graphs, I calculated if the simulated bandwidth depended on the position of the emission spot x_{spot} . As the spot is moved from the center of the fiber core to the edge, the bandwidth decreases monotonically to 90% of its value at the center (for $\lambda = 532$ nm, $\varnothing_{core} = 30$ μm , $NA = 0.5$, $L = 1$ cm).

6.5.4 Discussion

The bandwidth is inversely proportional to the length of the fiber (Figure 6.4(a)): $\Delta\lambda_{FWHM} \propto 1/L$. It decreases with increasing numerical aperture, following a power law $\Delta\lambda_{FWHM} \propto 1/NA^{2.26}$ (the exponent was calculated by fitting the results of Figure 6.4(b)). It increases with wavelength as $\Delta\lambda_{FWHM} \propto \lambda^2$. The bandwidth does not depend much on the core diameter (consistently with prior results in literature [102]).

At 532 nm, a 1 cm long step-index fiber with an NA of 0.30 has approximately 1.2 nm of spectral decorrelation bandwidth. This covers only a limited portion of a typical fluorophore's emission spectrum. To implement fluorescence imaging with high sensitivity, a broader bandwidth will be necessary than provided by step-index fibers. This may be possible with graded-index fibers, which have less modal dispersion properties (as demonstrated e.g. for the transmission of ultrashort pulses [197]).

6.6 Conclusion

In conclusion, I developed an all-optical method to obtain confocal images through a multimode fiber. This method uses only a spatial light modulator to improve imaging contrast and give a sectioning capability. These results could be relevant in future applications such as multimode fiber endoscopy in thick biological tissues.

If fluorescence imaging is desired, a multispectral matrix should be used. Additionally, a fiber with a larger spectral decorrelation bandwidth than step-index fibers would be needed, e.g. a graded-index fiber.

7 Bend translation

In this chapter, a sliding bend is shown preserve the propagation characteristics of a multimode fiber as described by the transmission matrix, while altering the shape of the fiber.

This chapter corresponds to the following publication: Damien Loterie, Demetri Psaltis, and Christophe Moser. Bend translation in multimode fiber imaging. *Optics Express*, 25(6):6263–6273, March 2017.

7.1 Introduction

An important question in multimode fiber imaging is how to manage the bend-induced changes in propagation characteristics of multimode fibers. These changes usually occur after deformations of the order of a few millimeters [65, 78, 86]. Several compensation mechanisms have been proposed. For example, multiple calibrations can be stored for different spatial configurations of the fiber in a semi-rigid endoscope setting. The correct calibration can be loaded based on feedback from a passive holographic beacon at the distal tip [86]. Using a photodetector in the distal end and fast electronic feedback, the system can be recalibrated on a millisecond timescale [90]. Recently, mechanisms were proposed to correct the distortions by exploiting the reflections from the distal facet of the fiber [88, 89]. Finally, a theoretical model describing light propagation in bent fibers was introduced and verified experimentally [74], allowing the propagation characteristics to be predicted based on the curvature at every location and on the physical parameters of the fiber.

This chapter takes a closer look at the following question: are there any ways to significantly alter the geometrical shape of the fiber, while conserving constant propagation characteristics? It is shown here that this is possible when a bend with constant shape is translated along the length of a multimode fiber. This effect is observed to different extents on various fibers. Practically, this could be exploited for example to allow a multimode fiber imaging device to translate longitudinally over a certain distance inside a rigid conduit such as a catheter, after having determined the propagation characteristics of the whole device in its initial state.

Under the assumption that mode coupling can be neglected, the fiber should maintain approximately the same propagation characteristics independently of the location of the bend [199, 200]. The goal of the following experiments is to verify if this assumption holds in practice, to compare various types of fibers using a translating bend, and to quantify differences in bend sensitivity between the fibers.

7.2 Methods

7.2.1 Overview

To assess bending behavior, a constant pattern of light was projected into the fiber core, and the output pattern on the other end of the fiber was monitored while translating the bend. The amount of change in the output gives a measure of how sensitive the fiber is to a displacement of the bend. The experimental setup is described in more detail in the subsection 7.2.2.

As these experiments revealed, the results depend on the fiber's specifications but also on the type of pattern being displayed. This is why a spatial light modulator (SLM) is included in the illumination path, as shown in Figure 7.1. The SLM allows testing bending sensitivity under different launch conditions, for example with speckle inputs or shaped inputs that create focused spots at the output. This will be explained in subsection 7.2.3 and subsection 7.2.4 respectively.

All measurements were validated using simulations, which are described in subsection 7.2.5.

7.2.2 Experimental setup

The setup uses spatially filtered, collimated light from a 532 nm laser (CNI MSL-FN-532-100mW). The light is modulated by a phase-only spatial light modulator (HoloEye Pluto VIS), as shown in Figure 7.1. The modulated light is then relayed via a lens (L1, $f = 200$ mm) and microscope objective (OBJ1, Newport MV-60X NA 0.85) to the fiber under test. The fiber passes through a sliding jacket (Teflon tube) that allows an S-bend with constant shape to be translated between the two ends of the fiber. The light output obtained on the distal side of the fiber is expanded by a microscope objective (OBJ2, Newport MV-40X NA 0.65) and a lens (L2, $f = 250$ mm)¹ and observed on a camera (PhotonFocus MV1-D1312-G2). For the speckle experiments, an off-axis reference beam was also superposed to the output pattern, to make an off-axis holographic recording of both the amplitude and the phase of the speckles [28]. The bend has a peak curvature of 40 m^{-1} and the overall length of the fiber is around 250 mm.

All fibers were tested without protective jacket or connectors (bare fibers). The fiber lengths varied between 235 mm and 250 mm (the variations are due to the cleaving process). The list of the tested fibers is shown in Table 7.1.

¹The focal length of this lens was erroneously reported as $f = 200$ mm in the paper [198].

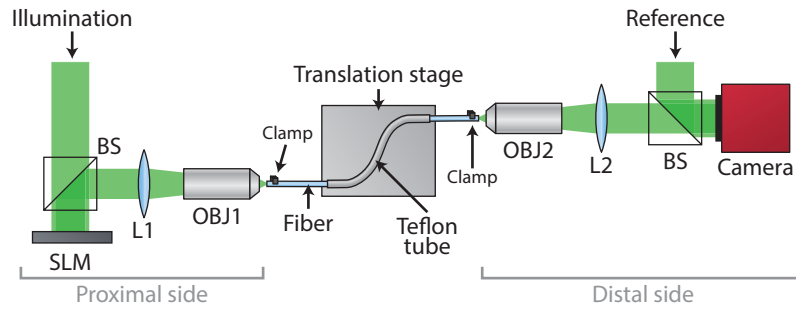


Figure 7.1: Experimental setup for imaging during translation of a bend in the fiber.

Label	Model	Supplier	Index	NA	Diameter
S1	FG050LGA	Thorlabs	Step	0.22	50 μm
S2	FG105LCA	Thorlabs	Step	0.22	105 μm
S3	FG200LEA	Thorlabs	Step	0.22	200 μm ^a
S4	FT200EMT	Thorlabs	Step	0.39	200 μm ^a
S5	GOF85	Schott	Step	0.64	70 μm
G1	GIF625	Thorlabs	Graded	0.29	62.5 μm
G2	F-MLD	Newport	Graded	0.29	100 μm

Table 7.1: List of fibers and nominal specifications.

^aFor fibers with a core size of 200 μm , only 80% of the core's surface was imaged on either end due to field of view limitations.

The fiber under test is held in place on each of its ends by a clamp (see Figure 7.1). In between, the fiber passes through a section of PTFE tubing (inner diameter 550 μm , outer diameter 1.08 mm) which constrains the fiber to a specific geometric shape. The tubing is taped to a motorized translation stage (Thorlabs PT1-Z8), which allows the bend to be smoothly translated along the fiber over a range of 25 mm. The precise shape of the bend is drawn in Figure 7.2. The shortest radius of curvature along the bend is approximately 25 mm.

7.2.3 Speckle patterns

The first set of test inputs are random speckle patterns. For each fiber, a speckle pattern was calculated to fill the entire fiber core, and to contain all possible angles of illumination up to the numerical aperture of the fiber under test. Such a speckle pattern is generated starting from a complex image where the real and imaginary part of every pixel is set by a random number generator following a normal distribution. Then, the image is filtered in the spatial and the Fourier domain by circular masks, limiting the spatial and angular extent of the pattern

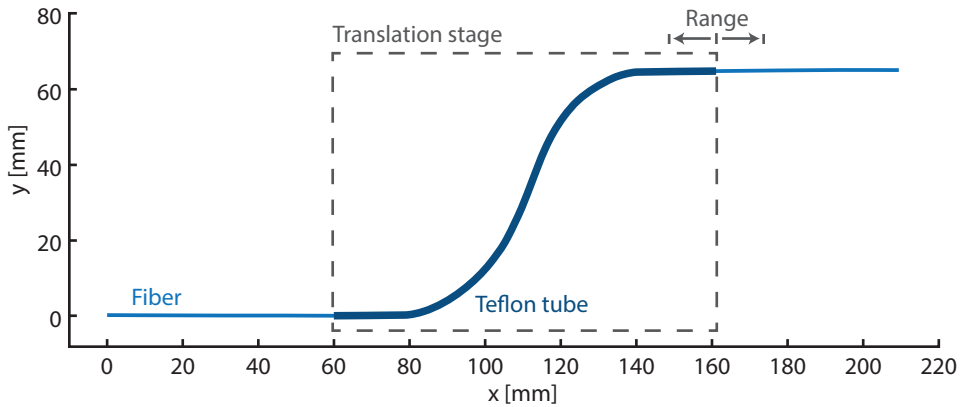


Figure 7.2: Shape of the bend used in these experiments

to the specified fiber core diameter and NA. When this pattern is displayed on the SLM, it excites every mode of the fiber under test randomly.

With a speckle as input, the output pattern on the other side of the fiber is also a speckle pattern. This output speckle is measured holographically for different displacements of the bend. Then, the amplitude and phase distribution of the output at each bend position is compared to the initial output using the correlation coefficient [158] as defined in Equation 3.3 on p. 36. In other words, we are calculating the autocorrelation of the output under bend translation, i.e. the correlation of the output with itself at various displacements of the bend. When the autocorrelation decreases, it means that the output speckle has changed and therefore the propagation characteristics of the fiber have changed (since the input is constant).

7.2.4 Spot focusing

The speckle experiment described above is interesting to give a global view of fiber transmission, averaged over many input angles and positions. However, this is not necessarily representative of the spot focusing experiments done in the context of multimode fiber imaging. Whereas a random speckle input excites all the modes of the fiber randomly, a wavefront that is shaped to make spots excites the modes in a specific way [59]. A spot in the center of the core leads predominantly to the excitation of low-order modes (depending on the notation, these are the LP_{0n} [201], HE_{1n} [202], or $\psi_{(0,m)}$ [74] modes). As the spot is moved closer to the edge of the core, higher order modes are also excited. Because of this, the location of the spot influences the bending characteristics.

In order to obtain results that can directly be related to imaging performance in multimode fiber imaging systems based on spot-scanning, a series of experiments was also performed using shaped inputs. For each fiber, an input wavefront was applied that causes the light to focus into a spot at the output of the fiber. The required input wavefront was found with the transmission matrix method as described in chapter 4. Then the intensity of the output spot

was recorded (non-holographically) as the bend was translated. For each fiber, this was done for two different spot locations: an output spot in the center of the fiber core, and an output spot halfway between the center and the edge of the fiber core.

The spot experiment presented here can be interpreted as an optical correlation experiment as well, similar to the one described in the previous section. In fact, the spot intensity is proportional to the magnitude squared of the correlation coefficient. The purpose of measuring the spot intensity experimentally in addition to the speckle autocorrelation is that spots excite a different subset of modes, and they are more meaningful measure for spot-scanning imaging applications (e.g. as in section 4.2).

7.2.5 Simulations

Modes of an optical fiber

For the step-index fibers, I made simulations to verify the results of the experiments. I used a vector mode propagation model [202] (i.e. including polarization effects). A brief explanation is given here. For more information, please refer to Appendix A. Propagation-invariant modes are patterns of light that retain their transverse amplitude and phase distribution as they propagate through a medium. In an optical fiber, only a limited set of such modes can be found that are guided through the fiber. Other modes radiate their energy away from the core of the fiber as they propagate. The guided modes can be found by solving a characteristic equation, which is derived from expressing the boundary conditions of Maxwell's equations at the interface between the core and cladding of the fiber.

By solving the characteristic equation, the propagation constants β_n , the order ν_n and transverse spatial profile of each mode n are determined. Because of the waveguide's symmetry, the electric field E_n of each mode can be written in a separable way using a cylindrical polarization basis, as shown in Equation 7.1. Here, the radial profile of mode n (i.e. $E_{r,n}(r)$, $E_{\phi,n}(r)$ and $E_{z,n}(r)$) is composed of Bessel functions [202].

$$E_n(r, \phi, z, t) = \begin{pmatrix} E_{r,n}(r) \\ E_{\phi,n}(r) \\ E_{z,n}(r) \end{pmatrix} e^{i\nu_n\phi} e^{i\beta_n z} e^{i\omega t} \quad (7.1)$$

Each mode E_n can be propagated along a straight segment of fiber by multiplying it with the phase factor $e^{i\beta_n L}$ where L is the length of the fiber segment. Arbitrary input fields must first be decomposed in an orthonormal basis of the fiber modes, yielding a set of modal coefficients. After that, each modal coefficient can be multiplied by the appropriate propagation phase factor $e^{i\beta_n L}$ to simulate propagation over a distance L . The linear combination of the modes, weighted by their modal coefficient at distance L , gives the spatial profile of an arbitrary input after propagating through a straight segment of fiber.

Propagation in bent fibers

For propagation in curved segments of fiber, I used the method proposed in [74]. Instead of multiplying each modal coefficient by a single phase factor, a matrix operation now has to be used since modes can couple to each other. The new modal coefficients are calculated from $c(L) = e^{iBL}c(0)$, where $c(L)$ represents the vector of modal coefficients at distance L , i.e. the phase and amplitude of each mode E_n at distance L . The matrix exponential e^{iBL} contains in its argument the matrix B defined by Equation 7.2,

$$B_{nm} = \beta_n \delta_{nm} - \left(\frac{n_{core} k_0}{\rho / \xi} \right) \langle E_n | x | E_m \rangle \quad (7.2)$$

where β_n is the propagation constant of mode n , δ_{nm} is the Kronecker symbol, n_{core} is the refractive index of the core of the fiber, k_0 is the magnitude of the wave vector of the light in vacuum, ρ is the curvature of the fiber segment and $\xi \approx 0.77$ is a correction factor to account for refractive index changes due to deformation-induced stress [74].

The factor $\langle E_n | x | E_m \rangle$ is given by Equation 7.3 and can be interpreted as the overlap between mode n and m , weighted by the position coordinate x along the axis of the bend.

$$\langle E_n | x | E_m \rangle = \iint E_n^*(x, y) x E_m(x, y) dx dy \quad (7.3)$$

This factor is equal to zero everywhere except between modes of neighboring order (i.e. when the order ν between mode n and m differ by ± 1 , or equivalently $|\nu_n - \nu_m| = 1$). This can be proven by inserting Equation 7.1 in Equation 7.3.

The x -axis in Equation 7.3 is oriented in the direction of the bend. When the bend changes orientation, a corresponding rotation should be applied to the bending operator [74]. In this case, the curvature changes its direction in the middle of the bend, as is evident from Figure 7.2. I accounted for this by letting the curvature ρ in Equation 7.2 become negative, which is equivalent to a 180° rotation of the x -axis at that point.

The bending operator describes propagation through a circular segment of fiber. Other shapes of bend must be approximated as a sequence of small circular segments. In the present simulations, the segment size was $250 \mu\text{m}$ for every simulated fiber.

Note that the bending operator e^{iBL} is in general not commutative: the order of two bends $e^{iB_1 L_1}$ and $e^{iB_2 L_2}$ matters in determining the overall propagation characteristics of a fiber. A different transmission matrix might be obtained if the locations of these bends were swapped. Incidentally, the experiments described in this chapter can be interpreted as a way to probe for commutativity. In particular, they test how well the propagation operator of an S-bend commutes with the propagation operator of straight segments of fiber.

Numerical implementation

The parameters for each fiber simulation were determined based on the corresponding experiments. The shape of the bend, shown previously in Figure 7.2, was estimated from a photograph of the experiment at right angle and at approximately 1m distance, with digital correction for the geometric distortion of the camera lens. The fiber's core size was set at the manufacturer's nominal value shown in Table 7.1. The refractive index of core was assumed to be that of pure silica (1.4607) at the working wavelength (532 nm). The refractive index of the cladding was calculated based on the specified NA in Table 7.1 and the index of the core.

For efficiency, the spot experiments were implemented in simulation using the time-reversal symmetry of electromagnetic waves: a spot was created as input to the bending simulation, and the outputs for various displacements were correlated with each other. The magnitude squared of the correlation coefficient corresponds to the experimental measurement of the spot intensity as noted in subsection 7.2.4.

The bending operator is described above as a multiplication with a matrix exponential. I applied a sparse numerical algorithm [203] for this calculation, and tuned it to exploit the specific block structure of the bending operator. Indeed, as stated before, all overlap factors $\langle E_n | x | E_m \rangle$ are equal to zero except between modes of neighboring order. As an example, a fiber with a 200 μm core and NA 0.39 (fiber S4 in Table 7.1) has over 100 000 modes at 532 nm, but less than 0.4% of the 10^{10} cross-coupling factors are nonzero. Bent propagation is therefore calculated from a sparse matrix, with a diagonal component representing 'normal' mode propagation and small block components representing coupling between modes of order ν and $\nu \pm 1$. The blocks are of variable size. Support for this particular matrix structure is not common in sparse algebra libraries, so I implemented C++ routines that handle this type of matrix operations in a multithreaded and cache-efficient manner.

These improvements allowed simulating bending with a large number of modes in a reasonable time. For example, propagating light through the bend for fiber S4 with 500 inputs and 500 bend segments takes 48 h on the lab's server (dual Intel Xeon E5-2670 2.6 GHz processors). Note that this problem is intractable with a non-sparse algorithm for this number of modes.

Graded-index fibers were not simulated. Their modes cannot be calculated as accurately due to the lack of an analytical solution and the requirement for the precise knowledge of the refractive index profile.

7.3 Results

In the first set of experiments, a static random pattern of light was applied to the input of the fiber and the output speckle was recorded holographically as the bend was translated. From the holographic recordings, the autocorrelation coefficient was calculated, which describes the similarity of the output between various states of translation of the bend. The experimental

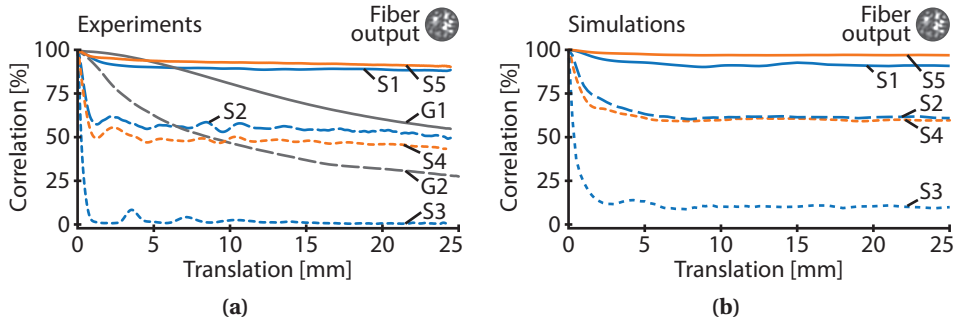


Figure 7.3: Autocorrelation of the output as the bend is translated, for a random input. (a) Experimental autocorrelation of the speckle pattern at the output of the fiber as the bend is translated. (b) Simulated autocorrelation for the step index fibers. Refer to Table 1 for the fiber specifications.

data is shown in Figure 7.3(a) and the corresponding simulations in Figure 7.3(b).

In a second set of experiment, the intensity of focused spots was measured at the output of the fiber, as shown experimentally in Figure 7.4(a) for a spot in the center of the core and Figure 7.4(c) for an off-center spot. The corresponding simulations are Figure 7.4(b) and (d) respectively. I also projected a line and a grid of spots at the output of the fiber (i.e. patterns where spots at many different positions are displayed simultaneously). The grid is shown in Figure 7.5(a) before deformation and in Figure 7.5(b) after deformation. The average full width at half maximum of these spots is 480 nm. The line is displayed in Figure 7.5(c) before deformation and in Figure 7.5(d) after deformation, showing the extent of the central region of the core where bending resilience is lower. The patterns in Figure 7.5 were made via fiber S5 (70 μm core, NA 0.64).

7.4 Discussion

Several interesting conclusions can be drawn from the data presented in Figure 7.3 and Figure 7.4. First, the data shows that with some fibers a bend can be translated over a few centimeters while still preserving a nearly constant output. However, the assumption of limited mode coupling is not universally applicable. For example, a fiber with a 200 μm core and NA 0.22 tolerates very little translation before the output is lost. In contrast, a fiber with the same NA but a smaller core of 50 μm has a much more stable output during the experiment: after 25 mm translation, the output remains constant to within 89% as measured by the correlation coefficient. In comparison with the diameter of the fiber, this is a significant distance.

The output patterns change more rapidly in fibers with larger core sizes, as can be seen by comparing the traces of fibers S1, S2 and S3 in Figure 7.3 and Figure 7.4. This behavior is expected from Equation 7.2, because the overlap factors $\langle E_n | x | E_m \rangle$ increase in magnitude

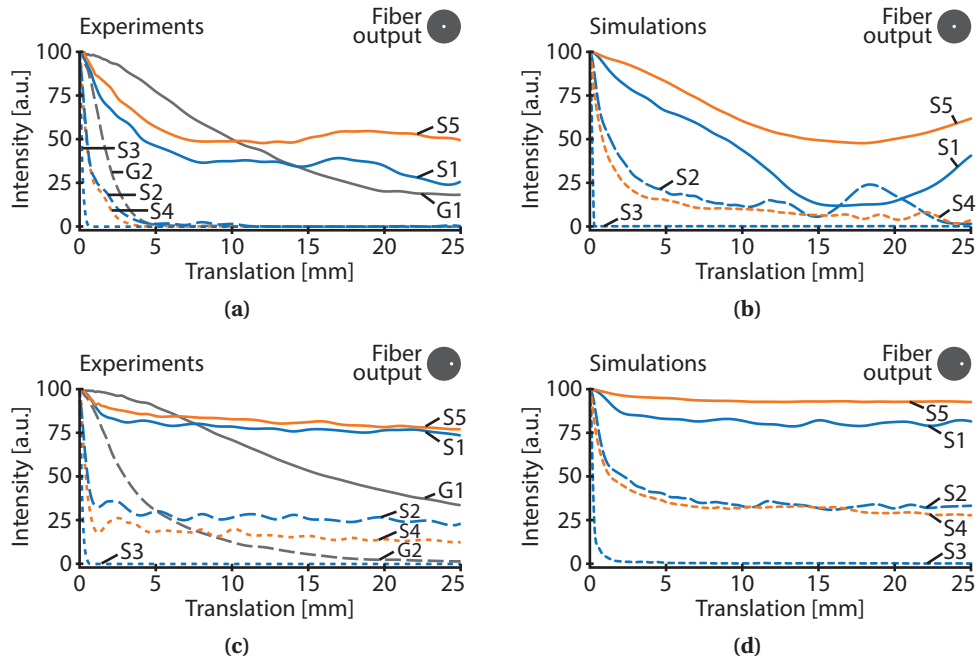


Figure 7.4: Change in intensity of a focused spot due to the translation of the bend. (a) Experiments and (b) simulations of the spot intensity in the middle of the fiber's core. (c) Experiments and (d) simulations for a spot half-way between the center and the edge of the core. Refer to Table 1 for the specifications of the various fibers.

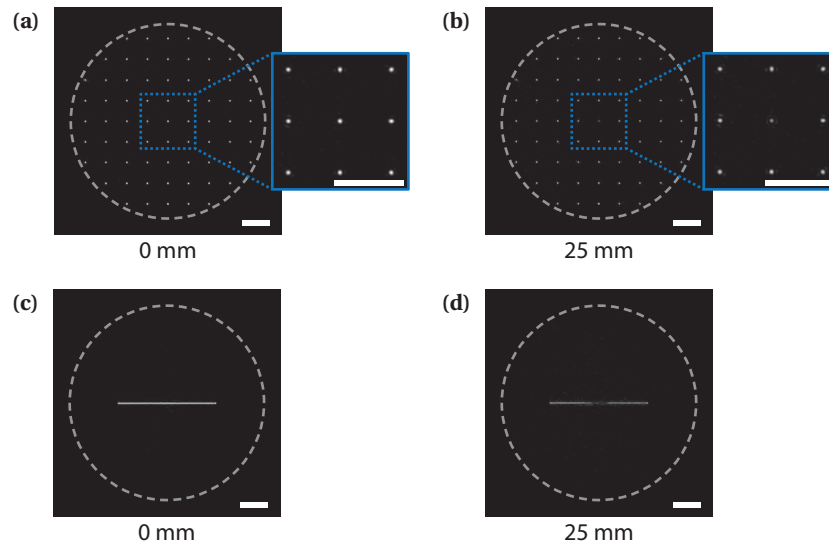


Figure 7.5: Patterns at the tip of a fiber before and after the bend is shifted. (a) Spots before translating the bend and (b) after 25 mm translation. The inset is a zoom on the center of the spot grid. (c) Line before translating the bend and (d) after 25 mm translation. The boundary of the core is indicated with a dashed circle. The scale bars are $10\ \mu\text{m}$.

Chapter 7. Bend translation

with increasing core diameter, so that the overall effect of bending is larger. On the contrary, the output patterns are more stable in fibers with larger NA, as can be seen by comparing fibers S1 and S5, or S3 and S4. Both core size and NA affect the number of modes in the same way (i.e. doubling either the core size or the NA quadruples the number of modes). However, an increase in core diameter increases the density of modes over the same range of propagation constants, whereas an increase in NA spreads the modes over a larger span of propagation constants.

The step-index fibers show a sharp change in the output as the bend is moved from its initial position, but after this point there is a plateau phase where the output remains constant over a large range. This behavior is consistent across the experiments in Figure 7.3(a) and Figure 7.4(c) and the corresponding simulations in Figure 7.3(b) and Figure 7.4(d). In the simulations, it was possible to verify that this plateau extends to much larger distances. For example, the intensity of an off-center spot in fiber S5 remains the same to within 1% whether the bend is translated by 25 mm or 1 m (assuming a fiber that long). Graded-index fibers show a different trend. While the range over which they maintain the output is rather large, graded-index fibers do not exhibit the plateau behavior and the integrity of the output keeps decreasing as we move away from the starting position.

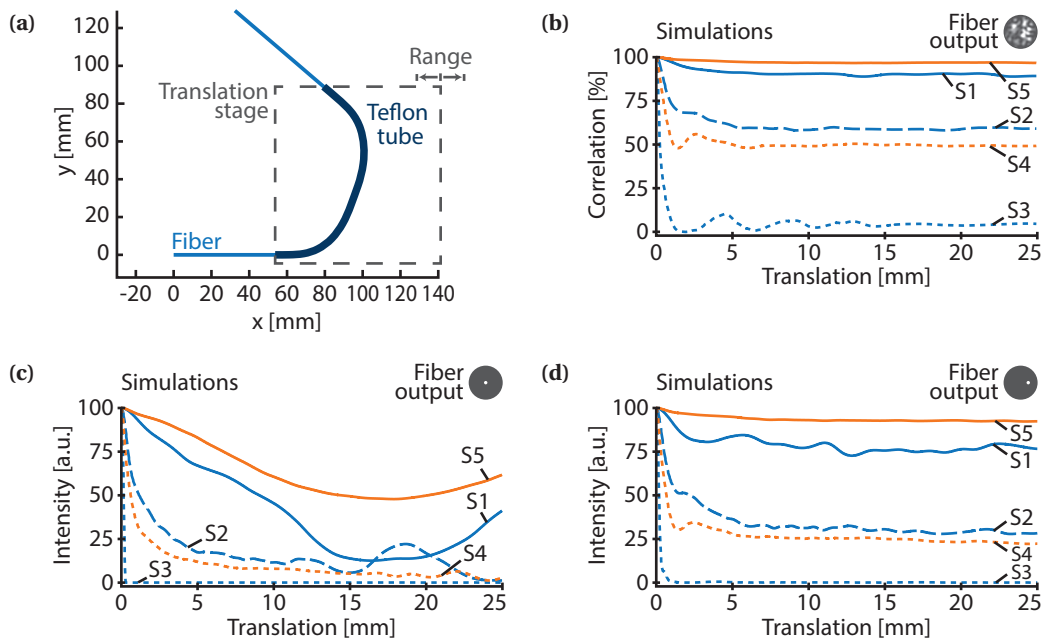


Figure 7.6: Simulation of a U-shaped bend. (a) Bend having the same absolute curvature as in Figure 7.2, except the curvature is everywhere positive. (b) Correlation versus horizontal translation of the bend. (c) Spot intensity in the center of the core and (d) intensity of an off-center spot versus translation of the bend.

The type of excitation has a great influence on the bending stability. For speckle (Figure 7.3) or off-center spots (Figure 7.4(c) and (d)), the output can be maintained over a significant range for certain fibers. However, for spots created in the center of the core (Figure 7.4(a) and (b)), the stability of the output is much lower and the spots disappear monotonically as the bend is translated in all cases. This shows the large difference in bending sensitivity between the low order modes and the high order modes. For fiber imaging, it means that the regions of the core that are not in the center have a much greater tolerance to this type of deformation. This is illustrated visually Figure 7.5 using a grid and a line pattern. The central region of the core is visibly attenuated after deformation, but the other spots maintain high intensities.

An important remark concerns the symmetry of the bend used in these experiments. For experimental simplicity, an S-shaped bend is used here which allows changing the shape of the fiber while both ends remain fixed. Since the first half of this curve has roughly the same shape as the second half except for an opposite curvature, one could hypothesize that some of the distortions incurred in the first half are somehow compensated when the light travels through the second half because of the symmetry. I have verified in simulation, however, that the effects discussed above also exist for a translating U-shaped bend. For a bend with the same absolute curvature as the S-bend in Figure 7.2, but with everywhere positive curvature value, I obtained similar intensity and correlation curves as shown in Figure 7.6.

7.5 Conclusion

I compared various multimode fibers with each other in terms of their ability to maintain a constant output while a bend is translated along their length. The results give an indication of the mode coupling effects in each fiber.

There are large differences in the stability of the propagation characteristics of fibers undergoing bending. Fibers with limited core sizes and large numerical apertures (e.g. 70 μm and NA 0.64) are resilient and maintain a nearly constant output over significant ranges. Fibers with large cores and small numerical apertures (e.g. 200 μm and NA 0.22) are very sensitive to any translation of the bend.

These findings may help select fibers with a greater tolerance to certain deformations, and motivate the search for other classes of deformations that preserve propagation characteristics. Finally, note that a sliding U-shaped bend could allow linear motion of the tip of a fiber while the other end remains fixed to the measurement apparatus. In conjunction with bending compensation techniques, this could improve the flexibility of imaging systems based on multimode fibers.

8 Conclusion

This thesis presents new methods and technical improvements for microscopic imaging through multimode optical fibers, which have the potential to greatly reduce the probe size of endoscopic tools.

8.1 Summary of the results

Digital holography and wavefront shaping were applied to realize imaging through multimode fibers. The tool making this possible is the transmission matrix, and an accurate procedure was developed to measure this matrix even for fibers with a large number of modes.

The transmission matrix was then used to transmit images through fibers in both directions. Controlled patterns can be generated at the tip of the fiber, and this can be used for example in two-photon spot-scanning microscopy. Imaging in the reverse direction (from the distal to the proximal end) was shown to be possible as well using the same transmission matrix as for pattern projection.

This bidirectional imaging capability was exploited to realize a digital form of confocal microscopy through fibers. As a result, a sectioning effect can be obtained and imaging contrast is increased. A correlation-based setup simplifies the application of this method by eliminating part of the computations.

Finally, the topic of bending was explored. This work revealed that under particular constraints, fibers can be deformed without loss of their propagation characteristics. The results of this sliding bend experiment are relevant to situations where a fiber would be pushed through a catheter or where the fiber could be constrained by a robotic arm to preserve its propagation characteristics.

8.2 Future work

In the course of this work, several aspects of multimode fiber imaging were identified that could be the topic of future work.

The matrix method as used in this work scales with the fourth power of the core diameter and resolution of the fiber fibers, as explained in subsection 3.2.3. This is a limiting factor when very high-resolution probes are needed with simultaneously a large field of view. More efficient algorithms could exploit the sparsity properties of the matrix (subsection 3.1.2) to drastically reduce the required amount of data and increase the speed of processing.

An interesting extension of the results of chapter 4 would be a system that could simultaneously illuminate and image a distal sample using a single holographic acquisition. As explained before, this is theoretically possible but difficult in practice because reflections and mismatches between camera and SLM need to be tightly controlled. Still, such a system would be particularly interesting since it would not rely on spot scanning and would therefore eliminate the speed issue. The images obtained this way would be holographic in nature (phase and amplitude).

For the confocal methods, the extension to fluorescence would enable certain biomedical applications that would otherwise not be possible due to the lack of contrast. As shown in chapter 6, confocal fluorescence imaging is not feasible with step-index fibers but could be done with graded-index fibers. A non-holographic method of processing the fluorescent signal would be needed. The optical correlation system of chapter 6 may be more appropriate in this case. In addition, a large increase in speed and sensitivity would be required to realize the high-performance fluorescent imaging expected by most biomedical researchers. This will require further progress concerning the optical tools used in these experiments, particularly the spatial light modulators.

The bending problem needs further study, but the results found so far in this work and in the prior literature are encouraging. With a better understanding of bending, efficient methods or algorithms could be developed to counteract its effects and allow fully flexible probes.

8.3 End word

Multimode fiber imaging is a promising solution for the further miniaturization of endoscopic tools. By compensating modal scrambling, it is possible to obtain images through an extremely thin probe (less than 300 μm). By using wavefront shaping, the focal plane can be adjusted dynamically once the probe is calibrated, without any optical elements being required on the distal tip of the fiber. The main challenges are the speed of imaging, bending tolerance and image contrast. In the course of this thesis, progress was made on some of these issues by investigating bidirectional imaging via fibers, by implementing confocal imaging, and by identifying bending states with constant propagation characteristics. This contributes to

realize a high-performance imaging device using only a single fiber as a relay element. Such a system, capable of diffraction-limited microscopy via an extremely thin probe, could be used e.g. to assist in biopsies or for other minimally invasive imaging applications.

A Fiber modes

In this appendix, light propagation through an optical fiber will be described on a theoretical level. The Maxwell's equations will be solved in an optical fiber, demonstrating the existence of discrete propagation modes. These modes are behind one of the main challenges in fiber endoscopy: as light travels through a bent fiber, the optical modes travel with different phase velocities. This leads to scrambling of the transported images.

The derivation in this appendix can be found in a shorter form in various articles [202,204] and textbooks [163,205–207]. The aim of this section is to give a detailed guide to the calculation of modes in a step-index fiber, with special attention to numerical aspects when solving the equations in software packages such as MATLAB.

A.1 From Maxwell's equations to the wave equation

Light is an electromagnetic wave which is described by Maxwell's equations. The Maxwell's equations in matter are:

$$\begin{cases} \nabla \cdot \vec{D} = \rho_{\text{free}} \\ \nabla \cdot \vec{B} = 0 \\ \nabla \times \vec{E} = -\frac{\partial \vec{B}}{\partial t} \\ \nabla \times \vec{H} = \vec{J}_{\text{free}} + \frac{\partial \vec{D}}{\partial t} \end{cases} \quad (\text{A.1})$$

These equations describe the propagation of electromagnetic waves in terms of the electric field \vec{E} , the magnetic field \vec{B} , the electric displacement field \vec{D} and the magnetizing field \vec{H} . The definition of the auxiliary fields \vec{D} and \vec{H} is:

$$\begin{cases} \vec{D} = \epsilon_0 \vec{E} + \vec{P} \\ \vec{B} = \mu_0 (\vec{H} + \vec{M}) \end{cases} \quad (\text{A.2})$$

Equations A.1 can be simplified in the present case. Optical fibers are typically made of a

Appendix A. Fiber modes

dielectric material like silica glass and contain no free charges ρ_{free} or free currents \vec{J}_{free} . In addition, these materials are nonmagnetic, and we will assume their dielectric behavior to be linear, isotropic and homogeneous. These assumptions are expressed as follows:

$$\begin{cases} \rho_{free} = 0 \\ \vec{J}_{free} = 0 \\ \vec{P} = \epsilon_0 \chi \vec{E} \\ \vec{M} = 0 \end{cases} \quad (\text{A.3})$$

With these assumptions, Maxwell's equations simplify:

$$\begin{cases} 0 = \nabla \cdot \vec{E} \\ 0 = \nabla \cdot \vec{H} \\ 0 = \mu_0 \frac{\partial \vec{H}}{\partial t} + \nabla \times \vec{E} \\ 0 = \epsilon_0 (1 + \chi) \frac{\partial \vec{E}}{\partial t} - \nabla \times \vec{H} \end{cases} \quad (\text{A.4})$$

This is a system of four first-order linear partial differential equations, which are now in terms of two fields \vec{E} and \vec{H} only. Using vector identities, we can rewrite this system of four first-order partial differential equations more conveniently as a system of two second-order partial differential equations:

$$\begin{cases} 0 = \nabla^2 \vec{E} - \frac{n^2}{c^2} \frac{\partial^2 \vec{E}}{\partial t^2} \\ 0 = \nabla^2 \vec{H} - \frac{n^2}{c^2} \frac{\partial^2 \vec{H}}{\partial t^2} \end{cases} \quad (\text{A.5})$$

Equation A.5 are called the wave equations. Each equation now involves only one field. The derivation can be continued using either equation; the other field is then uniquely determined by equations A.4. We choose to solve for the electric field \vec{E} :

$$0 = \nabla^2 \vec{E} - \frac{n^2}{c^2} \frac{\partial^2 \vec{E}}{\partial t^2} \quad (\text{A.6})$$

A.2 Wave equation in an optical fiber

The geometry of an optical fiber consists of a glass “core” cylinder of radius a , embedded in another glass “cladding” cylinder, as sketched in Figure A.1. We assume the fiber is straight, has infinite length, and that the cladding extends to infinity as well.

The refractive index of the core is higher than that of the cladding:

$$n_{core} > n_{clad} \quad (\text{A.7})$$

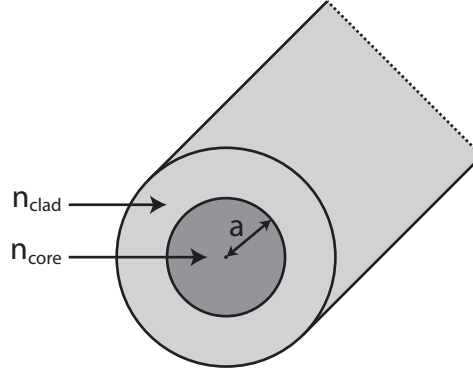


Figure A.1: Geometry of an optical fiber

For this geometry, a cylindrical coordinate system is appropriate:

$$0 = \nabla^2 \begin{pmatrix} E_\rho(\rho, \phi, z, t) \\ E_\phi(\rho, \phi, z, t) \\ E_z(\rho, \phi, z, t) \end{pmatrix} - \frac{n^2}{c^2} \frac{\partial^2}{\partial t^2} \begin{pmatrix} E_\rho(\rho, \phi, z, t) \\ E_\phi(\rho, \phi, z, t) \\ E_z(\rho, \phi, z, t) \end{pmatrix} \quad (\text{A.8})$$

We will solve this equation first for the E_z component of the electric field. The other components E_r and E_ϕ can be found later using Maxwell's curl equations.

$$0 = \nabla^2 E_z(\rho, \phi, z, t) - \frac{n^2}{c^2} \frac{\partial^2}{\partial t^2} E_z(\rho, \phi, z, t) \quad (\text{A.9})$$

To solve this partial differential equation, we will use the technique of separation of variables: we assume that the solution can be written as a product of functions of independent variables [205, 206].

$$E_z(\rho, \phi, z, t) = R(\rho)P(\phi)Z(z)T(t) \quad (\text{A.10})$$

In addition, we will assume a plane wave solution for the z and t variables. This is justified since the medium is time invariant, and the geometry along the z direction is assumed to be constant and infinite in size. Correspondingly, we expect eigenmodes with exponential form such as in free space:

$$\begin{cases} Z(z) = e^{-i\beta z} \\ T(t) = e^{i\omega t} \end{cases} \quad (\text{A.11})$$

Inserting the separated solution along with the plane wave assumption in the wave equation

Appendix A. Fiber modes

(in cylindrical coordinates) yields following equation:

$$\rho^2 \frac{R''(\rho)}{R(\rho)} + \rho \frac{R'(\rho)}{R(\rho)} + \rho^2 \left(\frac{n^2 \omega^2}{c^2} - \beta^2 \right) = - \frac{P''(\phi)}{P(\phi)} \quad (\text{A.12})$$

Because both sides are functions of different independent variables, this equation can only hold if both sides are equal to a constant, which we name ν^2 :

$$\begin{cases} \nu^2 = - \frac{P''(\phi)}{P(\phi)} \\ \nu^2 = \rho^2 \frac{R''(\rho)}{R(\rho)} + \rho \frac{R'(\rho)}{R(\rho)} + \rho^2 \left(\frac{n^2 \omega^2}{c^2} - \beta^2 \right) \end{cases} \quad (\text{A.13})$$

The equation for $P(\phi)$ is a second order linear differential equation with constant coefficients, and has a simple exponential solution:

$$P(\phi) = K_1 e^{i\nu\phi} + K_2 e^{-i\nu\phi} \quad (\text{A.14})$$

Note that since $P(\phi)$ is a function of an angle, it must be 2π -periodic. Therefore, ν must be an integer.

The equation for $R(\rho)$ is Bessel's equation. Its solution can be written in terms of the Bessel functions. Due to the core/cladding interface occurring at the core radius a , the solution is split in two parts:

$$R(\rho) = \begin{cases} Q_1 J_\nu(\kappa\rho) + Q_2 Y_\nu(\kappa\rho) & \rho \leq a \\ Q_3 K_\nu(\gamma\rho) + Q_4 I_\nu(\gamma\rho) & \rho > a \end{cases} \quad (\text{A.15})$$

$$\text{with } \begin{cases} \kappa = \sqrt{\frac{n_{\text{core}}^2 \omega^2}{c^2} - \beta^2} \\ \gamma = \sqrt{\beta^2 - \frac{n_{\text{clad}}^2 \omega^2}{c^2}} \end{cases} \quad (\text{A.16})$$

Similarly to linear second order differential equations with constant coefficients, where the solution can be written equivalently in terms of sine and cosine functions or in terms of exponential functions, the Bessel equation's solution can be written equivalently in terms of J_ν and Y_ν or in terms of K_ν and I_ν . The Bessel functions J_ν and Y_ν represent oscillatory behavior (compare to sine and cosine functions), while K_ν and I_ν are rapidly decaying/growing functions (compare to exponentials).

Inside the core ($\rho \leq a$), we expect an oscillatory behavior and thus we write the solution in terms of J_ν and Y_ν . In the cladding ($\rho > a$), we expect a rapidly decaying field because the light should stay confined in the core, hence we write the solution in terms of K_ν and I_ν . In addition, for notational convenience, we introduced the parameters κ and γ , which are direct functions of the z -direction propagation constant β .

The Bessel function Y_ν diverges for $\rho \rightarrow 0$, while I_ν diverges for $\rho \rightarrow \infty$. However, a physical solution for the wave equation in an optical fiber cannot diverge. Therefore, the radial solution can only contain J_ν and K_ν :

$$R(\rho) = \begin{cases} Q_1 J_\nu(\kappa\rho) & \rho \leq a \\ Q_3 K_\nu(\gamma\rho) & \rho > a \end{cases} \quad (\text{A.17})$$

The significance of the parameters κ and γ becomes clear in Equation A.17: κ defines the frequency of the amplitude oscillations of the modes in the radial direction, whereas γ defines the rate at which the modes decay outside of the cladding.

We have now determined $R(\rho)$, $P(\phi)$, $Z(z)$ and $T(t)$. Assembling the different parts of E_z , we obtain:

$$E_z(\rho, \phi, z, t) = \begin{cases} C_1 J_\nu(\kappa\rho) e^{i\nu\phi} e^{-i\beta z} e^{i\omega t} & \rho \leq a \\ C_3 K_\nu(\gamma\rho) e^{i\nu\phi} e^{-i\beta z} e^{i\omega t} & \rho > a \end{cases} \quad (\text{A.18})$$

Here we lumped together the constants by setting $C_1 = Q_1 K_1$ and $C_3 = Q_3 K_1$. The negative exponential term of Equation A.14 was dropped since it can be accounted for simply by letting ν become negative, i.e. $\nu \in \mathbb{Z}$.

Since the wave equation for \vec{H} is the same as that for \vec{E} (see Equation A.5), we expect the same type of solution for H_z :

$$H_z(\rho, \phi, z, t) = \begin{cases} C_2 J_\nu(\kappa\rho) e^{i\nu\phi} e^{-i\beta z} e^{i\omega t} & \rho \leq a \\ C_4 K_\nu(\gamma\rho) e^{i\nu\phi} e^{-i\beta z} e^{i\omega t} & \rho > a \end{cases} \quad (\text{A.19})$$

In Equation A.19, we have tacitly assumed that the parameters ν , β and ω are the same for \vec{H} and \vec{E} within a given mode. As will become clear in section A.3, this choice is necessary to satisfy the continuity conditions at the interface between core and cladding for all values of ϕ , z and t .

The remaining vector components can be found through Maxwell's curl equations:

$$\begin{cases} 0 = \mu_0 \frac{\partial \vec{H}}{\partial t} + \nabla \times \vec{E} \\ 0 = \epsilon_0(1 + \chi) \frac{\partial \vec{E}}{\partial t} - \nabla \times \vec{H} \end{cases} \quad (\text{A.20})$$

Using these curl equations, we can express the transversal field components E_ρ , E_ϕ , H_ρ and

H_ϕ in terms of the longitudinal fields E_z and H_z .

$$\begin{cases} E_\rho = \frac{i e^{i(z\beta - t\omega)} \left(\mu_0 \omega \frac{\partial H_z}{\partial \phi} + \beta \rho \frac{\partial E_z}{\partial \rho} \right)}{\rho (\beta^2 - \epsilon_0 \mu_0 (1 + \chi) \omega^2)} \\ E_\phi = \frac{i e^{i(z\beta - t\omega)} \left(\beta \frac{\partial E_z}{\partial \phi} - \mu_0 \rho \omega \frac{\partial H_z}{\partial \rho} \right)}{\rho (\beta^2 - \epsilon_0 \mu_0 (1 + \chi) \omega^2)} \\ H_\rho = \frac{i e^{i(z\beta - t\omega)} \left(\beta \rho \frac{\partial H_z}{\partial \rho} - \epsilon_0 (1 + \chi) \omega \frac{\partial E_z}{\partial \phi} \right)}{\rho (\beta^2 - \epsilon_0 \mu_0 (1 + \chi) \omega^2)} \\ H_\phi = \frac{i e^{i(z\beta - t\omega)} \left(\beta \frac{\partial H_z}{\partial \phi} + \epsilon_0 \rho (1 + \chi) \omega \frac{\partial E_z}{\partial \rho} \right)}{\rho (\beta^2 - \epsilon_0 \mu_0 (1 + \chi) \omega^2)} \end{cases} \quad (\text{A.21})$$

Using these equations, we can find the full vectorial solution for the fields in core and cladding:

$$\vec{E} = \begin{pmatrix} E_\rho \\ E_\phi \\ E_z \end{pmatrix} = e^{i\nu\phi} e^{-i\beta z} e^{i\omega t} \begin{cases} \begin{pmatrix} \frac{\mu_0 \nu \omega C_2}{\kappa} \frac{J_\nu(\kappa\rho)}{\kappa\rho} + \frac{-i\beta C_1}{\kappa} J'_\nu(\kappa\rho) \\ \frac{\beta \nu C_1}{\kappa} \frac{J_\nu(\kappa\rho)}{\kappa\rho} + \frac{i\mu_0 \omega C_2}{\kappa} J'_\nu(\kappa\rho) \\ C_1 J_\nu(\kappa\rho) \end{pmatrix} & \rho \leq a \\ \begin{pmatrix} \frac{-\mu_0 \nu \omega C_4}{\gamma} \frac{K_\nu(\gamma\rho)}{\gamma\rho} + \frac{i\beta C_3}{\gamma} K'_\nu(\gamma\rho) \\ \frac{-\beta \nu C_3}{\gamma} \frac{K_\nu(\gamma\rho)}{\gamma\rho} + \frac{-i\mu_0 \omega C_4}{\gamma} K'_\nu(\gamma\rho) \\ C_3 K_\nu(\gamma\rho) \end{pmatrix} & \rho > a \end{cases} \quad (\text{A.22})$$

$$\vec{H} = \begin{pmatrix} H_\rho \\ H_\phi \\ H_z \end{pmatrix} = e^{i\nu\phi} e^{-i\beta z} e^{i\omega t} \begin{cases} \begin{pmatrix} \frac{-n_{\text{core}}^2 \epsilon_0 \nu \omega C_1}{\kappa} \frac{J_\nu(\kappa\rho)}{\kappa\rho} + \frac{-i\beta C_2}{\kappa} J'_\nu(\kappa\rho) \\ \frac{\beta \nu C_2}{\kappa} \frac{J_\nu(\kappa\rho)}{\kappa\rho} + \frac{-i n_{\text{core}}^2 \epsilon_0 \omega C_1}{\kappa} J'_\nu(\kappa\rho) \\ C_2 J_\nu(\kappa\rho) \end{pmatrix} & \rho \leq a \\ \begin{pmatrix} \frac{n_{\text{clad}}^2 \epsilon_0 \nu \omega C_3}{\gamma} \frac{K_\nu(\gamma\rho)}{\gamma\rho} + \frac{i\beta C_4}{\gamma} K'_\nu(\gamma\rho) \\ \frac{-\beta \nu C_4}{\gamma} \frac{K_\nu(\gamma\rho)}{\gamma\rho} + \frac{i n_{\text{clad}}^2 \epsilon_0 \omega C_3}{\gamma} K'_\nu(\gamma\rho) \\ C_4 K_\nu(\gamma\rho) \end{pmatrix} & \rho > a \end{cases} \quad (\text{A.23})$$

A.3 Continuity conditions and characteristic equation

At the boundary between core and cladding, the field components tangent to the interface (i.e. E_z , E_ϕ , H_z and H_ϕ) must be continuous. This is required by the interface conditions for electromagnetic fields. For completeness, these conditions are given below in general form:

$$\begin{cases} \vec{n} \cdot (\vec{D}_{\text{core}} - \vec{D}_{\text{clad}}) = \rho_s = 0 \\ \vec{n} \cdot (\vec{B}_{\text{core}} - \vec{B}_{\text{clad}}) = 0 \\ \vec{n} \times (\vec{E}_{\text{core}} - \vec{E}_{\text{clad}}) = 0 \\ \vec{n} \times (\vec{H}_{\text{core}} - \vec{H}_{\text{clad}}) = \vec{j}_s = 0 \end{cases} \quad (\text{A.24})$$

A.3. Continuity conditions and characteristic equation

There are no free surface charges ρ_s or free surface currents \vec{j}_s in the problem under consideration, so these parameters were set to 0 in Equations A.24. The vector \vec{n} represents the normal to the interface between core and cladding.

Using the third and fourth equations in A.24, we see that the solutions for $\rho \leq a$ and $\rho > a$ must connect in $\rho = a$ for the components E_z , E_ϕ , H_z and H_ϕ . This yields following set of equations:

$$\begin{cases} K_v(a\gamma)C_3 = J_v(a\kappa)C_1 \\ \frac{1}{\gamma^2}(-\beta v K_v(a\gamma)C_3 - i a \gamma \mu_0 \omega K'_v(a\gamma)C_4) = \frac{1}{\kappa^2}(\beta v J_v(a\kappa)C_1 + i a \kappa \mu_0 \omega J'_v(a\kappa)C_2) \\ K_v(a\gamma)C_4 = J_v(a\kappa)C_2 \\ \frac{1}{\gamma^2}(-\beta v K_v(a\gamma)C_4 + i a n_{\text{clad}}^2 \gamma \epsilon_0 \omega K'_v(a\gamma)C_3) = \frac{1}{\kappa^2}(\beta v J_v(a\kappa)C_2 - i a n_{\text{core}}^2 \kappa \epsilon_0 \omega J'_v(a\kappa)C_1) \end{cases} \quad (\text{A.25})$$

This is a homogeneous linear system of equations in the amplitude parameters C_1 , C_2 , C_3 and C_4 .

$$\begin{pmatrix} J_v(a\kappa) & 0 & -K_v(a\gamma) & 0 \\ \frac{\beta v}{\kappa} \frac{J_v(a\kappa)}{a\kappa} & \frac{i\omega\mu_0}{\kappa} J'_v(a\kappa) & \frac{\beta v}{\gamma} \frac{K_v(a\gamma)}{a\gamma} & \frac{i\omega\mu_0}{\gamma} K'_v(a\gamma) \\ 0 & J_v(a\kappa) & 0 & -K_v(a\gamma) \\ -\frac{i\omega n_{\text{core}}^2 \epsilon_0}{\kappa} J'_v(a\kappa) & \frac{\beta v}{\kappa} \frac{J_v(a\kappa)}{a\kappa} & -\frac{i\omega n_{\text{clad}}^2 \epsilon_0}{\gamma} K'_v(a\gamma) & \frac{\beta v}{\gamma} \frac{K_v(a\gamma)}{a\gamma} \end{pmatrix} \begin{pmatrix} C_1 \\ C_2 \\ C_3 \\ C_4 \end{pmatrix} = \begin{pmatrix} 0 \\ 0 \\ 0 \\ 0 \end{pmatrix} \quad (\text{A.26})$$

In order to have a nontrivial solution for these amplitude parameters, the determinant of this system must be zero. This conditions yields following equation, called the ‘‘characteristic equation’’ of the fiber:

$$\left(\frac{\beta v c}{a^2 \omega}\right)^2 \left(\frac{1}{\gamma^2} + \frac{1}{\kappa^2}\right)^2 = \left(n_{\text{core}}^2 \frac{J'_v(a\kappa)}{a\kappa J_v(a\kappa)} + n_{\text{clad}}^2 \frac{K'_v(a\gamma)}{a\gamma K_v(a\gamma)}\right) \left(\frac{J'_v(a\kappa)}{a\kappa J_v(a\kappa)} + \frac{K'_v(a\gamma)}{a\gamma K_v(a\gamma)}\right) \quad (\text{A.27})$$

This equation is a transcendental equation in β (remember that κ and γ are functions of β). It describes for which β there exists a stable solution for a guided electromagnetic wave inside the fiber. These solutions are called the modes of the optical fiber.

Equation A.27 can be difficult to solve numerically. One problem is that the two factors on the right hand side of A.27 tend to produce pairs of solutions that are close to each other (and therefore difficult to distinguish), especially when the difference between n_{core} and n_{clad} is small.

To separate the solutions, we decompose the characteristic equation. Indeed, we can write the

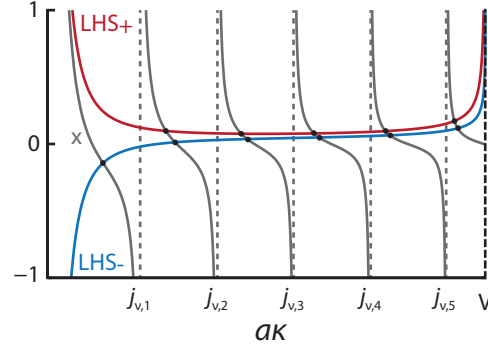


Figure A.2: Illustration of Equations A.30 for a particular set of fiber parameters. The solutions are indicated with black dots.

A.27 as a quadratic equation:

$$L^2 = (ux - vy)(x - y) \quad (\text{A.28})$$

$$\text{with } \begin{cases} u = n_{\text{core}}^2 \\ v = n_{\text{clad}}^2 \\ x = \frac{J'_v(a\kappa)}{a\kappa J_v(a\kappa)} = \frac{J_{v-1}(a\kappa)}{a\kappa J_v(a\kappa)} - \frac{v}{(a\kappa)^2} \\ y = -\frac{K'_v(a\gamma)}{a\gamma K_v(a\gamma)} = \frac{K_{v-1}(a\gamma)}{a\gamma K_v(a\gamma)} + \frac{v}{(a\gamma)^2} \\ L = \left(\frac{\beta v c}{a^2 \omega}\right) \left(\frac{1}{\gamma^2} + \frac{1}{\kappa^2}\right) = \frac{\beta v c}{a^2 \omega} \frac{u-v}{\gamma^2 \kappa^2} \end{cases} \quad (\text{A.29})$$

The constants u , v and the function y are positive real numbers, L is a real function and has the same sign as v , and x is a real oscillatory function with singularities at each zero of the Bessel function $J_v(a\kappa)$. The alternate forms of x and y can be derived from the identities of Bessel functions A.36, and the alternate form of L follows from the definition of κ and γ in A.16. Note that mode solutions can also be found using a different rewrite of the characteristic equation, see e.g. in reference [202].

The quadratic equation A.29 can be split in two solutions:

$$\begin{aligned} x &= \frac{(u+v)y + \sqrt{4L^2 u + (u-v)^2 y^2}}{2u} \quad (\text{LHS}_+) \\ x &= \frac{(u+v)y - \sqrt{4L^2 u + (u-v)^2 y^2}}{2u} \quad (\text{LHS}_-) \end{aligned} \quad (\text{A.30})$$

As an illustration, the solutions of Equations A.30 are shown in Figure A.2. It is a graph of the right hand side (x) and left hand sides (LHS_- and LHS_+) of A.30 versus the parameter $a\kappa$, for a particular value of the order v (there is one such graph for each $v \in \mathbb{Z}$). The solutions are found at the intersection of x with the left hand sides. These points are indicated by black dots.

A.4. Finding the amplitude coefficients

We expect only solutions where κ , γ and β are real numbers. This implies that $\kappa, \gamma \in [0, V]$ where $V = k_0 a \sqrt{n_{\text{core}}^2 - n_{\text{clad}}^2}$ is defined as the dimensionless frequency parameter of the fiber and $k_0 = \frac{2\pi}{\lambda_0} = \frac{\omega}{c}$ is the magnitude of the wave vector in vacuum. As a consequence:

$$n_{\text{clad}} k_0 < \beta < n_{\text{core}} k_0 \quad (\text{A.31})$$

These conditions can also be derived on physical grounds (see e.g. [163, p. 226] or [205, p. 112]).

Since x is a monotonic function with singularities at each zero $j_{\nu, n}$ of the Bessel function J_ν , the intervals where the solutions of A.30 are located can easily be delimited for a numerical root-solving algorithm. For a given order ν , the intervals are $[0, j_{\nu, 1}]$, $[j_{\nu, 1}, j_{\nu, 2}]$, ..., $[j_{\nu, \text{last}}, V]$ where $j_{\nu, n}$ is the n -th zero of J_ν , and $j_{\nu, \text{last}}$ is the largest zero smaller than V . In each such interval, there is exactly one solution for each equation of A.30, with a few exceptions. The last interval $[j_{\nu, \text{last}}, V]$ may not have a “minus” solution if x does not cross LHS_- , and the first interval $[0, j_{\nu, 1}]$ contains no solutions for $\nu = 0$ and only a “minus” solution for $\nu \neq 0$ (as shown in Figure A.2).

The solution intervals should be analyzed for each order ν until the order ν_{max} above which no more solutions can be found even in the first interval $[0, j_{\nu_{\text{max}}+1, 1}]$. To determine the intervals quickly and easily for any type of fiber, it is recommended to pre-compute all the zeros $j_{\nu, n}$ of the Bessel function J_ν up to a certain index n and order ν . Note also that the solution sets for ν and $-\nu$ share the same value of the parameters β , κ and γ (because ν appears only as ν^2 in the characteristic equation), so these values can be copied instead of solved again.

A.4 Finding the amplitude coefficients

Once the κ values (and therefore the β 's) of the modes are determined by solving the Equations A.30, the amplitude parameters C_i can be determined using the continuity conditions.

However, the coefficients C_1 and C_2 differ from C_3 and C_4 by a factor of $\frac{J_\nu(a\kappa)}{K_\nu(a\gamma)}$. Due to the faster-than-exponential decay of the modified Bessel function K_ν , this factor can rapidly exceed the range of representable numbers in double precision binary arithmetic. In numerical simulations, this leads in some cases to the false result that C_3 and C_4 are zero. We can determine the amplitude coefficients more reliably by using the following substitutions:

$$\begin{cases} C_1 \rightarrow A \\ C_2 \rightarrow \frac{i}{Z_0} B \\ C_3 \rightarrow \frac{J_\nu(a\kappa)}{K_\nu(a\gamma)} A \\ C_4 \rightarrow \frac{J_\nu(a\kappa)}{K_\nu(a\gamma)} \frac{i}{Z_0} B \end{cases} \quad (\text{A.32})$$

$$\text{where } Z_0 = \sqrt{\frac{\mu_0}{\epsilon_0}}$$

Appendix A. Fiber modes

The substitutions A.32 implicitly satisfy the first and third continuity equation from A.25. The remaining continuity conditions can be expressed in terms of the new coefficients A and B as:

$$\begin{pmatrix} \frac{\beta v c}{a^2 \omega} \left(\frac{1}{\gamma^2} + \frac{1}{\kappa^2} \right) & - \left(\frac{J'_v(a\kappa)}{a\kappa J_v(a\kappa)} + \frac{K'_v(a\gamma)}{a\gamma K_v(a\gamma)} \right) \\ - \left(n_{\text{core}}^2 \frac{J'_v(a\kappa)}{a\kappa J_v(a\kappa)} + n_{\text{clad}}^2 \frac{K'_v(a\gamma)}{a\gamma K_v(a\gamma)} \right) & \left(\frac{\beta v c}{a^2 \omega} \right) \left(\frac{1}{\gamma^2} + \frac{1}{\kappa^2} \right) \end{pmatrix} \begin{pmatrix} A \\ B \end{pmatrix} = \begin{pmatrix} 0 \\ 0 \end{pmatrix} \quad (\text{A.33})$$

With the substitutions of A.29, this can be rewritten more compactly as:

$$\begin{pmatrix} L & -(x-y) \\ -(ux-vy) & L \end{pmatrix} \begin{pmatrix} A \\ B \end{pmatrix} = \begin{pmatrix} 0 \\ 0 \end{pmatrix} \quad (\text{A.34})$$

The solution for the amplitude coefficients A and B can now be written explicitly, depending on kind of solution we obtain from the characteristic equation:

$$\begin{cases} A = 1, B = 0 & v = 0 \text{ and } ux = vy \\ A = 0, B = 1 & v = 0 \text{ and } x = y \\ A = 1, B = \frac{L}{x-y} = \frac{ux-vy}{L} & v \neq 0 \end{cases} \quad (\text{A.35})$$

A.5 Rewriting the field equations

The vectorial fields as described by Equation A.22 and A.23 have a singularity in $\rho = 0$. They can be reformatted to be more suitable for numerical calculations by using the new amplitude coefficients defined in A.32 and the following identities of Bessel functions:

$$\begin{cases} \frac{v}{z} J_v(z) = \frac{1}{2} (J_{v-1}(z) + J_{v+1}(z)) \\ J'_v(z) = \frac{1}{2} (J_{v-1}(z) - J_{v+1}(z)) \\ \frac{v}{z} K_v(z) = -\frac{1}{2} (K_{v-1}(z) - K_{v+1}(z)) \\ K'_v(z) = -\frac{1}{2} (K_{v-1}(z) + K_{v+1}(z)) \end{cases} \quad (\text{A.36})$$

The resulting field formulas are:

$$\vec{E} = \begin{pmatrix} E_\rho \\ E_\phi \\ E_z \end{pmatrix} = e^{i\nu\phi} e^{-i\beta z} e^{i\omega t} \begin{cases} \begin{pmatrix} \frac{i}{2\kappa} (-(\beta A - k_0 B) J_{v-1}(\kappa\rho) + (\beta A + k_0 B) J_{v+1}(\kappa\rho)) \\ \frac{1}{2\kappa} ((\beta A - k_0 B) J_{v-1}(\kappa\rho) + (\beta A + k_0 B) J_{v+1}(\kappa\rho)) \\ A J_v(\kappa\rho) \end{pmatrix} & \rho \leq a \\ \frac{J_v(a\kappa)}{K_v(a\gamma)} \begin{pmatrix} \frac{i}{2\gamma} (-(\beta A - k_0 B) K_{v-1}(\gamma\rho) - (\beta A + k_0 B) K_{v+1}(\gamma\rho)) \\ \frac{1}{2\gamma} ((\beta A - k_0 B) K_{v-1}(\gamma\rho) - (\beta A + k_0 B) K_{v+1}(\gamma\rho)) \\ A K_v(\gamma\rho) \end{pmatrix} & \rho > a \end{cases} \quad (\text{A.37})$$

$$\vec{H} = \begin{pmatrix} H_\rho \\ H_\phi \\ H_z \end{pmatrix} = e^{i\nu\phi} e^{-i\beta z} e^{i\omega t} \begin{cases} \frac{i}{Z_0} \begin{pmatrix} \frac{i}{2\kappa} ((k_0 u A - \beta B) J_{\nu-1}(\kappa\rho) + (k_0 u A + \beta B) J_{\nu+1}(\kappa\rho)) \\ \frac{1}{2\kappa} (-(k_0 u A - \beta B) J_{\nu-1}(\kappa\rho) + (k_0 u A + \beta B) J_{\nu+1}(\kappa\rho)) \\ B J_\nu(\kappa\rho) \end{pmatrix} & \rho \leq a \\ \frac{J_\nu(a\kappa)}{K_\nu(a\gamma)} \frac{i}{Z_0} \begin{pmatrix} \frac{i}{2\gamma} ((k_0 v A - \beta B) K_{\nu-1}(\gamma\rho) - (k_0 v A + \beta B) K_{\nu+1}(\gamma\rho)) \\ \frac{1}{2\gamma} (-(k_0 v A - \beta B) K_{\nu-1}(\gamma\rho) - (k_0 v A + \beta B) K_{\nu+1}(\gamma\rho)) \\ B K_\nu(\gamma\rho) \end{pmatrix} & \rho > a \end{cases} \quad (\text{A.38})$$

In A.38, note the difference between the order ν and $\nu = n_{\text{clad}}^2$ as defined in A.29.

The vector field components were given until now with respect to cylindrical unit vectors. To obtain the Cartesian (linearly polarized) representation of the field components, the following transformation is necessary (shown here for the electric field \vec{E}):

$$\begin{pmatrix} E_x \\ E_y \\ E_z \end{pmatrix} = \begin{pmatrix} \cos\phi & -\sin\phi & 0 \\ \sin\phi & \cos\phi & 0 \\ 0 & 0 & 1 \end{pmatrix} \begin{pmatrix} E_\rho \\ E_\phi \\ E_z \end{pmatrix} \quad (\text{A.39})$$

The transformation to Cartesian components complicates the expressions A.37 and A.38 even more. A transformation to a circular polarization basis, however, simplifies them somewhat. The circularly polarized components are related to the other representations as follows:

$$\begin{pmatrix} E_{\text{RCP}} \\ E_{\text{LCP}} \\ E_z \end{pmatrix} = \begin{pmatrix} \frac{1}{\sqrt{2}} & \frac{i}{\sqrt{2}} & 0 \\ \frac{1}{\sqrt{2}} & \frac{-i}{\sqrt{2}} & 0 \\ 0 & 0 & 1 \end{pmatrix} \begin{pmatrix} E_x \\ E_y \\ E_z \end{pmatrix} = \begin{pmatrix} \frac{1}{\sqrt{2}} e^{i\phi} & \frac{i}{\sqrt{2}} e^{i\phi} & 0 \\ \frac{1}{\sqrt{2}} e^{-i\phi} & \frac{-i}{\sqrt{2}} e^{-i\phi} & 0 \\ 0 & 0 & 1 \end{pmatrix} \begin{pmatrix} E_\rho \\ E_\phi \\ E_z \end{pmatrix} \quad (\text{A.40})$$

Note that we used the following convention for circular polarization: a wave is right-handed circularly polarized (RCP) if, with the right thumb oriented along the direction of propagation, the curling of one's fingers matches the direction of the temporal rotation of the field at a fixed point in space.

With circularly polarized transverse components, the field components are thus written as follows:

$$\vec{E} = \begin{pmatrix} E_{\text{RCP}} \\ E_{\text{LCP}} \\ E_z \end{pmatrix} = e^{-i\beta z} e^{i\omega t} \begin{cases} \begin{pmatrix} e^{i(\nu+1)\phi} \frac{i}{\kappa\sqrt{2}} (\beta A + k_0 B) J_{\nu+1}(\kappa\rho) \\ e^{i(\nu-1)\phi} \frac{-i}{\kappa\sqrt{2}} (\beta A - k_0 B) J_{\nu-1}(\kappa\rho) \\ e^{i\nu\phi} A J_\nu(\kappa\rho) \end{pmatrix} & \rho \leq a \\ \frac{J_\nu(a\kappa)}{K_\nu(a\gamma)} \begin{pmatrix} e^{i(\nu+1)\phi} \frac{-i}{\gamma\sqrt{2}} (\beta A + k_0 B) K_{\nu+1}(\gamma\rho) \\ e^{i(\nu-1)\phi} \frac{-i}{\gamma\sqrt{2}} (\beta A - k_0 B) K_{\nu-1}(\gamma\rho) \\ e^{i\nu\phi} A K_\nu(\gamma\rho) \end{pmatrix} & \rho > a \end{cases} \quad (\text{A.41})$$

$$\vec{H} = \begin{pmatrix} H_{\text{RCP}} \\ H_{\text{LCP}} \\ H_z \end{pmatrix} = e^{-i\beta z} e^{i\omega t} \begin{cases} \frac{i}{Z_0} \begin{pmatrix} e^{i(v+1)\phi} \frac{i}{\kappa\sqrt{2}} (k_0 u A + \beta B) J_{v+1}(\kappa\rho) \\ e^{i(v-1)\phi} \frac{i}{\kappa\sqrt{2}} (k_0 u A - \beta B) J_{v-1}(\kappa\rho) \\ e^{iv\phi} B J_v(\kappa\rho) \end{pmatrix} & \rho \leq a \\ \frac{J_v(a\kappa)}{K_v(a\gamma)} \frac{i}{Z_0} \begin{pmatrix} e^{i(v+1)\phi} \frac{-i}{\gamma\sqrt{2}} (k_0 v A + \beta B) K_{v+1}(\gamma\rho) \\ e^{i(v-1)\phi} \frac{i}{\gamma\sqrt{2}} (k_0 v A - \beta B) K_{v-1}(\gamma\rho) \\ e^{iv\phi} B K_v(\gamma\rho) \end{pmatrix} & \rho > a \end{cases} \quad (\text{A.42})$$

As a side note, for most modes the energy is predominantly concentrated in one of the two circular polarizations [74].

A.6 Normalization

When modes are used to simulate propagation or to convert transmission matrices to a fiber mode basis, the fields must first be normalized for the calculations to make sense. This means for example that the field \vec{E} as described by A.41 must be divided by its norm integral given below in A.43. The integral runs over the whole transverse plane. In other words, it is a polar integral over the surface $(\rho, \phi) \in [0, \infty] \times [0, 2\pi]$.

$$\int \|\vec{E}\|^2 dS = \int_{\phi=0}^{2\pi} \int_{\rho=0}^{\infty} \|\vec{E}(\rho, \phi, z)\|^2 \rho d\rho d\phi \quad (\text{A.43})$$

In Cartesian coordinates, the norm of a vector is obtained as the sum of the square magnitudes of the components. However, since the circularly polarized or cylindrical components are orthogonal as well, the norm can be calculated in the same way in each representation:

$$\|\vec{E}\|^2 = |E_x|^2 + |E_y|^2 + |E_z|^2 = |E_{\text{RCP}}|^2 + |E_{\text{LCP}}|^2 + |E_z|^2 = |E_\rho|^2 + |E_\phi|^2 + |E_z|^2 \quad (\text{A.44})$$

Substituting the field components of A.41 (and assuming real parameters), we obtain the following expression for the norm $\|\vec{E}\|^2$:

$$\|\vec{E}\|^2 = \begin{cases} \frac{1}{2\kappa^2} |\beta A + k_0 B|^2 J_{v+1}(\kappa\rho)^2 + \frac{1}{2\kappa^2} |\beta A - k_0 B|^2 J_{v-1}(\kappa\rho)^2 + |A|^2 J_v(\kappa\rho)^2 & \rho \leq a \\ \left(\frac{J_v(a\kappa)}{K_v(a\gamma)} \right)^2 \left(\frac{1}{2\gamma^2} |\beta A + k_0 B|^2 K_{v+1}(\gamma\rho)^2 + \frac{1}{2\gamma^2} |\beta A - k_0 B|^2 K_{v-1}(\gamma\rho)^2 + |A|^2 K_v(\gamma\rho)^2 \right) & \rho > a \end{cases} \quad (\text{A.45})$$

The norm can finally be calculated by evaluating the integral A.43 over the transverse plane while substituting Equation A.45. The norm integral can be solved analytically by using the

following identities:

$$\int_0^{\rho_0} \rho J_\nu(\rho)^2 d\rho = \frac{1}{2} \rho_0 (\rho_0 J_{\nu-1}(\rho)^2 - 2\nu J_{\nu-1}(\rho) J_\nu(\rho) + \rho_0 J_\nu(\rho)^2) \quad (\text{A.46})$$

$$\int_{\rho_0}^{+\infty} \rho K_\nu(\rho)^2 d\rho = \frac{1}{2} \rho_0 (\rho_0 K_{\nu-1}(\rho)^2 + 2\nu K_{\nu-1}(\rho) K_\nu(\rho) - \rho_0 K_\nu(\rho)^2) \quad (\text{A.47})$$

A.7 Numerical procedure

To calculate the modes of a step-index fiber in software, the following procedure can be used:

1. Determine all the intervals where $a\kappa$ can have a solution, as explained at the end of section A.3.
2. Use a root-finding algorithm to determine the solutions $a\kappa$ of each equation of A.30 inside each interval found in step 1. For the root-solving procedure, make sure to replace γ and β in A.30 by their equivalent in terms of $a\kappa$ using A.16.
3. Calculate the amplitude coefficients using A.35.
4. Normalize the amplitude coefficients by dividing them with the square root of the norm, calculated as explained in section A.6.
5. Calculate the field values over a grid of spatial positions, e.g. using a circular polarization with formulas A.41 and A.42.

In each of these steps, problems can occur due to the modified Bessel function $K_\nu(a\gamma)$. Because of the exponential nature of this function, it can quickly exceed the range of representable values of floating-point numbers on a typical computer. This happens both for $\gamma \rightarrow 0$ (overflow) as well as for $\gamma \rightarrow \infty$ (underflow), and occurs more readily when the order ν becomes large (i.e. for fiber with many modes, such as fibers with a large core or numerical aperture). For this reason, it is recommended to use a variable precision solver in step 2 (e.g. the “vpa” toolbox in MATLAB), and to check for problematic values of K_ν before proceeding to the next steps. The simulations in the main text relied on a custom numerical class for the subsequent steps, allowing the exponent to span a much wider range than standard floating-point values without the overhead of a full variable precision class.

When the propagation constants are found in step 2, it is recommended to verify them by inserting them again in the characteristic equation A.29 in order to check for errors and numerical accuracy. Indeed, the condition number of this problem can be high, particularly for modes near cutoff.

Examples of mode solutions can be found in Figure A.3 and Table A.1.

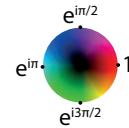
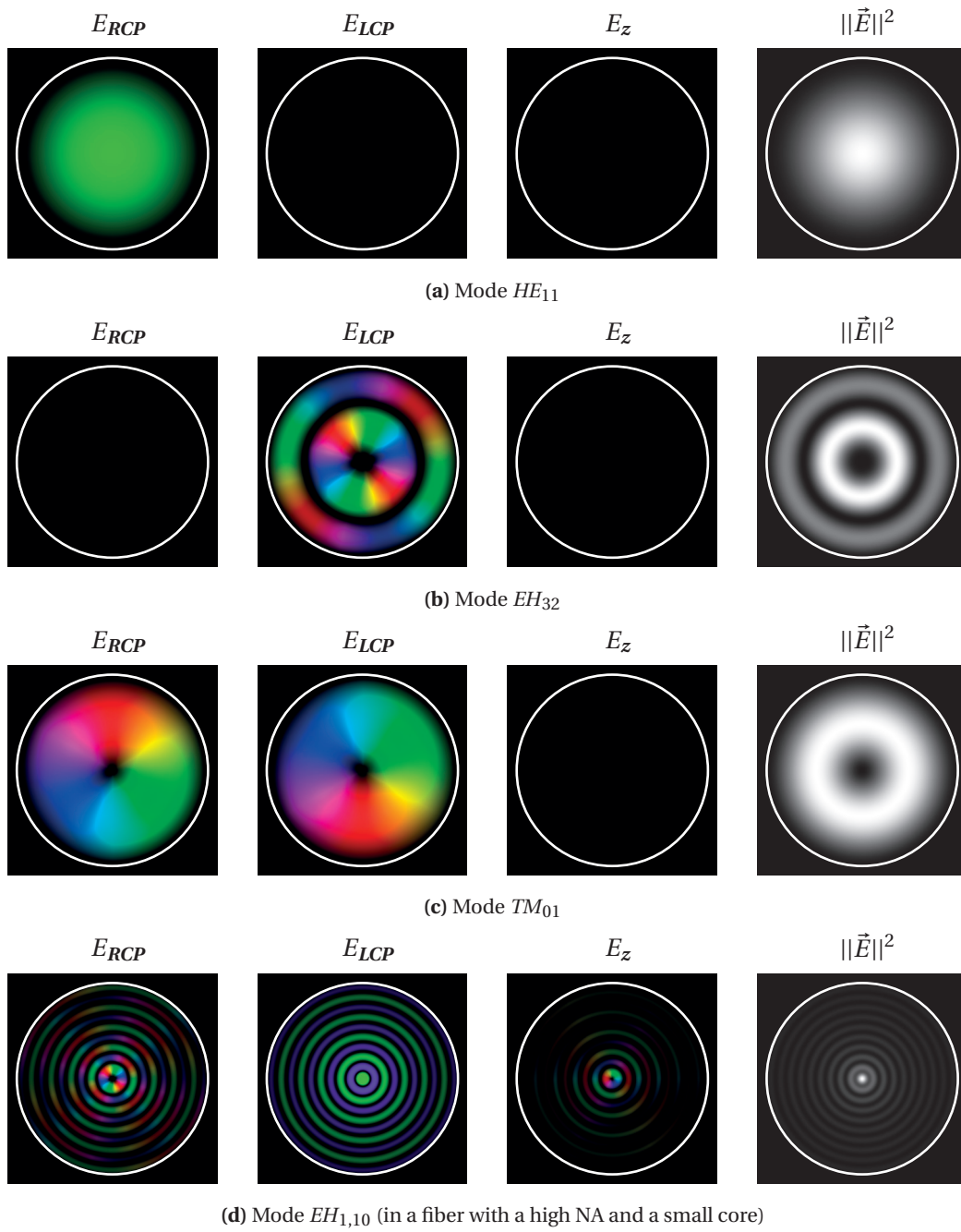


Figure A.3: Field components (circularly polarized representation) for various fiber modes. See Table A.1 for the parameters of each mode. The fiber core is indicated with a white circle.

A.7. Numerical procedure

Mode	HE_{11}	EH_{32}	TM_{01}	$EH_{1,10}$
Fiber parameters				
\mathcal{O}_{core}	105 μm	105 μm	105 μm	10 μm
NA	0.22	0.22	0.22	1.06
n_{core}	1.4607	1.4607	1.4607	1.4607
n_{clad}	1.4440	1.4440	1.4440	1.0000
Wavelength				
λ	532 nm	532 nm	532 nm	532 nm
Solution parameters				
ν	-1	3	0	1
Equation (A.30)	LHS_-	LHS_-	LHS_-	LHS_-
Interval	$(0, j_{1,1})$	$(j_{3,1}, j_{3,2})$	$(j_{0,1}, j_{0,2})$	$(j_{1,9}, j_{1,10})$
Propagation constant				
β	$17.3 \times 10^6 \text{m}^{-1}$	$17.3 \times 10^6 \text{m}^{-1}$	$17.3 \times 10^6 \text{m}^{-1}$	$16.1 \times 10^6 \text{m}^{-1}$
κa	2.387 521	8.356 654	3.804 443	30.352 647
γa	136.390 365	136.155 052	136.358 198	55.063 223
Amplitude coefficients				
A	38.3	257	111	2.70×10^5
B	55.9	-374	0	-5.27×10^4

Table A.1: Propagation constants and amplitude coefficients for various modes. These modes are also illustrated in Figure A.3.

Bibliography

- [1] Jeff Hecht. *City of Light: The Story of Fiber Optics*. Oxford University Press, 2004. Google-Books-ID: 4oMu7RbGpqUC.
- [2] Roman Barankov and Jerome Mertz. High-throughput imaging of self-luminous objects through a single optical fibre. *Nature Communications*, 5, November 2014.
- [3] Sylwia M. Kolenderska, Ori Katz, Mathias Fink, and Sylvain Gigan. Scanning-free imaging through a single fiber by random spatio-spectral encoding. *Optics Letters*, 40(4):534–537, February 2015.
- [4] Fritjof Helmchen and Winfried Denk. Deep tissue two-photon microscopy. *Nature Methods*, 2(12):932–940, December 2005.
- [5] David Huang, Eric A. Swanson, Charles P. Lin, Joel S. Schuman, William G. Stinson, Warren Chang, Michael R. Hee, Thomas Flotte, Kenton Gregory, Carmen A. Puliafito, and James G. Fujimoto. Optical Coherence Tomography. *Science (New York, N.Y.)*, 254(5035):1178–1181, November 1991.
- [6] Sungsam Kang, Seungwon Jeong, Wonjun Choi, Hakseok Ko, Taeseok D. Yang, Jang Ho Joo, Jae-Seung Lee, Yong-Sik Lim, Q.-Han Park, and Wonshik Choi. Imaging deep within a scattering medium using collective accumulation of single-scattered waves. *Nature Photonics*, advance online publication, March 2015.
- [7] Jae-Ho Han, Junghoon Lee, and Jin U. Kang. Pixelation effect removal from fiber bundle probe based optical coherence tomography imaging. *Optics Express*, 18(7):7427–7439, March 2010.
- [8] Simon Peter Mekhail, Gordon Arbuthnott, and Sile Nic Chormaic. Advances in Fibre Microendoscopy for Neuronal Imaging. *Optical Data Processing and Storage*, 2(1), January 2016.
- [9] Peter Delaney and Martin Harris. Fiber-Optics in Scanning Optical Microscopy. In *Handbook of Biological Confocal Microscopy*, pages 508–515. Springer US, New York, USA, 3 edition, 2006.
- [10] Mauna Kea Technologies. Cellvizio® Lab Technical Sheet, June 2014.

Bibliography

- [11] M. C. W. van Rossum and Th. M. Nieuwenhuizen. Multiple scattering of classical waves: microscopy, mesoscopy, and diffusion. *Reviews of Modern Physics*, 71(1):313–371, January 1999.
- [12] W. F. Cheong, S. A. Prah, and A. J. Welch. A review of the optical properties of biological tissues. *IEEE Journal of Quantum Electronics*, 26(12):2166–2185, December 1990.
- [13] Emmett N. Leith and Juris Upatnieks. Holographic Imagery Through Diffusing Media. *JOSA*, 56(4):523–523, April 1966.
- [14] H. Kogelnik. Holographic Image Projection through Inhomogeneous Media. *Bell System Technical Journal*, 44(10):2451–2455, December 1965.
- [15] I. M. Vellekoop and A. P. Mosk. Focusing coherent light through opaque strongly scattering media. *Optics Letters*, 32(16):2309–2311, August 2007.
- [16] Meng Cui and Changhui Yang. Implementation of a digital optical phase conjugation system and its application to study the robustness of turbidity suppression by phase conjugation. *Optics Express*, 18(4):3444–3455, February 2010.
- [17] Myung K. Kim. Principles and techniques of digital holographic microscopy. *Journal of Photonics for Energy*, pages 018005–018005–50, 2010.
- [18] S. M. Popoff, G. Lerosey, R. Carminati, M. Fink, A. C. Boccara, and S. Gigan. Measuring the Transmission Matrix in Optics: An Approach to the Study and Control of Light Propagation in Disordered Media. *Physical Review Letters*, 104(10):100601, March 2010.
- [19] Sébastien Popoff, Geoffroy Lerosey, Mathias Fink, Albert Claude Boccara, and Sylvain Gigan. Image transmission through an opaque material. *Nature Communications*, 1:81, September 2010.
- [20] S. M. Popoff, G. Lerosey, M. Fink, A. C. Boccara, and S. Gigan. Controlling light through optical disordered media: transmission matrix approach. *New Journal of Physics*, 13(12):123021, December 2011.
- [21] Kevin T. Takasaki and Jason W. Fleischer. Phase-space measurement for depth-resolved memory-effect imaging. *Optics Express*, 22(25):31426–31433, December 2014.
- [22] Benjamin Judkewitz, Roarke Horstmeyer, Ivo M. Vellekoop, Ioannis N. Papadopoulos, and Changhui Yang. Translation correlations in anisotropically scattering media. *Nature Physics*, 11(8):684–689, August 2015.
- [23] Sam Schott, Jacopo Bertolotti, Jean-Francois Léger, Laurent Bourdieu, and Sylvain Gigan. Characterization of the angular memory effect of scattered light in biological tissues. *Optics Express*, 23(10):13505, May 2015.

-
- [24] Moonseok Kim, Youngwoon Choi, Changhyeong Yoon, Wonjun Choi, Kim Jaisoon, Q.-Han Park, and Wonshik Choi. Maximal energy transport through disordered media with the implementation of transmission eigenchannels. *Nature Photonics*, 6(9):581–585, September 2012.
- [25] Curtis Jin, Raj Rao Nadakuditi, Eric Michielssen, and Stephen C. Rand. Backscatter analysis based algorithms for increasing transmission through highly scattering random media using phase-only-modulated wavefronts. *Journal of the Optical Society of America A*, 31(8):1788–1800, August 2014.
- [26] Wonjun Choi, Moonseok Kim, Donggyu Kim, Changhyeong Yoon, Christopher Fang-Yen, Q.-Han Park, and Wonshik Choi. Preferential coupling of an incident wave to reflection eigenchannels of disordered media. *Scientific Reports*, 5, June 2015.
- [27] Raktim Sarma, Alexey Yamilov, and Hui Cao. Enhancing light transmission through a disordered waveguide with inhomogeneous scattering and loss. *Applied Physics Letters*, 110(2):021103, January 2017.
- [28] Walter Harm, Clemens Roeder, Alexander Jesacher, Stefan Bernet, and Monika Ritsch-Marte. Lensless imaging through thin diffusive media. *Optics Express*, 22(18):22146–22156, September 2014.
- [29] Allard P. Mosk, Ad Lagendijk, Geoffroy Lerosey, and Mathias Fink. Controlling waves in space and time for imaging and focusing in complex media. *Nature Photonics*, 6(5):283–292, May 2012.
- [30] Ivo M. Vellekoop. Feedback-based wavefront shaping. *Optics Express*, 23(9):12189, May 2015.
- [31] Hyeonseung Yu, Jongchan Park, KyeoReh Lee, Jonghee Yoon, KyungDuk Kim, Shinwha Lee, and YongKeun Park. Recent advances in wavefront shaping techniques for biomedical applications. *Current Applied Physics*, 15(5):632–641, May 2015.
- [32] Jacopo Bertolotti, Elbert G. van Putten, Christian Blum, Ad Lagendijk, Willem L. Vos, and Allard P. Mosk. Non-invasive imaging through opaque scattering layers. *Nature*, 491(7423):232–234, November 2012.
- [33] Roarke Horstmeyer, Haowen Ruan, and Changhuei Yang. Guidestar-assisted wavefront-shaping methods for focusing light into biological tissue. *Nature Photonics*, 9(9):563–571, September 2015.
- [34] Xiao Xu, Honglin Liu, and Lihong V. Wang. Time-reversed ultrasonically encoded optical focusing into scattering media. *Nature Photonics*, 5(3):154–157, March 2011.
- [35] T. Chaigne, O. Katz, A. C. Boccara, M. Fink, E. Bossy, and S. Gigan. Controlling light in scattering media non-invasively using the photoacoustic transmission matrix. *Nature Photonics*, advance online publication, November 2013.

Bibliography

- [36] Benjamin Judkewitz, Ying Min Wang, Roarke Horstmeyer, Alexandre Mathy, and Changhuei Yang. Speckle-scale focusing in the diffusive regime with time reversal of variance-encoded light (TROVE). *Nature Photonics*, 7(4):300–305, April 2013.
- [37] Emmanuel Bossy and Sylvain Gigan. Photoacoustics with coherent light. *Photoacoustics*, 4(1):22–35, March 2016.
- [38] Ori Katz, Eran Small, Yefeng Guan, and Yaron Silberberg. Noninvasive nonlinear focusing and imaging through strongly scattering turbid layers. *Optica*, 1(3):170–174, September 2014.
- [39] Ioannis N. Papadopoulos, Jean-Sébastien Jouhannau, James F. A. Poulet, and Benjamin Judkewitz. Scattering compensation by focus scanning holographic aberration probing (F-SHARP). *Nature Photonics*, 11(2):116–123, February 2017.
- [40] Erich Spitz and Alain Werts. Transmission des images à travers une fibre optique. *Comptes rendus hebdomadaires des séances de l'Académie des sciences, série B.*, 264(4):1015–1018, March 1967.
- [41] Gilmore J. Dunning and R. C. Lind. Demonstration of image transmission through fibers by optical phase conjugation. *Optics Letters*, 7(11):558–560, November 1982.
- [42] Baruch Fischer and Shmuel Sternklar. Image transmission and interferometry with multimode fibers using self-pumped phase conjugation. *Applied Physics Letters*, 46(2):113–114, January 1985.
- [43] Paul H. Beckwith, Ian McMichael, and Pochi Yeh. Image distortion in multimode fibers and restoration by polarization-preserving phase conjugation. *Optics Letters*, 12(7):510–512, July 1987.
- [44] Yasuo Tomita, Ram Yahalom, and Amnon Yariv. Theory of polarization and spatial information recovery by modal dispersal and phase conjugation. *JOSA B*, 5(3):690–700, March 1988.
- [45] A. Volyar, A. Gnatovskii, N. Kukhtarev, and S. Lapaeva. Image transmission via a multimode fiber assisted by polarization preserving phase conjugation in the photorefractive crystal. *Applied Physics B*, 52(6):400–401, 1991.
- [46] Amnon Yariv. On transmission and recovery of three-dimensional image information in optical waveguides. *Journal of the Optical Society of America*, 66(4):301–306, April 1976.
- [47] Amnon Yariv. Three-dimensional pictorial transmission in optical fibers. *Applied Physics Letters*, 28(2):88–89, January 1976.
- [48] AA Friesem, U. Levy, and Y. Silberberg. Parallel transmission of images through single optical fibers. *Proceedings of the IEEE*, 71(2):208–221, February 1983.

-
- [49] Takeshi Ogasawara, Masahiro Ohno, Koichi Karaki, Koichi Nishizawa, and Atsushi Akiba. Image transmission with a pair of graded-index optical fibers and a BaTiO₃ phase-conjugate mirror. *JOSA B*, 13(10):2193–2197, October 1996.
- [50] A. Gover, C. P. Lee, and A. Yariv. Direct transmission of pictorial information in multimode optical fibers. *Journal of the Optical Society of America*, 66(4):306–311, April 1976.
- [51] Masaki Fukui and Ken-ichi Kitayama. Real-time restoration method for image transmission in a multimode optical fiber. *Optics Letters*, 15(17):977–979, September 1990.
- [52] C. Y. Wu, A. R. D. Somervell, and T. H. Barnes. Direct image transmission through a multi-mode square optical fiber. *Optics Communications*, 157(1–6):17–22, December 1998.
- [53] Jung-Young Son, Vladimir I. Bobrinev, Hyung-Wook Jeon, Young-Hyun Cho, and Yong-Sik Eom. Direct image transmission through a multimode optical fiber. *Applied Optics*, 35(2):273–277, January 1996.
- [54] Maxim A. Bolshtyansky and Boris Ya. Zel'dovich. Transmission of the image signal with the use of a multimode fiber. *Optics Communications*, 123(4–6):629–636, February 1996.
- [55] Roberto Di Leonardo and Silvio Bianchi. Hologram transmission through multi-mode optical fibers. *Optics Express*, 19(1):247–254, January 2011.
- [56] Reza Nasiri Mahalati, Daulet Askarov, Jeffrey P. Wilde, and Joseph M. Kahn. Adaptive control of input field to achieve desired output intensity profile in multimode fiber with random mode coupling. *Optics express*, 20(13):14321–14337, 2012.
- [57] Tomáš Čižmár and Kishan Dholakia. Shaping the light transmission through a multimode optical fibre: complex transformation analysis and applications in biophotonics. *Optics Express*, 19(20):18871–18884, September 2011.
- [58] Alex J. Thompson, Carl Paterson, Mark AA Neil, Chris Dunsby, and Paul MW French. Adaptive phase compensation for ultracompact laser scanning endomicroscopy. *Optics letters*, 36(9):1707–1709, 2011.
- [59] Ioannis N. Papadopoulos, Salma Farahi, Christophe Moser, and Demetri Psaltis. Focusing and scanning light through a multimode optical fiber using digital phase conjugation. *Optics Express*, 20(10):10583–10590, May 2012.
- [60] Ioannis N. Papadopoulos, Salma Farahi, Christophe Moser, and Demetri Psaltis. High-resolution, lensless endoscope based on digital scanning through a multimode optical fiber. *Biomedical Optics Express*, 4(2):260–270, February 2013.
- [61] Silvio Bianchi and Roberto Di Leonardo. A multi-mode fiber probe for holographic micromanipulation and microscopy. *Lab on a Chip*, 12(3):635–639, January 2012.

Bibliography

- [62] Tomáš Čižmár and Kishan Dholakia. Exploiting multimode waveguides for pure fibre-based imaging. *Nature Communications*, 3:1027, August 2012.
- [63] Changhyeong Yoon, Youngwoon Choi, Moonseok Kim, Junggho Moon, Donggyu Kim, and Wonshik Choi. Experimental measurement of the number of modes for a multimode optical fiber. *Optics Letters*, 37(21):4558–4560, November 2012.
- [64] Donggyu Kim, Junggho Moon, Moonseok Kim, Taeseok Daniel Yang, Jaisoon Kim, Euiheon Chung, and Wonshik Choi. Toward a miniature endomicroscope: pixelation-free and diffraction-limited imaging through a fiber bundle. *Optics Letters*, 39(7):1921–1924, April 2014.
- [65] Antonio M. Caravaca-Aguirre and Rafael Piestun. Single multimode fiber endoscope. *Optics Express*, 25(3):1656, February 2017.
- [66] Nicolino Stasio, Atsushi Shibukawa, Ioannis N. Papadopoulos, Salma Farahi, Olivier Simandoux, Jean-Pierre Huignard, Emmanuel Bossy, Christophe Moser, and Demetri Psaltis. Towards new applications using capillary waveguides. *Biomedical Optics Express*, 6(12):4619, December 2015.
- [67] Nicolino Stasio, Christophe Moser, and Demetri Psaltis. Calibration-free imaging through a multicore fiber using speckle scanning microscopy. *Optics Letters*, 41(13):3078, July 2016.
- [68] Martin Plöschner, Věra Kollárová, Zbyněk Dostál, Jonathan Nylk, Thomas Barton-Owen, David E. K. Ferrier, Radim Chmelík, Kishan Dholakia, and Tomáš Čižmár. Multimode fibre: Light-sheet microscopy at the tip of a needle. *Scientific Reports*, 5:18050, December 2015.
- [69] Gregoire. P. J. Laporte, Nicolino Stasio, Christophe Moser, and Demetri Psaltis. Enhanced resolution in a multimode fiber imaging system. *Optics Express*, 23(21):27484, October 2015.
- [70] Edgar E. Morales Delgado, Demetri Psaltis, and Christophe Moser. Two-photon imaging through a multimode fiber. *Optics Express*, 23(25):32158, December 2015.
- [71] Donald B. Conkey, Nicolino Stasio, Edgar E. Morales Delgado, Marilisa Romito, Christophe Moser, and Demetri Psaltis. Lensless two-photon imaging through a multicore fiber with coherence-gated digital phase conjugation. *Journal of Biomedical Optics*, 21(4):045002–045002, 2016.
- [72] Siddharth Sivankutty, Esben Ravn Andresen, Rosa Cossart, Géraud Bouwmans, Serge Monneret, and Hervé Rigneault. Ultra-thin rigid endoscope: two-photon imaging through a graded-index multi-mode fiber. *Optics Express*, 24(2):825, January 2016.
- [73] Reza Nasiri Mahalati, Ruo Yu Gu, and Joseph M. Kahn. Resolution limits for imaging through multi-mode fiber. *Optics Express*, 21(2):1656–1668, January 2013.

- [74] Martin Plöschner, Tomáš Tyc, and Tomáš Čižmár. Seeing through chaos in multimode fibres. *Nature Photonics*, 9(8):529–535, August 2015.
- [75] G.S.D. Gordon, J. Joseph, S. Bohndiek, and T.D. Wilkinson. Single-pixel phase-corrected fiber bundle endomicroscopy with lensless focussing capability. *Journal of Lightwave Technology*, PP(99):1–1, 2015.
- [76] Damien Loterie, Sebastianus A. Goorden, Demetri Psaltis, and Christophe Moser. Confocal microscopy through a multimode fiber using optical correlation. *Optics Letters*, 40(24):5754–5757, December 2015.
- [77] Damien Loterie, Salma Farahi, Ioannis Papadopoulos, Alexandre Goy, Demetri Psaltis, and Christophe Moser. Digital confocal microscopy through a multimode fiber. *Optics Express*, 23(18):23845–23858, September 2015.
- [78] Youngwoon Choi, Changhyeong Yoon, Moonseok Kim, Taeseok Daniel Yang, Christopher Fang-Yen, Ramachandra R. Dasari, Kyoung Jin Lee, and Wonshik Choi. Scanner-free and wide-field endoscopic imaging by using a single multimode optical fiber. *Physical Review Letters*, 109(20):203901, November 2012.
- [79] Esben Ravn Andresen, Géraud Bouwmans, Serge Monneret, and Hervé Rigneault. Toward endoscopes with no distal optics: video-rate scanning microscopy through a fiber bundle. *Optics Letters*, 38(5):609–611, March 2013.
- [80] Siddharth Sivankutty, Viktor Tsvirkun, Géraud Bouwmans, Dani Kogan, Dan Oron, Esben Ravn Andresen, and Hervé Rigneault. Extended field-of-view in a lensless endoscope using an aperiodic multicore fiber. *Optics Letters*, 41(15):3531, August 2016.
- [81] Ioannis N. Papadopoulos, Olivier Simandoux, Salma Farahi, Jean Pierre Huignard, Emmanuel Bossy, Demetri Psaltis, and Christophe Moser. Optical-resolution photoacoustic microscopy by use of a multimode fiber. *Applied Physics Letters*, 102(21):211106, May 2013.
- [82] Hwanchol Jang, Changhyeong Yoon, Euiheon Chung, Wonshik Choi, and Heung-No Lee. Holistic random encoding for imaging through multimode fibers. *Optics Express*, 23(5):6705–6721, March 2015.
- [83] Ryosuke Takagi, Ryoichi Horisaki, and Jun Tanida. Object recognition through a multimode fiber. *Optical Review*, pages 1–4, February 2017.
- [84] Amir Porat, Esben Ravn Andresen, Hervé Rigneault, Dan Oron, Sylvain Gigan, and Ori Katz. Widefield lensless imaging through a fiber bundle via speckle correlations. *Optics Express*, 24(15):16835–16855, July 2016.
- [85] Viktor Tsvirkun, Siddharth Sivankutty, Géraud Bouwmans, Ori Katz, Esben Ravn Andresen, and Hervé Rigneault. Widefield lensless endoscopy with a multicore fiber. *Optics Letters*, 41(20):4771, October 2016.

Bibliography

- [86] Salma Farahi, David Ziegler, Ioannis N. Papadopoulos, Demetri Psaltis, and Christophe Moser. Dynamic bending compensation while focusing through a multimode fiber. *Optics Express*, 21(19):22504–22514, September 2013.
- [87] Nicolino Stasio, Donald B. Conkey, Christophe Moser, and Demetri Psaltis. Light control in a multicore fiber using the memory effect. *Optics Express*, 23(23):30532, November 2015.
- [88] Sean C. Warren, Youngchan Kim, James M. Stone, Claire Mitchell, Jonathan C. Knight, Mark A. A. Neil, Carl Paterson, Paul M. W. French, and Chris Dunsby. Adaptive multi-photon endomicroscopy through a dynamically deformed multicore optical fiber using proximal detection. *Optics Express*, 24(19):21474, September 2016.
- [89] Ruo Yu Gu, Reza Nasiri Mahalati, and Joseph M. Kahn. Design of flexible multi-mode fiber endoscope. *Optics Express*, 23(21):26905, October 2015.
- [90] Antonio M. Caravaca-Aguirre, Eyal Niv, Donald B. Conkey, and Rafael Piestun. Real-time resilient focusing through a bending multimode fiber. *Optics Express*, 21(10):12881–12887, May 2013.
- [91] Shamir Rosen, Doron Gilboa, Ori Katz, and Yaron Silberberg. Focusing and Scanning through Flexible Multimode Fibers without Access to the Distal End. *arXiv:1506.08586 [physics]*, June 2015. arXiv: 1506.08586.
- [92] M. Plöschner, B. Straka, K. Dholakia, and T. Čižmár. GPU accelerated toolbox for real-time beam-shaping in multimode fibres. *Optics Express*, 22(3):2933–2947, February 2014.
- [93] Martin Plöschner and Tomáš Cizmár. Compact multimode fiber beam-shaping system based on GPU accelerated digital holography. *Optics Letters*, 40(2):197–200, January 2015.
- [94] Adrien Descloux, Lyubov V. Amitonova, and Pepijn W. H. Pinkse. Aberrations of the point spread function of a multimode fiber. *arXiv:1606.05436 [physics]*, June 2016. arXiv: 1606.05436.
- [95] Wen Xiong, Philipp Ambichl, Yaron Bromberg, Brandon Redding, Stefan Rotter, and Hui Cao. Principal modes in multimode fibers: exploring the crossover from weak to strong mode coupling. *Optics Express*, 25(3):2709–2724, February 2017.
- [96] Wen Xiong, Philipp Ambichl, Yaron Bromberg, Brandon Redding, Stefan Rotter, and Hui Cao. Spatiotemporal Control of Light Transmission through a Multimode Fiber with Strong Mode Coupling. *Physical Review Letters*, 117(5):053901, July 2016.
- [97] Joel Carpenter, Benjamin J. Eggleton, and Jochen Schröder. Observation of Eisenbud–Wigner–Smith states as principal modes in multimode fibre. *Nature Photonics*, advance online publication, October 2015.

-
- [98] Joel Carpenter, Benjamin J. Eggleton, and Jochen Schröder. Comparison of principal modes and spatial eigenmodes in multimode optical fibre. *Laser & Photonics Reviews*, 11(1):n/a–n/a, January 2017.
- [99] Joel Carpenter, Benjamin J. Eggleton, and Jochen Schröder. Complete spatiotemporal characterization and optical transfer matrix inversion of a 420 mode fiber. *Optics Letters*, 41(23):5580, December 2016.
- [100] J. Carpenter, B. C. Thomsen, and T. D. Wilkinson. Degenerate Mode-Group Division Multiplexing. *Journal of Lightwave Technology*, 30(24):3946–3952, December 2012.
- [101] Seng Fatt Liew, Brandon Redding, Michael A. Choma, Hemant D. Tagare, and Hui Cao. Broadband multimode fiber spectrometer. *Optics Letters*, 41(9):2029, May 2016.
- [102] Brandon Redding, Sebastien M. Popoff, and Hui Cao. All-fiber spectrometer based on speckle pattern reconstruction. *Optics express*, 21(5):6584–6600, 2013.
- [103] Brandon Redding, Seng Fatt Liew, Yaron Bromberg, Raktim Sarma, and Hui Cao. Evanescently coupled multimode spiral spectrometer. *Optica*, 3(9):956, September 2016.
- [104] Edgar E. Morales Delgado, Salma Farahi, Ioannis N. Papadopoulos, Demetri Psaltis, and Christophe Moser. Delivery of focused short pulses through a multimode fiber. *Optics Express*, 23(7):9109, April 2015.
- [105] Lyubov V. Amitonova, Adrien Descloux, Joerg Petschulat, Michael H. Frosz, Goran Ahmed, Fehim Babic, Xin Jiang, Allard P. Mosk, Philip St.J. Russell, and Pepijn W. H. Pinkse. High-resolution wavefront shaping with a photonic crystal fiber for multimode fiber imaging. *Optics Letters*, 41(3):497, February 2016.
- [106] S. Bianchi, V. P. Rajamanickam, L. Ferrara, E. Di Fabrizio, C. Liberale, and R. Di Leonardo. Focusing and imaging with increased numerical apertures through multimode fibers with micro-fabricated optics. *Optics Letters*, 38(23):4935–4938, December 2013.
- [107] Ioannis N. Papadopoulos, Salma Farahi, Christophe Moser, and Demetri Psaltis. Increasing the imaging capabilities of multimode fibers by exploiting the properties of highly scattering media. *Optics Letters*, 38(15):2776–2778, August 2013.
- [108] Lyubov V. Amitonova, Allard P. Mosk, and Pepijn W. H. Pinkse. The rotational memory effect of a multimode fiber. *Optics Express*, 23(16):20569, August 2015.
- [109] Damien Loterie, Salma Farahi, Demetri Psaltis, and Christophe Moser. Complex pattern projection through a multimode fiber. In *Adaptive Optics and Wavefront Control for Biological Systems*, volume 9335, pages 93350I–1 to –6, 2015.
- [110] Zhe Yin, Guodong Liu, Fengdong Chen, and Bingguo Liu. Fast-forming focused spots through a multimode fiber based on an adaptive parallel coordinate algorithm. *Chinese Optics Letters*, 13(7):071404, July 2015.

Bibliography

- [111] Joel Carpenter, Benjamin J. Eggleton, and Jochen Schröder. 110x110 optical mode transfer matrix inversion. *Optics Express*, 22(1):96–101, January 2014.
- [112] Bienvenu Ndagano, Robert Brüning, Melanie McLaren, Michael Duparré, and Andrew Forbes. Fiber propagation of vector modes. *Optics Express*, 23(13):17330, June 2015.
- [113] Joel A. Carpenter, Benjamin J. Eggleton, and Jochen Schroeder. Maximally efficient imaging through multimode fiber. In *CLEO: 2014*, OSA Technical Digest (online), page STh1H.3. Optical Society of America, June 2014.
- [114] Ioannis Papadopoulos. *Dynamic control of light transmission through multimode fibers*. PhD thesis, EPFL, Lausanne, February 2014.
- [115] Emmett N. Leith and Juris Upatnieks. Reconstructed wavefronts and communication theory. *JOSA*, 52(10):1123–1130, 1962.
- [116] Joseph W Goodman. *Introduction to Fourier optics*. Roberts & Co., Englewood, Colo., 2005.
- [117] Alan V. Oppenheim and Alan S. Willsky. The Effect of Undersampling: Aliasing. In *Signals and Systems*, pages 527–534. Prentice Hall, Englewood Cliffs, N.J, 1st edition edition, June 1982.
- [118] Zichen Zhang, Zheng You, and Daping Chu. Fundamentals of phase-only liquid crystal on silicon (LCOS) devices. *Light: Science & Applications*, 3(10):e213, October 2014.
- [119] Philip Zupancic, Philipp M. Preiss, Ruichao Ma, Alexander Lukin, M. Eric Tai, Matthew Rispoli, Rajibul Islam, and Markus Greiner. Ultra-precise holographic beam shaping for microscopic quantum control. *Optics Express*, 24(13):13881, June 2016.
- [120] Wai-Hon Lee. Computer-Generated Holograms: Techniques and Applications. In E. Wolf, editor, *Progress in Optics*, volume 16, pages 119–232. Elsevier, 1978. DOI: 10.1016/S0079-6638(08)70072-6.
- [121] Santosh Tripathi and Kimani C. Toussaint. Quantitative control over the intensity and phase of light transmitted through highly scattering media. *Optics Express*, 21(22):25890–25900, November 2013.
- [122] Kevin J. Mitchell, Sergey Turtaev, Miles J. Padgett, Tomáš Čižmár, and David B. Phillips. High-speed spatial control of the intensity, phase and polarisation of vector beams using a digital micro-mirror device. *Optics Express*, 24(25):29269, December 2016.
- [123] Erdem Ulusoy, Levent Onural, and Haldun M. Ozaktas. Full-complex amplitude modulation with binary spatial light modulators. *Journal of the Optical Society of America A*, 28(11):2310–2321, November 2011.

- [124] Sebastianus A. Goorden, Jacopo Bertolotti, and Allard P. Mosk. Superpixel-based spatial amplitude and phase modulation using a digital micromirror device. *arXiv:1405.3893 [physics]*, May 2014.
- [125] Jorge García-Márquez, Victor López, Arturo González-Vega, and Enrique Noé. Flicker minimization in an LCoS spatial light modulator. *Optics Express*, 20(8):8431–8441, April 2012.
- [126] DirectX 11 Tutorials, July 2011. <http://rastertek.com/tutdx11.html>.
- [127] Alain Bergeron, Jonny Gauvin, François Gagnon, Denis Gingras, Henri H. Arsenault, and Michel Doucet. Phase calibration and applications of a liquid-crystal spatial light modulator. *Applied Optics*, 34(23):5133–5139, August 1995.
- [128] Pedro M. Prieto, Enrique J. Fernández, Silvestre Manzanera, and Pablo Artal. Adaptive optics with a programmable phase modulator: applications in the human eye. *Optics Express*, 12(17):4059–4071, August 2004.
- [129] Omel Mendoza-Yero, Gladys Mínguez-Vega, Lluís Martínez-León, Miguel Carbonell-Leal, Mercedes Fernández-Alonso, Carlos Doñate-Buendía, Jorge Pérez-Vizcaíno, and Jesús Lancis. Diffraction-Based Phase Calibration of Spatial Light Modulators With Binary Phase Fresnel Lenses. *Journal of Display Technology*, 12(10):1027–1032, October 2016.
- [130] Stephan Reichelt. Spatially resolved phase-response calibration of liquid-crystal-based spatial light modulators. *Applied Optics*, 52(12):2610–2618, April 2013.
- [131] David Engström, Martin Persson, Jörgen Bengtsson, and Mattias Goksör. Calibration of spatial light modulators suffering from spatially varying phase response. *Optics Express*, 21(13):16086–16103, July 2013.
- [132] Tobias Haist, Christian Lingel, Rodolfo Adler, and Wolfgang Osten. Parallelized genetic optimization of spatial light modulator addressing for diffractive applications. *Applied Optics*, 53(7):1413–1418, March 2014.
- [133] José Luis Martínez Fuentes, Enrique J. Fernández, Pedro M. Prieto, and Pablo Artal. Interferometric method for phase calibration in liquid crystal spatial light modulators using a self-generated diffraction-grating. *Optics Express*, 24(13):14159–14171, June 2016.
- [134] Xiaodong Xun and Robert W. Cohn. Phase calibration of spatially nonuniform spatial light modulators. *Applied Optics*, 43(35):6400–6406, December 2004.
- [135] Joaquín Otón, Pierre Ambs, María S. Millán, and Elisabet Pérez-Cabré. Multipoint phase calibration for improved compensation of inherent wavefront distortion in parallel aligned liquid crystal on silicon displays. *Applied Optics*, 46(23):5667–5679, August 2007.

Bibliography

- [136] Long Teng, Mike Pivnenko, Brian Robertson, Rong Zhang, and Daping Chu. A compensation method for the full phase retardance nonuniformity in phase-only liquid crystal on silicon spatial light modulators. *Optics Express*, 22(21):26392–26402, October 2014.
- [137] Tomáš Čižmár, Michael Mazilu, and Kishan Dholakia. In situ wavefront correction and its application to micromanipulation. *Nature Photonics*, 4(6):388–394, June 2010.
- [138] José Luis Martínez, Ignacio Moreno, María del Mar Sánchez-López, Asticio Vargas, and Pascuala García-Martínez. Analysis of multiple internal reflections in a parallel aligned liquid crystal on silicon SLM. *Optics Express*, 22(21):25866–25879, October 2014.
- [139] E. G. van Putten, I. M. Vellekoop, and A. P. Mosk. Spatial amplitude and phase modulation using commercial twisted nematic LCDs. *Applied Optics*, 47(12):2076–2081, April 2008.
- [140] Omel Mendoza-Yero, Gladys Mínguez-Vega, and Jesús Lancis. Encoding complex fields by using a phase-only optical element. *Optics Letters*, 39(7):1740–1743, April 2014.
- [141] Cheng-Shan Guo, Zhen-Yu Rong, and Shu-Zhen Wang. Double-channel vector spatial light modulator for generation of arbitrary complex vector beams. *Optics Letters*, 39(2):386–389, January 2014.
- [142] Erik H. Waller and Georg von Freymann. Independent spatial intensity, phase and polarization distributions. *Optics Express*, 21(23):28167–28174, November 2013.
- [143] D. Bowman, T. L. Harte, V. Chardonnet, C. De Groot, S. J. Denny, G. Le Goc, M. Anderson, P. Ireland, D. Cassettari, and G. D. Bruce. High-fidelity phase and amplitude control of phase-only computer generated holograms using conjugate gradient minimisation. *Optics Express*, 25(10):11692–11700, May 2017.
- [144] Long Zhu and Jian Wang. Arbitrary manipulation of spatial amplitude and phase using phase-only spatial light modulators. *Scientific Reports*, 4, December 2014.
- [145] Atsushi Shibukawa, Atsushi Okamoto, Yuta Goto, Satoshi Honma, and Akihisa Tomita. Digital phase conjugate mirror by parallel arrangement of two phase-only spatial light modulators. *Optics Express*, 22(10):11918–11929, May 2014.
- [146] Zhen-Yu Rong, Yu-Jing Han, Shu-Zhen Wang, and Cheng-Shan Guo. Generation of arbitrary vector beams with cascaded liquid crystal spatial light modulators. *Optics Express*, 22(2):1636–1644, January 2014.
- [147] J. R. Fienup. Phase retrieval algorithms: a comparison. *Applied Optics*, 21(15):2758–2769, August 1982.
- [148] Emilio Sánchez-Ortiga, Ana Doblas, Genaro Saavedra, Manuel Martínez-Corral, and Jorge Garcia-Sucerquia. Off-axis digital holographic microscopy: practical design parameters for operating at diffraction limit. *Applied Optics*, 53(10):2058–2066, April 2014.

-
- [149] R. Carminati, J. J. Sáenz, J.-J. Greffet, and M. Nieto-Vesperinas. Reciprocity, unitarity, and time-reversal symmetry of the S matrix of fields containing evanescent components. *Physical Review A*, 62(1):012712, June 2000.
- [150] Stefan Rotter and Sylvain Gigan. Light fields in complex media: Mesoscopic scattering meets wave control. *Reviews of Modern Physics*, 89(1):015005, March 2017.
- [151] Donald B. Conkey, Antonio M. Caravaca-Aguirre, and Rafael Piestun. High-speed scattering medium characterization with application to focusing light through turbid media. *Optics Express*, 20(2):1733–1740, January 2012.
- [152] Mooseok Jang, Haowen Ruan, Ivo M. Vellekoop, Benjamin Judkewitz, Euiheon Chung, and Changhuei Yang. Relation between speckle decorrelation and optical phase conjugation (OPC)-based turbidity suppression through dynamic scattering media: a study on in vivo mouse skin. *Biomedical Optics Express*, 6(1):72–85, January 2015.
- [153] Yan Liu, Cheng Ma, Yuecheng Shen, Junhui Shi, and Lihong V. Wang. Focusing light inside dynamic scattering media with millisecond digital optical phase conjugation. *Optica*, 4(2):280–288, February 2017.
- [154] Agnese Lucesoli and Tullio Rozzi. Image transmission and radiation by truncated linearly polarized multimode fiber. *Applied Optics*, 46(15):3031–3037, May 2007.
- [155] Donald B. Conkey, Eirini Kakkava, Thomas Lanvin, Damien Loterie, Nicolino Stasio, Edgar Morales-Delgado, Christophe Moser, and Demetri Psaltis. High power, ultrashort pulse control through a multi-core fiber for ablation. *Optics Express*, 25(10):11491–11502, May 2017.
- [156] Dirk Jalas, Alexander Petrov, Manfred Eich, Wolfgang Freude, Shanhui Fan, Zongfu Yu, Roel Baets, Miloš Popović, Andrea Melloni, John D. Joannopoulos, Mathias Vanwolleghem, Christopher R. Doerr, and Hagen Renner. What is — and what is not — an optical isolator. *Nature Photonics*, 7(8):579–582, August 2013.
- [157] F. Albe, H. Fagot, and P. Smigielski. Use Of An Endoscope For Optical Fiber Holography. volume 0600, pages 199–203, 1986.
- [158] Peter J. Schreier and Louis L. Scharf. Correlation analysis. In *Statistical Signal Processing of Complex-Valued Data: The Theory of Improper and Noncircular Signals*, pages 85–88. Cambridge University Press, February 2010.
- [159] Robert J. Collier, Christoph B. Burckhardt, and Lawrence H. Lin. *Optical Holography*. Academic Press, New York, 1971.
- [160] Robert Jones and Catherine Wykes. *Holographic and Speckle Interferometry*. Cambridge University Press, January 1989. Google-Books-ID: 6u34K_EIV6EC.
- [161] Vincent Toal. *Introduction to Holography*. CRC Press, September 2011. Google-Books-ID: PRCrRc7jiG0C.

Bibliography

- [162] Philip E. Ciddor. Refractive index of air: new equations for the visible and near infrared. *Applied Optics*, 35(9):1566–1573, March 1996.
- [163] Alan W. Snyder and John D. Love. *Optical Waveguide Theory*. Chapman and Hall Ltd., London, 1983.
- [164] Shay Ohayon, Antonio Miguel Caravaca Aguirre, Rafael Piestun, and Jim J. DiCarlo. Deep brain fluorescence imaging with minimally invasive ultra-thin optical fibers. *bioRxiv*, page 116350, March 2017.
- [165] J. Arlt and M. J. Padgett. Generation of a beam with a dark focus surrounded by regions of higher intensity: the optical bottle beam. *Optics Letters*, 25(4):191–193, February 2000.
- [166] K. T. Gahagan and G. A. Swartzlander. Optical vortex trapping of particles. *Optics Letters*, 21(11):827–829, June 1996.
- [167] A. Turpin, V. Shvedov, C. Hnatovsky, Yu V. Loiko, J. Mompart, and W. Krolikowski. Optical vault: A reconfigurable bottle beam based on conical refraction of light. *Optics Express*, 21(22):26335–26340, November 2013.
- [168] Stefan W. Hell and Jan Wichmann. Breaking the diffraction resolution limit by stimulated emission: stimulated-emission-depletion fluorescence microscopy. *Optics Letters*, 19(11):780–782, June 1994.
- [169] Ivo M. Vellekoop, Meng Cui, and Changhuei Yang. Digital optical phase conjugation of fluorescence in turbid tissue. *Applied Physics Letters*, 101(8):081108, 2012.
- [170] Percival F. Almero, Laura Waller, Mostafa Agour, Claas Falldorf, Giancarlo Pedrini, Wolfgang Osten, and Steen G. Hanson. Enhanced deterministic phase retrieval using a partially developed speckle field. *Optics Letters*, 37(11):2088–2090, June 2012.
- [171] Mooseok Jang, Haowen Ruan, Haojiang Zhou, Benjamin Judkewitz, and Changhuei Yang. Method for auto-alignment of digital optical phase conjugation systems based on digital propagation. *Optics Express*, 22(12):14054–14071, June 2014.
- [172] C. J. R. Sheppard and A. Choudhury. Image Formation in the Scanning Microscope. *Optica Acta: International Journal of Optics*, 24(10):1051–1073, October 1977.
- [173] James Pawley. *Handbook of Biological Confocal Microscopy*. Springer Science & Business Media, December 2012.
- [174] Joey M. Jabbour, Meagan A. Saldua, Joel N. Bixler, and Kristen C. Maitland. Confocal Endomicroscopy: Instrumentation and Medical Applications. *Annals of Biomedical Engineering*, 40(2):378–397, October 2011.
- [175] Arthur F. Gmitro and David Aziz. Confocal microscopy through a fiber-optic imaging bundle. *Optics Letters*, 18(8):565–567, April 1993.

-
- [176] J Knittel, L Schnieder, G Buess, B Messerschmidt, and T Possner. Endoscope-compatible confocal microscope using a gradient index-lens system. *Optics Communications*, 188(5–6):267–273, February 2001.
- [177] Jonathan TC Liu, Michael J. Mandella, Hyejun Ra, Larry K. Wong, Olav Solgaard, Gordon S. Kino, Wibool Piyawattanametha, Christopher H. Contag, and Thomas D. Wang. Miniature near-infrared dual-axes confocal microscope utilizing a two-dimensional microelectromechanical systems scanner. *Optics letters*, 32(3):256–258, 2007.
- [178] Hyun-Joon Shin, Mark C. Pierce, Daesung Lee, Hyejun Ra, Olav Solgaard, and Rebecca Richards-Kortum. Fiber-optic confocal microscope using a MEMS scanner and miniature objective lens. *Optics express*, 15(15):9113–9122, 2007.
- [179] Christoph J. Engelbrecht, Richard S. Johnston, Eric J. Seibel, and Fritjof Helmchen. Ultra-compact fiber-optic two-photon microscope for functional fluorescence imaging in vivo. *Optics express*, 16(8):5556–5564, 2008.
- [180] Benno H. W. Hendriks, Walter C. J. Bierhoff, Jeroen J. L. Horikx, Adrien E. Desjardins, Cees A. Hezemans, Gert W. 't Hooft, Gerald W. Lucassen, and Nenad Mihajlovic. High-resolution resonant and nonresonant fiber-scanning confocal microscope. *Journal of Biomedical Optics*, 16(2):026007–026007–8, 2011.
- [181] Optiscan Pty. Ltd. OptiScan FIVE 1 Product Brochure, April 2006.
- [182] Alexandre S. Goy and Demetri Psaltis. Digital confocal microscope. *Optics Express*, 20(20):22720–22727, September 2012.
- [183] Yuta Goto, Atsushi Okamoto, Masataka Toda, Yasuyuki Kuno, Jin Nozawa, Kazuhisa Ogawa, and Akihisa Tomita. Digital confocal microscopy using a virtual 4f-system based on numerical beam propagation for depth measurement without mechanical scanning. *Japanese Journal of Applied Physics*, 55(8S3):08RE04, July 2016.
- [184] Alexandre S. Goy, Michaël Unser, and Demetri Psaltis. Multiple contrast metrics from the measurements of a digital confocal microscope. *Biomedical Optics Express*, 4(7):1091–1103, July 2013.
- [185] Amnon Yariv. Fundamental media considerations for the propagation of phase-conjugate waves. *Optics Letters*, 16(18):1376–1378, September 1991.
- [186] George Barbastathis, Michal Balberg, and David J. Brady. Confocal microscopy with a volume holographic filter. *Optics Letters*, 24(12):811–813, June 1999.
- [187] Antonio Miguel Caravaca Aguirre and Rafael Piestun. Robustness of multimode fiber focusing through wavefront shaping. In *Latin America Optics and Photonics Conference*, OSA Technical Digest (online), page LTh4A.23. Optical Society of America, November 2014.

Bibliography

- [188] Damien Loterie, Demetri Psaltis, and Christophe Moser. Confocal microscopy via multimode fibers: fluorescence bandwidth. volume 9717, pages 97171C–1 to –6, 2016.
- [189] A. Vander Lugt. Signal detection by complex spatial filtering. *IEEE Transactions on Information Theory*, 10(2):139–145, April 1964.
- [190] Joseph L. Horner and Peter D. Gianino. Phase-only matched filtering. *Applied Optics*, 23(6):812, March 1984.
- [191] Sebastianus A. Goorden, Marcel Horstmann, Allard P. Mosk, Boris ?kori?, and Pepijn W. H. Pinkse. Quantum-secure authentication of a physical unclonable key. *Optica*, 1(6):421–424, December 2014.
- [192] Salvador González and Zeina Tannous. Real-time, in vivo confocal reflectance microscopy of basal cell carcinoma. *Journal of the American Academy of Dermatology*, 47(6):869–874, December 2002.
- [193] Chen Liang, Michael Descour, Kung-Bin Sung, and Rebecca Richards-Kortum. Fiber confocal reflectance microscope (FCRM) for in-vivo imaging. *Optics Express*, 9(13):821–830, 2001.
- [194] Daria Andreoli, Giorgio Volpe, Sébastien Popoff, Ori Katz, Samuel Grésillon, and Sylvain Gigan. Deterministic control of broadband light through a multiply scattering medium via the multispectral transmission matrix. *Scientific Reports*, 5, May 2015.
- [195] Mickael Mounaix, Hugo Defienne, and Sylvain Gigan. Deterministic light focusing in space and time through multiple scattering media with a Time-Resolved Transmission Matrix approach. *arXiv:1607.06331 [physics]*, July 2016. arXiv: 1607.06331.
- [196] Mickael Mounaix, Daria Andreoli, Hugo Defienne, Giorgio Volpe, Ori Katz, Samuel Grésillon, and Sylvain Gigan. Spatiotemporal Coherent Control of Light through a Multiple Scattering Medium with the Multispectral Transmission Matrix. *Physical Review Letters*, 116(25):253901, June 2016.
- [197] Edgar E. Morales Delgado, Ioannis N. Papadopoulos, Salma Farahi, Demetri Psaltis, and Christophe Moser. Delivery of an ultrashort spatially focused pulse to the other end of a multimode fiber using digital phase conjugation. volume 9335, pages 93350J–93350J–7, 2015.
- [198] Damien Loterie, Demetri Psaltis, and Christophe Moser. Bend translation in multimode fiber imaging. *Optics Express*, 25(6):6263–6273, March 2017.
- [199] D. Z. Anderson, M. A. Bolshtyansky, and B. Ya. Zel’dovich. Stabilization of the speckle pattern of a multimode fiber undergoing bending. *Optics Letters*, 21(11):785–787, June 1996.

- [200] Maxim A. Bolshtyansky and B. Ya. Zel'dovich. Stabilization of transmission function: theory for an ultrathin endoscope of one multimode fiber. *Applied Optics*, 36(16):3673–3681, June 1997.
- [201] D. Gloge. Weakly guiding fibers. *Applied Optics*, 10(10):2252–2258, 1971.
- [202] Elias Snitzer. Cylindrical dielectric waveguide modes. *JOSA*, 51(5):491–498, 1961.
- [203] Awad H. Al-Mohy and Nicholas J. Higham. Computing the action of the matrix exponential, with an application to exponential integrators. *SIAM Journal on Scientific Computing*, 33(2):488–511, January 2011.
- [204] Allan W. Snyder and William R. Young. Modes of optical waveguides. *JOSA*, 68(3):297–309, March 1978.
- [205] Amnon Yariv, Pochi Yeh, and Amnon Yariv. *Photonics: Optical Electronics in Modern Communications*. Oxford University Press, New York, 2007.
- [206] Clifford R. Pollock and Michal Lipson. *Integrated Photonics*. Kluwer Academic Publishers, Boston, USA, 2003.
- [207] Katsunari Okamoto. *Fundamentals of Optical Waveguides*. Academic Press, 2006.

ACADEMIC CURRICULUM VITAE

DAMIEN LOTERIE

Address EPFL STI IMT LAPD, BM 4109
Station 17
CH-1015 Lausanne
Switzerland
Phone +41 21 69 35184
E-mail damien.loterie@epfl.ch
Date of birth September 21, 1990

Education

- 2013 – 2017 **PhD at the Laboratory of Applied Photonics Devices**
École polytechnique fédérale de Lausanne (EPFL), Switzerland
Research on fiber optic endoscopy.
- 2011 – 2013 **Master in Engineering, Photonics (minor in control systems)**
Vrije Universiteit Brussel (VUB), Belgium
Erasmus exchange (2011-2012) in EPFL, Lausanne, Switzerland,
Research internship (Aug. 2012) in IPHT, Jena, Germany.
- 2008 – 2011 **Bachelor in Engineering, Electronics and Information Technology**
Vrije Universiteit Brussel (VUB), Belgium
Summer course (Aug. 2009) on renewable energy in Uppsala, Sweden.

Projects

- 2013 – 2017 **Fiber optic endoscopy**
PhD thesis. Supervisor: Prof. C. Moser (EPFL, Lausanne).
Developed an ultra-thin fiber optic microscopy system, for biomedical applications. Wrote high-throughput data processing algorithms that doubled the achievable resolution and field of view. Implemented new imaging modalities such as confocal and two-photon fluorescence microscopy.
- 2012 – 2013 **Raman spectroscopy in lab-on-chips**
Master's thesis. Supervisor: Prof. H. Ottevaere (VUB, Brussels).
Engineered a micro-optical structure that allows high-quality Raman signals to be acquired from a low-cost polymer module. The design is suitable for mass production.
Received the IMEC award for best Master's thesis in engineering.
- Spring 2012 **Surface metrology**
Semester project. Supervisor: Prof. C. Moser (EPFL, Lausanne).
Built a surface measurement system from scratch (hardware & software), based on white light interferometry. With it, I measured deformations in a self-tracking solar concentrator system.
- Autumn 2011 **Optical coherence microscopy**
Semester project. Supervisor: Prof. T. Lasser (EPFL, Lausanne).
Quantified the performance of anisotropic nanoparticles as contrast agents in OCM.

Skills

Technical competences	Microscopic imaging, optical fibers, digital holography, spatial light modulators, optical metrology, micro-optics, optical coherence tomography, Raman spectroscopy. System identification and control.
Software	Scientific programs (MATLAB, Octave, Mathematica, LabView, COMSOL) Mechanical design (Solidworks, Inventor) Optical design (ASAP, FRED, MODE Solutions) Graphical design (Photoshop, Illustrator, Inkscape), Office suite.
IT competences	Extensive programming knowledge (C++, MATLAB, Python, C#, Java, ASM), with practical experience in imaging, numerical simulations, signal processing and hardware interfaces. Notions of system administration (Linux).
Languages	French: native language English: very good (C2) Dutch: very good (C2) German: beginner

Publications

Peer-reviewed articles	<p>D. Loterie, D. Psaltis, C. Moser, "Bend translation in multimode fiber imaging," <i>Optics Express</i>, vol. 25, num. 6, p. 6263-6273, 2017.</p> <p>D. Loterie, S. A. Goorden, D. Psaltis, C. Moser, "Confocal microscopy through a multimode fiber using optical correlation," <i>Optics Letters</i>, vol. 40, num. 24, p. 5754-5757, 2015.</p> <p>D. Loterie, S. Farahi, I. Papadopoulos, A. Goy, D. Psaltis, C. Moser, "Digital confocal microscopy through a multimode fiber," <i>Optics Express</i>, vol. 23, num. 18, p. 23845-23858, 2015.</p> <p>D. De Coster, D. Loterie, H. Ottevaere, M. Vervaeke, J. Van Erps, J. Missinne, H. Thienpont, "Free-Form Optics Enhanced Confocal Raman Spectroscopy for Optofluidic Lab-on-Chips," <i>IEEE Journal of Selected Topics in Quantum Electronics</i>, vol. 21, num. 4, p. 79-86, 2015.</p> <p>E. J. Tremblay, D. Loterie, C. Moser, "Thermal phase change actuator for self-tracking solar concentration," <i>Optics Express</i>, vol. 20, num. 23, p. A964-A976, 2012.</p>
Conference papers and talks	<p>D. Loterie, "Microscopic Imaging Using Fibers", 29th Annual Conference of the IEEE Photonics Society (03/10/2016).</p> <p>D. Loterie, D. Psaltis, C. Moser, "Confocal microscopy via multimode fibers: fluorescence bandwidth", in <i>Proc. SPIE 9717, Adaptive Optics and Wavefront Control for Biological Systems II</i>, p. 97171C (15/02/2016).</p> <p>D. Loterie, S. Farahi, I. N. Papadopoulos, A. Goy, D. Psaltis, C. Moser, "Reflection-mode confocal microscopy through a multimode fiber," <i>SPIE/OSJ Biophotonics Japan 2015</i> (27/10/2015).</p> <p>D. Loterie, S. Farahi, D. Psaltis, C. Moser, "Reflection-mode confocal microscopy via a multimode fiber", <i>CLEO Munich 2015</i> (25/06/2015).</p> <p>D. Loterie, S. Farahi, I. Papadopoulos, A. Goy, D. Psaltis, C. Moser, "Reflection-mode confocal microscopy through a multimode fiber", <i>Photorefractive 2015</i> (17/06/2015).</p> <p>D. Loterie, S. Farahi, D. Psaltis, C. Moser, "Complex pattern projection through a multimode fiber", in <i>Proc. SPIE 9335, Adaptive Optics and Wavefront Control for Biological Systems</i>, p. 93350I (7/02/2015).</p>

Lausanne, April 21, 2017.